



Advances in Optics and Photonics

Spatial light interference microscopy: principle and applications to biomedicine

XI CHEN,  **MIKHAIL E. KANDEL,**  **AND GABRIEL POPESCU*** 

Quantitative Light Imaging Laboratory, Department of Electrical and Computer Engineering, Beckman Institute for Advanced Science and Technology, University of Illinois at Urbana-Champaign, Urbana, Illinois 61801, USA

**Corresponding author: gpopescu@illinois.edu*

Received December 16, 2020; revised March 18, 2021; accepted March 28, 2021; published May 5, 2021 (Doc. ID 417837)

In this paper, we review spatial light interference microscopy (SLIM), a common-path, phase-shifting interferometer, built onto a phase-contrast microscope, with white-light illumination. As one of the most sensitive quantitative phase imaging (QPI) methods, SLIM allows for speckle-free phase reconstruction with sub-nanometer path-length stability. We first review image formation in QPI, scattering, and full-field methods. Then, we outline SLIM imaging from theory and instrumentation to diffraction tomography. Zernike’s phase-contrast microscopy, phase retrieval in SLIM, and halo removal algorithms are discussed. Next, we discuss the requirements for operation, with a focus on software developed in-house for SLIM that enables high-throughput acquisition, whole slide scanning, mosaic tile registration, and imaging with a color camera. We introduce two methods for solving the inverse problem using SLIM, white-light tomography, and Wolf phase tomography. Lastly, we review the applications of SLIM in basic science and clinical studies. SLIM can study cell dynamics, cell growth and proliferation, cell migration, mass transport, etc. In clinical settings, SLIM can assist with cancer studies, reproductive technology, blood testing, etc. Finally, we review an emerging trend, where SLIM imaging in conjunction with artificial intelligence brings computational specificity and, in turn, offers new solutions to outstanding challenges in cell biology and pathology. © 2021 Optical Society of America

<https://doi.org/10.1364/AOP.417837>

1. Introduction	355
1.1. Motivation for Label-Free Imaging	355
1.2. Quantitative Phase Imaging	355
1.3. Other Optical Label-Free Imaging Methods	356
2. Principles of QPI	358
2.1. Scattering	358
2.1a. First-Order Born Approximation	358

2.1b.	Physical Significance of Phase in Transmission and Reflection Geometries	359
2.1c.	Scattering of Spatiotemporally Broadband Fields	361
2.2.	Full-Field QPI Methods	362
2.2a.	Spatial Phase Modulation: Off-Axis Interferometry	362
2.2b.	Temporal Phase Modulation: Phase-Shifting Interferometry	363
2.2c.	QPI Figures of Merit	364
2.2d.	Tomographic Methods Based on QPI	365
3.	Principles of SLIM	368
3.1.	Theory	368
3.1a.	Zernike Phase-Contrast Microscope	368
3.1b.	Phase Retrieval in SLIM	369
3.1c.	Halo Removal	371
3.2.	Instrumentation	373
3.2a.	Alignment and Calibration	373
3.2b.	High-Throughput Acquisition	375
3.2c.	Whole Slide Imaging	377
3.2d.	Mosaic Tile Registration	378
3.2e.	SLIM with a Color Camera	379
3.2f.	SLIM and Other QPI Methods	380
3.3.	Diffraction Tomography using SLIM	381
3.3a.	White-Light Diffraction Tomography	381
3.3b.	Wolf Phase Tomography	382
4.	SLIM Applications	386
4.1.	Basic Science Applications	386
4.1a.	Cell Dynamics	386
4.1b.	Cell Growth	386
4.1c.	Cell Migration	390
4.1d.	Intracellular Transport	391
4.1e.	Applications in Neuroscience	393
4.2.	Clinical Applications	394
4.2a.	Cancer Screening	394
4.2b.	Cancer Diagnosis	396
4.2c.	Cancer Prognosis	399
4.2d.	SLIM as Assisted Reproductive Technology	400
4.2e.	Blood Testing	401
5.	Emerging Trends in SLIM Imaging	402
5.1.	Phase Imaging with Computational Specificity	402
5.2.	SLIM and AI in Cell Biology	405
5.3.	SLIM and AI in Pathology	407
6.	Summary and Outlook	410
	Funding	412
	Disclosures	412
	References	412

Spatial light interference microscopy: principle and applications to biomedicine

XI CHEN, MIKHAIL E. KANDEL, AND GABRIEL POPESCU

1. INTRODUCTION

1.1. Motivation for Label-Free Imaging

Most biological samples are optically thin and transparent under visible light. They have low contrast under conventional bright-field microscopes. Fluorescent labels are routinely used in combination with optical microscopes to investigate details inside of tissues and cells with high specificity. Although fluorescence microscopy has been used broadly in biomedicine [1], the approach still suffers from important limitations. Phototoxicity and photobleaching modify cellular and fluorophore structures due to the high-intensity illumination, leading to difficulties in live-cell imaging for a long period [2,3]. Moreover, fluorescent dyes can interfere with cell functions [4]. When multiple fluorescent dyes or proteins are used, the spectra can overlap, making it difficult to distinguish between different structures [5]. Besides, the cost of reagents can add up. Importantly, the fluorescence signal can vary across the specimen when staining is inhomogeneous, resulting in difficulty interpreting the images quantitatively [6]. Finally, whenever using genetic engineering, the transfection process can be complex and time-consuming [7].

Complementary to fluorescence microscopy, label-free imaging is non-destructive and, of course, lacks photobleaching [8]. Imaging unlabeled specimens requires minimal or no sample preparation and provides detailed dynamic and morphological information in live cells [9]. The cells are in their intact, native states, leading to more biologically relevant studies. Label-free imaging is suitable for long-period live-cell imaging without photobleaching. Multiple cellular characteristics can be measured repeatedly over time in longitudinal studies [10–12]. These capabilities open new opportunities to study long-term cellular events such as proliferation and response to chemical stimulations.

1.2. Quantitative Phase Imaging

Quantitative phase imaging (QPI) is an emerging field built on the foundation of microscopy, holography, and scattering techniques [13–16]. The understanding of the microscopic image as a complicated interferogram established by Abbe has been essential for the development of microscopic techniques, such as phase-contrast microscopy and differential interference contrast (DIC) microscopy [17–19]. These techniques greatly enhance the intrinsic contrast without labels and enable insight into the transparent structures. The invention of digital holography opened the door to storing the phase information of optical fields. Unlike the original implementation of holography, which was developed to record the intensity distribution in such a way as to preserve the phase information, QPI is aimed at quantitatively rendering the pure phase distribution, eliminating the intensity dependence [20]. One feature of QPI is the nanoscale sensitivity, enabling important studies of cellular morphology, cell membrane fluctuations, drug response, etc. [21–24] The phase information associated with the sample depends on critical parameters, such as the refractive index (RI) and dry mass of the specimen [25,26].

The QPI modalities can be divided into interferometric and non-interferometric, depending on whether an interferometer is involved in the phase measurement [27–29]. The precursors of interferometric phase measurements were performed via single-point, scanning techniques, such as optical coherence tomography (OCT) [30,31]. Later on, full-field QPI methods were developed based on spatial phase modulation and temporal phase modulation, i.e., off-axis and phase-shifting interferometers, respectively (chapter 2) [32–34]. Non-interferometric phase measurements include wavefront sensing, such as the Shack–Hartmann wavefront sensor, which is broadly employed in the adaptive optics field [35,36]. Other non-interferometric methods include phase retrieval techniques using iterative methods or deterministic methods [37–39]. The well-known iterative methods are Gerchberg–Saxton (GS) algorithm and ptychography [40,41]. A special case of QPI using deterministic methods of phase retrieval is based on the transport of the intensity equation. In this case, the phase information can be retrieved from the axial gradient of the intensity [42]. Note that, although “non-interferometric” methods lack an interferometer, they still use interference of light as the fundamental process for recording the phase information. For example, the local gradient of the wavefront is captured via the Shack–Hartmann sensor by recording the superposition (interference) of the waves emerging at each aperture. The computational phase retrieval methods exploit the fact that an image is an interferogram. Similarly, the techniques based on the transport of intensity equation treat the image field as the interference between the incident and scattered field, at several positions around the plane of focus. Interestingly, we can describe the field at each point in the image as the interference between the scattered field and the incident field, which acts as a common reference for a highly parallel interferometry system. This description is fundamental for understanding Zernike’s phase-contrast microscopy (Subsection 3.1a) and spatial light interference microscopy (SLIM) (Subsection 3.1b), which is a generalization of this method.

SLIM can be easily adopted in the field, due to its intrinsic stability and lack of speckles, along with its implementation as an add-on module to existing microscopes [8,43–58]. This review is likely to help further disseminate this technology for biomedical use.

1.3. Other Optical Label-Free Imaging Methods

Aside from the QPI methods, many more label-free imaging methods have been developed over the last century, based on different contrast mechanisms. This subsection serves as a brief summary of other optical label-free imaging methods and their comparison to SLIM. We compared the lateral and axial resolution, penetration depth, contrast mechanism, and imaging modality modes. The numbers shown in Table 1 are estimated values considering the different subfields that lie within the main methods.

Multiphoton microscopy is a nonlinear method widely employed in the biomedicine field, especially for imaging bulk tissues [59]. It includes several label-free methods such as second-harmonic generation microscopy (SHGM) [60], third-harmonic generation microscopy (THGM) [61], and coherent Raman scattering microscopy (CRSM) [62]. The contrast in the SHGM and THGM comes from the variations in a sample’s ability to generate harmonics, i.e., $\chi^{(2)}$ and $\chi^{(3)}$ properties. The contrast in CRSM depends on the Raman-active vibrational modes of molecules in the sample. Stimulated Raman scattering (SRS) and coherent anti-Stokes Raman scattering (CARS) are two major techniques in CRSM [63]. Compared to CRSM and SRS, confocal Raman microscopy (CRM) normally measures a spontaneous Raman spectrum with continuous-wave lasers. Multiphoton microscopy has a large number of applications in cancer studies, cell metabolism, and pharmaceutical research [64–67].

Fluorescence-lifetime imaging microscopy (FLIM) measures the lifetime associated with the fluorophore from a sample, and, in the autofluorescence case, is also a label-free method [68]. The fluorescence lifetime depends on the micro-environment of the fluorophore; thus, it is very sensitive to pH, chemical species, and viscosity [69–71]. Two-photon microscopy can measure autofluorescence with living tissues up to about 1 mm in thickness [72]. Fourier transform IR (FTIR) spectroscopy is another label-free method that allows for spectroscopic imaging via interferometric imaging [73]. It has found a variety of biological and clinical applications [74,75].

Photoacoustic tomography (PAT) combines sound waves and electromagnetic waves to create multiscale, multicontrast images of biological samples [76]. The penetration depth can go beyond the optical transport mean-free path due to the photoacoustic effect, thus enabling imaging from subcellular organelles to organ scales [77]. Diffuse optical imaging (DOI) is a label-free method using near-infrared spectroscopy for diffusive samples [78]. Optical projection tomography (OPT) [79] is the optical equivalent of x-ray computed tomography suitable for three-dimensional (3D) imaging of specimens ranging from 1 to 10 mm across. Photothermal optical microscopy [80] uses heating and probing laser beams to detect the refractive-index change in the specimens.

Imaging techniques such as confocal microscopy, light-sheet microscopy, 4pi microscopy, and I⁵M aim at improving the optical sectioning, and larger frequency support can also be used in label-free methods, using either scattered fields or intrinsic fluorophores [81–84]. The near-field scanning optical microscope (SNOM) [85] breaks the far-field resolution limit by exploiting the properties of evanescent waves. Serial time-encoded amplified microscopy (STEAM) [86] is an ultrafast continuous real-time imaging technique with megahertz frame rate by employing the photonic time stretch with internal Raman amplification.

Table 1. Comparison of Various Optical Label-Free Imaging Methods (W, widefield; S, scanning; T, transmission; R, reflection)

Label-Free Imaging Modality	Contrast Mechanism	Widefield/ Scanning	Transmission/ Reflection	Lateral Resolution (μm)	Axial Resolution (μm)	Penetration Depth (μm)
Bright-field	Absorption	W/S	T/R	~ 0.3	~ 2	~ 100
Dark-field	Absorption/ refraction	W	T/R	~ 0.3	~ 2	~ 25
Phase-contrast	Refraction	W	T	~ 0.3	~ 2	~ 150
DIC	Refraction	W/S	T/R	~ 0.3	~ 2	~ 300
SLIM	Refraction	W	T	~ 0.3	~ 2	~ 150
OCT	Scattering	W/S	T/R	~ 0.3	~ 8	~ 3000
STEAM	Scattering	S	T/R	~ 0.7	N/A	~ 100
SHGM	$\chi^{(2)}$ properties	S	T/R	~ 0.3	~ 2	$\sim 1,000$
THGM	$\chi^{(3)}$ properties	S	T/R	~ 0.3	~ 2	$\sim 1,000$
CRSM	Vibrational modes	S	T/R	~ 0.2	~ 1	~ 100
SRS	Vibrational modes	S	T/R	~ 0.2	~ 1	~ 100
CARS	Vibrational modes	S	T/R	~ 2	~ 1	~ 100
CRM	Vibrational modes	S	R	~ 0.25	~ 1	~ 100
FLIM	Autofluorescence lifetime	W/S	R	~ 0.25	~ 0.25	~ 200
Light-sheet	Autofluorescence	W	T/R	~ 0.25	~ 0.5	~ 300
4pi & I ⁵ M	Autofluorescence	W/S	T/R	~ 0.1	~ 0.1	~ 50
Two-photon	Autofluorescence	W/S	R	~ 0.3	~ 2	~ 1000
FTIR	Infrared spectrum	S	R	~ 5	N/A	~ 1
PAT	Photoacoustic effect	W	R	~ 0.5 to ~ 100	~ 50	$\sim 50,000$
DOI	Absorption	W	R	~ 1000	N/A	$\sim 50,000$
OPT	Transmission or emission	W	T/R	~ 10	~ 10	~ 5000
Photothermal	Nonlinear refraction	W	T/R	~ 5	~ 5	~ 50
Near-field	Scattering/ autofluorescence	S	T/R	~ 0.02	~ 0.003	~ 0.7

2. PRINCIPLES OF QPI

2.1. Scattering

2.1a. First-Order Born Approximation

The intrinsic contrast generated in QPI is due to light scattering. Scattering is the general term that describes the interaction between a field and the real part of the dielectric permittivity [63]. While the processes involved in QPI are linear, the term scattering includes nonlinear phenomena, such as second-harmonic generation (SHG). In this section, we will restrict ourselves to situations where the response of the object to the incident field is linear and static [87,88]. In general, solving the wave equations for an arbitrary inhomogeneous object is difficult, with no analytic solutions. However, here we show that, with weak scattering approximation, or the first-order Born approximation, analytic solutions can be obtained. The weak scattering regime occurs wherever the object's RI is very close to the background's RI. In this case, we can derive an expression of the far-zone scattered field using the first-order Born approximation [89].

The light propagation in the medium is governed by the Helmholtz equation

$$\nabla^2 U(\mathbf{r}, \omega) + \beta_0^2 U(\mathbf{r}, \omega) = -4\pi F(\mathbf{r}, \omega) U(\mathbf{r}, \omega), \quad (1)$$

where $\beta_0 = \omega/c$ is the wavenumber in vacuum. $F(\mathbf{r}, \omega)$ is the scattering potential defined as

$$F(\mathbf{r}, \omega) = \frac{1}{4\pi} \beta_0^2 [n^2(\mathbf{r}, \omega) - 1], \quad (2)$$

where n is the refractive index. Note that, in Eq. (1), the total field U is both present on the equation, indicating that any scattered field can be scattered again, generating multiple scattering, and acting as a secondary source. The first-order Born approximation assumes that the field inside of the object is only slightly different from the incident field. This weak scattering approximation dramatically simplifies the work, as it allows us to replace U with U_i on the right-hand side of Eq. (1). The total field under the first-order Born approximation can be calculated as [89]

$$\begin{aligned} U(\mathbf{r}, \omega) &= U_i(\mathbf{r}, \omega) + U_s(\mathbf{r}, \omega) \\ &\approx U_i(\mathbf{r}, \omega) + \int_V F(\mathbf{r}', \omega) U_i(\mathbf{r}', \omega) \frac{e^{i\beta_0 |\mathbf{r}-\mathbf{r}'|}}{|\mathbf{r}-\mathbf{r}'|} d^3 r'. \end{aligned} \quad (3)$$

If we assume the incident field as a plane wave, i.e., $U_i(\mathbf{r}, \omega) = e^{i\beta_i \cdot \mathbf{r}}$, and the measurement performs in the far-zone, the scattered field can be further simplified using Fraunhofer approximation, i.e., $|\mathbf{r}-\mathbf{r}'| \simeq r - \mathbf{r} \cdot \mathbf{r}'/r$, as [89]

$$\begin{aligned} U_s(\mathbf{r}, \omega) &= \frac{e^{i\beta_0 r}}{r} f(\mathbf{q}, \omega) \\ &= \frac{e^{i\beta_0 r}}{r} \int_V F(\mathbf{r}', \omega) e^{-i\mathbf{q} \cdot \mathbf{r}'} d^3 r', \end{aligned} \quad (4)$$

where $\mathbf{q} = \beta_s - \beta_i$ is the momentum transfer, and β_i and β_s are incident and scattered wave vectors. $f(\mathbf{q}, \omega)$ is the scattering amplitude. We can see that the scattering amplitude along a certain scattering direction depends entirely on one and only one Fourier component of the scattering potential, and the scattered field behaves as modulated spherical waves. The scattering potential can be recovered by the inverse Fourier transform of $f(\mathbf{q}, \omega)$, i.e.,

$$F(\mathbf{r}, \omega) = \int_{V_q} f(\mathbf{q}, \omega) e^{i\mathbf{q}\cdot\mathbf{r}} d^3q. \quad (5)$$

However, the q -domain integration is limited by the Ewald scattering sphere, defined as $\Pi[q/(4k_0)] = \begin{cases} 1, & \sqrt{q_x^2 + q_y^2 + q_z^2} \leq 2k_0 \\ 0, & \text{else} \end{cases}$, whereby the highest possible $q = 2k_0$ is obtained for backscattering. Thus, the reconstructed object from far-zone scattered-field measurement is a low-frequency bandpass version of the true object. Moreover, covering the entire Ewald sphere depends on illuminating the object from all directions and measuring the complex scattered field over the entire solid angle for each illumination direction. This implies that the ideal reconstruction modality requires 4π illumination and detection [90].

2.1b. Physical Significance of Phase in Transmission and Reflection Geometries

The phase information obtained by QPI is different in various imaging modalities. In this subsection, we discuss the interpretation of the phase in transmission and reflection geometries [91]. Let us assume the simplest case where the incident field is a monochromatic plane wave propagating along z , $U_i(\omega) = A(\omega) e^{in_0\beta_0 z}$, where $A(\omega)$ is the spectral amplitude and n_0 is the RI of the background (Fig. 1). The wave equation under the first-order Born approximation is

$$\nabla^2 U_s(\mathbf{r}, \omega) + n_0^2 \beta_0^2 U_s(\mathbf{r}, \omega) = -\beta_0^2 \chi(\mathbf{r}, \omega) U_i(\mathbf{r}, \omega), \quad (6)$$

where $\chi(\mathbf{r}, \omega) = n^2(\mathbf{r}, \omega) - n_0^2$ and n is the RI of the object. Taking the 3D Fourier transform of Eq. (6), we obtain

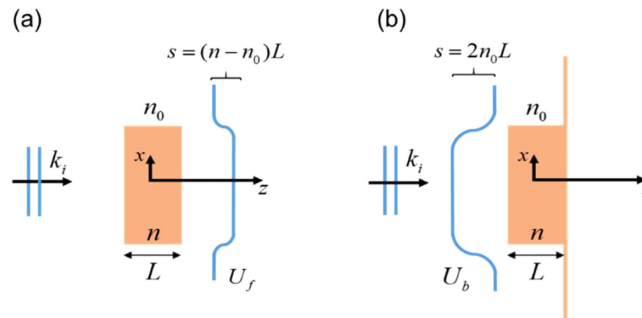
$$(\beta^2 - k^2) U_s(\mathbf{k}, \omega) = -\beta_0^2 A(\omega) \chi(k_\perp, k_z - \beta, \omega), \quad (7)$$

where $\beta = n_0\beta_0$ and $U_s(\mathbf{k}, \omega)$ is the Fourier transform of $U_s(\mathbf{r}, \omega)$ with respect to r ; k_\perp is the transverse spatial frequency. The scattered field in the wavevector space is thus in the form of

$$U_s(\mathbf{k}, \omega) = -\beta_0^2 A(\omega) \chi(k_\perp, k_z - \beta, \omega) \frac{1}{2\gamma} \left[\frac{1}{\gamma - k_z} + \frac{1}{\gamma + k_z} \right], \quad (8)$$

where $\gamma = \sqrt{\beta^2 - k_\perp^2}$. Let us next take the inverse Fourier transform with respect to k_z ; we have

Figure 1



Wavefront changes due to a medium of thickness L and refractive index n for (a) transmission and (b) reflection measurement. Reprinted with permission from [91]. Copyright 2017 Optical Society of America.

$$\begin{aligned}
U_s(k_\perp, z, \omega) &= -i\beta_0^2 A(\omega) \frac{e^{i\gamma z}}{2\gamma} \chi(k_\perp, \gamma - \beta, \omega) \Big|_{z \geq 0} \\
&\quad + i\beta_0^2 A(\omega) \frac{e^{i\gamma z}}{2\gamma} \chi(k_\perp, -\gamma - \beta, \omega) \Big|_{z < 0} \\
&= U^+(k_\perp, z, \omega) + U^-(k_\perp, z, \omega).
\end{aligned} \tag{9}$$

Here U^+ and U^- denote the forward and backscattering fields. Thus, the forward and back total fields can be calculated under the first-order Born approximation

$$U_f(k_\perp, z, \omega) = A(\omega) \delta(k_\perp) e^{i\beta z} - i\beta_0^2 A(\omega) \frac{e^{i\gamma z}}{2\gamma} \chi(k_\perp, \gamma - \beta, \omega), \tag{10}$$

$$\begin{aligned}
U_b(k_\perp, z, \omega) &= A(\omega) \delta(k_\perp) e^{-i\beta z} + i\beta_0^2 A(\omega) \frac{e^{-i\gamma z}}{2\gamma} \chi(k_\perp, -\gamma - \beta, \omega) \\
&\quad - A(\omega) \delta(k_\perp) e^{-i\beta z}
\end{aligned} \tag{11}$$

where $\delta(k_\perp)$ is Kronecker delta. To get an intuitive expression for the phase of the total field and connect this quantity to QPI measurements, we limit k_\perp to a small region close to 0, i.e., make a small-angle approximation. Thus, $\gamma = \sqrt{\beta^2 - k_\perp^2} \approx \beta$. As a result, the forward and backscattered fields (Fig. 1) can be approximated as

$$U_f(\mathbf{r}_\perp, z, \omega) = A(\omega) e^{i\beta z} e^{-i\beta_0[\bar{n}(\mathbf{r}_\perp, \omega) - n_0]L}, \tag{12}$$

$$U_b(\mathbf{r}_\perp, z, \omega) = A(\omega) e^{-i\beta z} e^{+i\beta_0 \int_{-L/2}^{L/2} [n(\mathbf{r}_\perp, z, \omega) - n_0] e^{i2\beta z} dz} - A(\omega) e^{-i\beta z}. \tag{13}$$

We can see that in the forward direction, the approximated phase of the total field is the well-known geometrical phase delay $\varphi(x, y) = \beta_0[\bar{n}(x, y) - n_0]L$. However, the phase of the backscattered field is more complicated, containing two terms. The first term shows the axial projection of the RI contrast weighted by the plane wave $e^{i2\beta z}$. Ignoring transverse features in the object, this expression indicates that the field detected in backscattering consists of a superposition of back-propagating plane waves originating at various depths, z , with respective phases $2\beta z$. The second term is the back-propagating incident field without interacting with the object. This axial integral can be expressed in terms of a z -axis Fourier transform as

$$\begin{aligned}
\phi^-(\mathbf{r}_\perp, z) &= \beta_0 \int_{-\infty}^{\infty} [n(\mathbf{r}_\perp, z, \omega) - n_0] \Pi\left(\frac{2z}{L}\right) e^{i2\beta z} dz \\
&= \beta_0 L \Delta n(\mathbf{r}_\perp, k_z, \omega) \textcircled{\vee} \text{sinc}\left(\frac{Lk_z}{2}\right) \Big|_{k_z = -2\beta},
\end{aligned} \tag{14}$$

where $\Pi(\frac{2z}{L})$ is the rectangular function of width L , and $\textcircled{\vee}$ is the convolution operator in the k_z domain. The phase of the scattered field depends on the convolution of RI at the axial frequency -2β with a sinc function. The oscillatory behavior leads to speckles in the backscattered quantitative phase images, which relates to the object structure in an intricate manner. In summary, we can approximate the phase in the forward and backward fields as

$$\varphi_f(x, y) = \beta_0 \Delta n L, \tag{15}$$

$$\varphi_b(x, y) = \arg(e^{i\phi^-} - 1). \quad (16)$$

The discussion above is only an approximation of the phase for coherent plane waves but gives us a general interpretation of the phase of the fields in a reflective imaging modality. The contributions to the phase of the total fields include double transmitted light, backscattered light, and multi-scattered back-propagating light. Using oblique partially coherent illumination or adding a reflective surface on the bottom of the object in epi QPI can minimize the contribution of the backscattered light and, therefore, enhance the contribution of the double transmitted light [92,93]. However, in this case, the benefit of capturing high frequencies from the object is lost. In sum, extracting quantitative phase information in a backscattering geometry remains challenging. On the one hand, reflection QPI requires developing techniques for separating the multiple scattering contributions to the phase of the detected field. On the other hand, it requires a theoretical interpretation that includes the coherence properties of the fields [94]. The use of broadband partially coherent illumination in a reflective imaging modality, such as epi-illumination gradient light interference microscopy (epi-GLIM) [95], can reduce the speckles in phase images, as it provides strong coherence sectioning, of the order of 1 μm . More generally, white-light interferometry provides optical gating, which minimizes multiple scattering contributions. The scattering of broadband light is discussed next.

2.1c. Scattering of Spatiotemporally Broadband Fields

The coherence properties of light play an important role when working with a spatiotemporally broadband source [94,96–98]. The assumption of the deterministic plane wave is no longer valid. The randomness in the primary sources and propagation media determines the statistical properties of the detected quantities [99–102]. Two important correlation functions to characterize the coherence properties of the fields are the cross-spectral density and mutual coherence function defined, respectively, as [94]

$$W(\mathbf{r}_1, \mathbf{r}_2, \omega) = \langle U^*(\mathbf{r}_1, \omega) U(\mathbf{r}_2, \omega) \rangle, \quad (17)$$

$$\Gamma(\mathbf{r}_1, \mathbf{r}_2, \tau) = \langle U^*(\mathbf{r}_1, \tau) U(\mathbf{r}_2, r + \tau) \rangle_t, \quad (18)$$

where the ensemble average is taken over all the different realizations of the fields; the star denotes the conjugate part. According to the generalized Wiener–Khinchine theorem, two functions are Fourier transform pairs:

$$\Gamma(\mathbf{r}_1, \mathbf{r}_2, \tau) = \int_0^\infty W(\mathbf{r}_1, \mathbf{r}_2, \omega) e^{-2\pi i \omega \tau} d\omega, \quad (19)$$

$$W(\mathbf{r}_1, \mathbf{r}_2, \omega) = \int_{-\infty}^\infty \Gamma(\mathbf{r}_1, \mathbf{r}_2, \tau) e^{2\pi i \omega \tau} d\tau. \quad (20)$$

For isotropic, statistically homogeneous sources, the correlation function will only depend on the difference of the two vectors \mathbf{r}_1 and \mathbf{r}_2 . The cross-spectral density of the incident field is

$$W_{ii}(\mathbf{r}_1 - \mathbf{r}_2, \omega) = \langle U_i^*(\mathbf{r}_1, \omega) U_i(\mathbf{r}_2, \omega) \rangle. \quad (21)$$

Under the first-order Born approximation, the correlation of the scattered fields in the far-zone becomes

$$\begin{aligned} \langle U_s^*(r\hat{\mathbf{k}}_s, \omega) U_s(r\hat{\mathbf{k}}_s, \omega) \rangle &= \frac{k^4}{r^2} V \int_V \left(n^2(r\hat{\mathbf{k}}_s, \omega) - 1 \right) \\ &\times \left(n^2(r\hat{\mathbf{k}}_s + \mathbf{R}, \omega) - 1 \right) W_{ii}(\mathbf{R}, \omega) e^{-i\mathbf{k}_s \cdot \mathbf{R}} d^3 R, \end{aligned} \quad (22)$$

where $\mathbf{R} = \mathbf{r}_2 - \mathbf{r}_1$, $\hat{\mathbf{k}}_s$ is the unit scattered wave vector, and V is the volume of the scatterer. The correlation between the incident and scattered fields is

$$\langle U_i^*(\mathbf{r}, \omega) U_s(\mathbf{r}, \omega) \rangle = \int_V F(\mathbf{r}', \omega) W_{ii}(\mathbf{r}', \omega) \frac{e^{ik_0|\mathbf{r}-\mathbf{r}'|}}{|\mathbf{r}-\mathbf{r}'|} d^3 r'. \quad (23)$$

The propagation of the random fields is governed by the correlation propagation equations, known as the Wolf equations [89],

$$\nabla_1^2 \Gamma(\mathbf{r}_1, \mathbf{r}_2, \tau) = \frac{1}{c^2} \frac{\partial}{\partial \tau^2} \Gamma(\mathbf{r}_1, \mathbf{r}_2, \tau), \quad (24)$$

$$\nabla_1^2 W(\mathbf{r}_1, \mathbf{r}_2, \omega) + k^2 W(\mathbf{r}_1, \mathbf{r}_2, \omega) = 0. \quad (25)$$

∇_1^2 is the Laplacian operator with respect to the position \mathbf{r}_1 . We can see that the propagation of the correlation functions is similar to the deterministic case when measuring at two independent points. However, if the two points of interest are not independent, the propagation of the correlation functions is more complicated, due to the two extra terms from the Laplacian operator [103]. To study broadband light propagation into biological samples or dynamic live-cell scattering, the statistical coherence theory is required to retrieve accurate results [104, 105].

2.2. Full-Field QPI Methods

2.2a. Spatial Phase Modulation: Off-Axis Interferometry

Quantitative phase information can be retrieved via spatial phase modulation or temporal phase modulation. In this subsection, we discuss the first case, where phase modulation is performed by an off-axis reference wave. The experimental setup is shown in Fig. 2 in the section of off-axis holography. The intensity at the detector is

$$I(x, y) = |U_r|^2 + |U_i(x, y)|^2 + 2 |U_r| |U_i(x, y)| \cos[k_{rx}x + \phi(x, y)]. \quad (26)$$

Figure 2

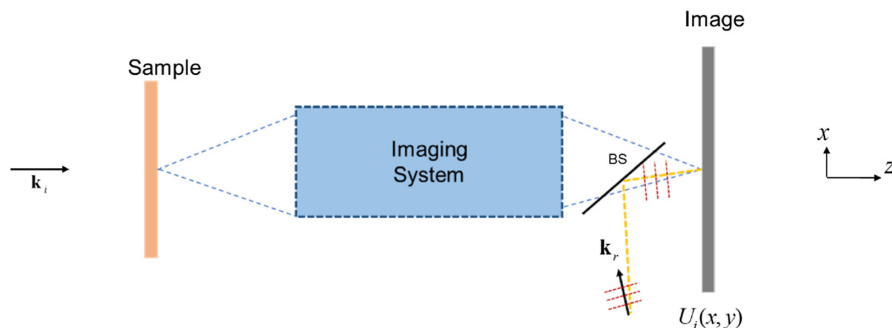


Diagram for off-axis interferometry. BS, beam splitter.

Applying a high-pass filter in the frequency domain can remove the DC term; thus the *cosine* term can be obtained, which is the real part of the complex correlation function. Hilbert transform of the real part yields the imaginary part of the correlation function

$$\sin[k_{rx}x + \phi(x, y)] = P \int \frac{\cos[k_{rx}x' + \phi(x', y)]}{x - x'} dx', \quad (27)$$

where P indicates the principal value integral. The highly wrapped phase can be retrieved as the argument of the complex correlation function

$$\phi(x, y) + k_{rx}x = \arg[\cos(k_{rx}x + \phi), \sin(k_{rx}x + \phi)]. \quad (28)$$

The k_{rx} term can be calculated with the known reference tilt angle. Thus, the final phase map ϕ is obtained by subtracting the modulation frequency term. Conventional off-axis interferometry has lower space-bandwidth coverage, meaning that either the resolution or the field of view must be compromised. However, slight off-axis interferometry has the problem of overlapping of the DC and AC signals. Techniques such as introducing a second color in the interferometry can resolve this problem [106].

2.2b. Temporal Phase Modulation: Phase-Shifting Interferometry

On-axis interferometry offers temporal phase shifts between the object field and the reference field, which preserves the space-bandwidth product, at the expense of the time-bandwidth product [107]. In Fig. 3, the intensity on the detector can be expressed as

$$I(\bar{\omega}\tau) = |U_r|^2 + |U_i(x, y)|^2 + 2 |U_r| |U_i(x, y)| \cos[\bar{\omega}\tau + \phi(x, y)], \quad (29)$$

where $\bar{\omega}$ is the central frequency of the reference field. To retrieve the information of ϕ , one can control $\bar{\omega}\tau$ to be different values and solve the equations for ϕ . Most common phase-shifting methods use four phase shifts with the increment of $\pi/2$. Therefore, the phase becomes

$$\phi = \arg [I(0) - I(\pi), I(3\pi/2) - I(\pi/2)]. \quad (30)$$

Phase-shifting QPI methods have demonstrated their capability for biological studies [108,109]. The imaging modalities using phase-shifting interferometry include

Figure 3

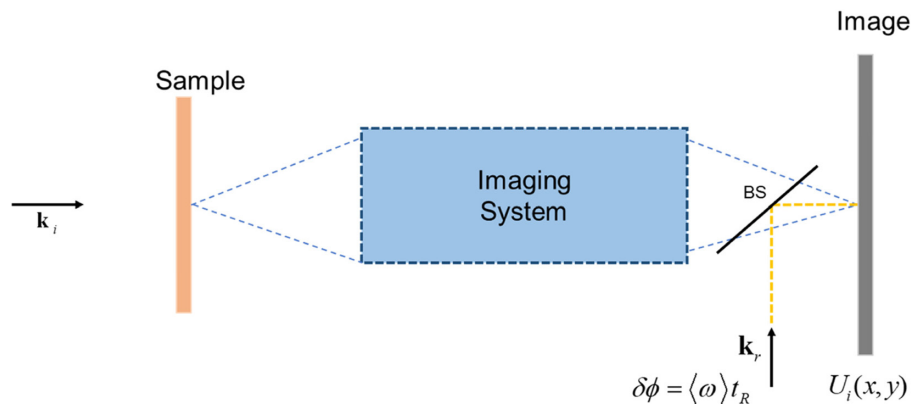


Diagram for phase-shifting interferometry. BS, beam splitter.

Fourier phase microscopy (FPM) [110], spatial light interference microscopy (SLIM) [111], and optical quadrature microscopy [112].

2.2c. QPI Figures of Merit

The main figures of merit of QPI are the acquisition rate, transverse resolution, temporal phase sensitivity, and spatial phase sensitivity [15]. The acquisition rate of QPI depends on the modality used for phase retrieval. The single-shot measurement is only limited by the camera, which can exceed 1000 frames per second at megapixel resolution. In this context, phase-shifting methods are slower since more frames are required, although possible approaches to achieve framerate parity include piezoelectric or electro-optical modulators.

Defining a proper measurement of transverse resolution in QPI is not trivial. It needs to consider the coherence properties of the system and also relies on different QPI methods. The common-path modality and the phase-shifting interferometry are more likely to preserve the diffraction-limited resolution. Off-axis methods reduce the information content of the hologram to about one-quarter of the pixel count, resulting in lower transverse resolution in the phase.

To assess the temporal stability experimentally, one can perform successive measurements of no-sample images. The histogram of the optical path length (OPD) can be obtained for the entire stacks of data, which yields the standard deviation of the data, defined as

$$\sigma_t = \sqrt{\langle [\delta\phi(t) - \langle \delta\phi(t) \rangle_t]^2 \rangle_t}, \quad (31)$$

where $\delta\phi(t)$ is the temporal phase fluctuation. Another way to describe the temporal phase noise is the temporal power spectrum by computing the Fourier transform of the no-sample stacks along time t :

$$|\delta\phi(\omega)|^2 = \left| \int \delta\phi(t) e^{i\omega t} dt \right|^2. \quad (32)$$

Similarly, the spatial phase sensitivity can also be calculated by taking no-sample images. The standard deviation for the entire field of view is defined as

$$\sigma_r = \sqrt{\langle [\delta\phi(x, y) - \langle \delta\phi(x, y) \rangle_{x,y}]^2 \rangle_{x,y}}. \quad (33)$$

Analog to the temporal power spectrum, the spatial power spectrum has the expression

$$|\delta\phi(x, y)|^2 = \left| \iint_A \delta\phi(x, y) e^{i(k_x x + k_y y)} dx dy \right|^2. \quad (34)$$

Figure 4 shows the histogram of the OPD in the spatial and temporal domains. One can obtain the temporal and spatial standard deviations by fitting the Gaussian curves. The spatiotemporal power spectrum is illustrated in Fig. 4 [113]. If the signal of interest lies in a certain frequency band, filtering can be used to significantly improve the signal-to-noise ratio (SNR) of the measurement.

The approaches to enhance the temporal phase sensitivity include passive stabilization, active stabilization, differential measurements, and common-path interferometry

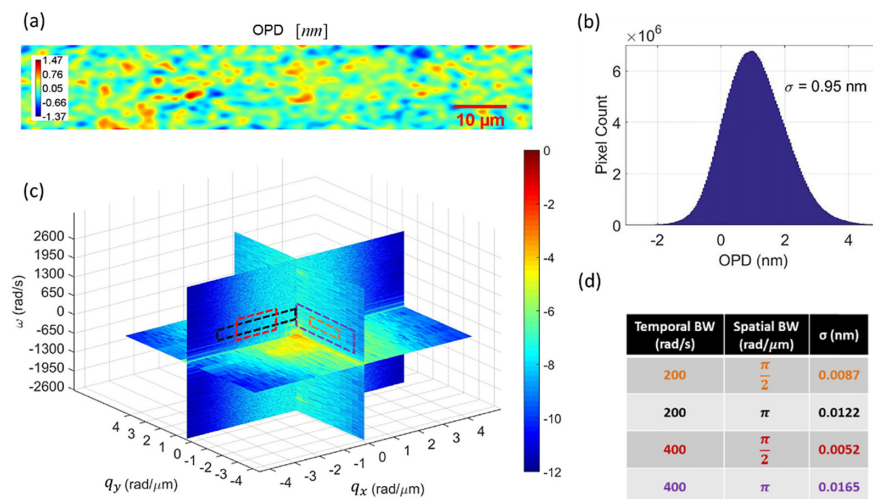
[114–116]. The spatial phase sensitivity can be improved by using the white-light source and keeping the optics pristine [117].

2.2d. Tomographic Methods Based on QPI

Tomography is one of the most important studies in QPI, aiming at solving the inverse scattering problem [118–120]. A large number of tomographic methods suitable for different scales and distinct types of biological samples are developed utilizing different parts of the spectrum of the electromagnetic fields [121–123]. X-ray computed tomography is a tomographic method based on Radon transform with a large number of applications in medicine and industry [124].

In 1969, Emil Wolf developed the theory, known as optical diffraction tomography (ODT), to reconstruct the object using the scattered fields [125]. ODT depends on either scanning the illumination angles or sample rotations to reconstruct the 3D object information [126–129]. The procedures of obtaining reconstructed tomograms with illumination rotation and cell rotation are illustrated in Figs. 5 and 6. However, to have the isotropic resolution in the reconstructed object, one needs to cover all the frequencies in the Ewald sphere by scanning the illumination angle through the entire solid angle 4π and taking the measurements over the entire solid angle (see details in Fig. 7) [130]. Most imaging modalities cannot cover all the frequencies in the Ewald sphere, a problem known as the *missing cone problem* [131]. Two categories of solutions were proposed to solve it. One is through the various iterative algorithms after the acquisition process, such as edge-preserving, total variation regularization, and the Gerchberg–Papoulis algorithm [132]. Another solution is through hardware improvement before the acquisition process, for example, in the 4π microscope, label-free light-sheet microscope, confocal microscope, and cell rotations by dielectrophoretic forces [129,133–135]. Machine learning can potentially mitigate the *missing cone problem*; the ground truth to train the network, however, is key to solving this problem [136,137].

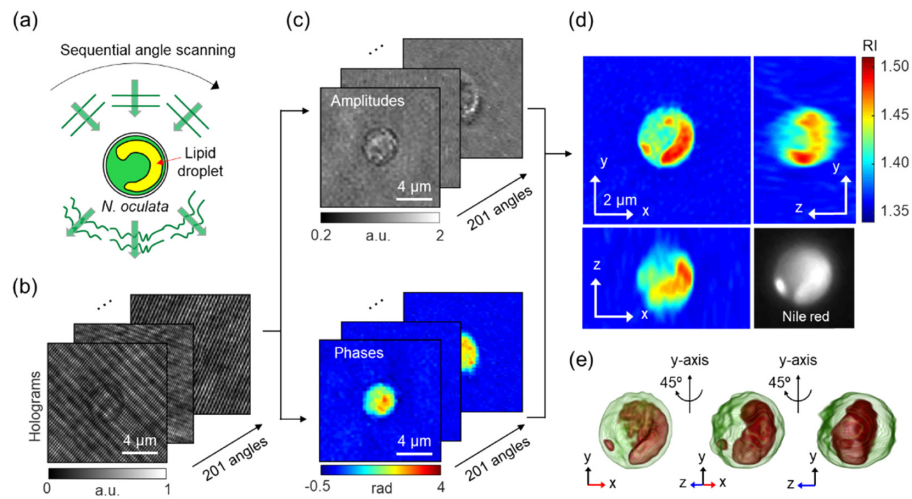
Figure 4



Analysis of spatiotemporal stability of the MISS microscopy system. (a) 256×1500 pixels no-sample OPD image with color bar in nanometers. (b) Histogram of the OPD stack acquired at 833 fps. (c) Plot showing the noise content of each spatial and temporal frequency component along three different planes in 3D frequency space. Color bar is in log scale with units of $\text{nm}^2 / ((\text{rad}^2 / \mu\text{m}^2)(\text{rad/s}))$. (d) Bandpass filtering over the spatiotemporal bands shown in (c) results in noise values orders of magnitude less than the total noise of 0.95 nm. Reprinted from [113].

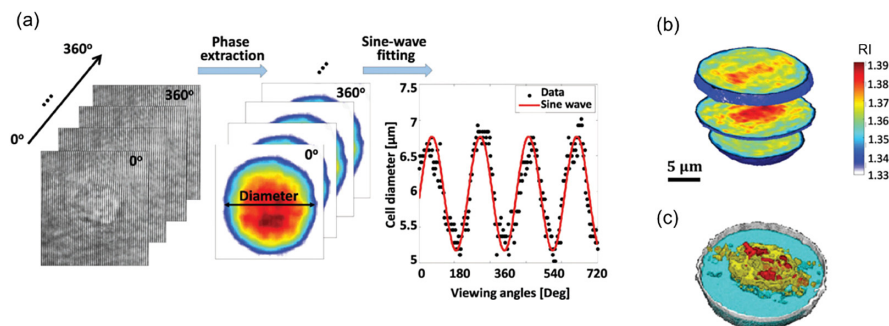
The original ODT was formulated with coherent illumination. However, wide-field microscopes with coherent illumination often suffer from speckles and other coherent artifacts, resulting in degraded contrast and resolution. Later on, several ODT techniques with partially coherent illumination were proposed [138–140]. We discuss two ODT techniques with partially coherent light, termed as white-light diffraction tomography (WDT) [141] and Wolf phase tomography (WPT) [103], in Subsection 4.3.

Figure 5



Schematic diagrams of the label-free identification of lipid droplets in individual *N. oculata* cells using ODT. (a) The sample is consecutively illuminated by a plane wave at various incident angles. (b) The holograms are recorded at 201 incident angles. (c) Retrieved amplitudes and phases of the optical fields diffracted by the sample. (d) Tomograms of the reconstructed 3D RI distribution of *N. oculata* in the $x - y$, $y - z$, and $x - z$ planes. The Nile red fluorescence image of the same cell is shown in the lower right corner for comparison. (e) 3D rendered iso-surface image of the reconstructed RI distribution at various viewing angles. Reprinted with permission from Jung *et al.*, *Sci. Rep.* **8**, 6524 (2018) [128]. Licensed under CC-BY 4.0.

Figure 6

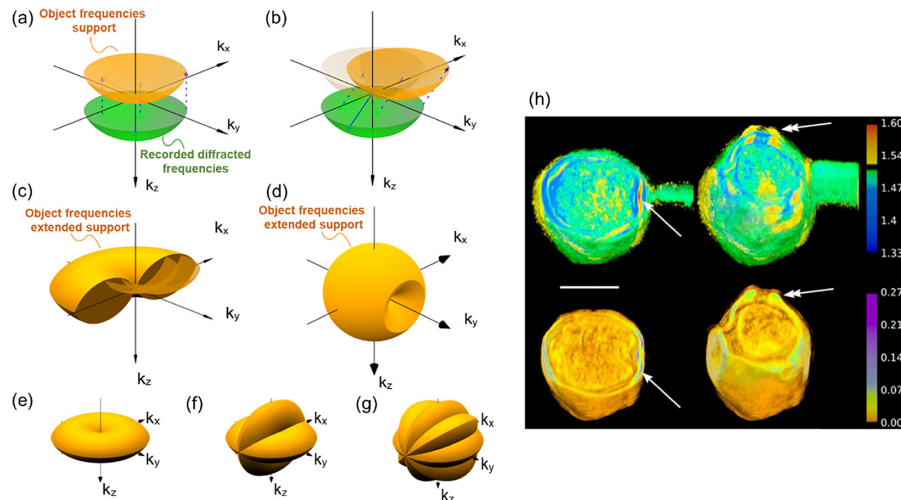


(a) Detection of the rotation cycle time and evaluation of the angle of the present point of view are done by fitting the cell diameter in the quantitative phase map during cell rotation to a sine wave. (b) 3D rendering and (c) rendered iso-surface plot of the refractive-index map of an MCF-7 cancer cell. Reprinted with permission from Habaza *et al.*, *Adv. Sci.* **4**, 1600205 (2017) [129]. Licensed under CC-BY 4.0.

As we mentioned in Subsection 1.2, tomographic methods such as OCT [142] and optical Doppler tomography [143] are interferometric techniques. Several non-interferometric tomographic methods based on the transport of intensity were also developed [144–146]. Fourier ptychographic tomography (FPM) and other synthetic aperture methods aim at improving the resolution in the 3D reconstruction [147–149]. Ghost tomography is based on the correlation between the known structured illuminating patterns and the total integrated intensity; the 3D object information can be reconstructed with Ghost imaging algorithms such as iterative cross-correlation via the Landweber algorithm [150,151].

To improve the penetration depth into the biological samples, photoacoustic tomographic methods combine the utilization of the electromagnetic fields with sound waves [152]. Diffuse optical tomography (DOT) uses diffusive photons to reconstruct the samples based on the transport equation of near-infrared light [153]. The forward model is based on the radiative transfer equation; however, the diffuse equation is often used because of the high computational load. The reconstruction algorithms are

Figure 7



Construction of the OTF for various configurations of TDM. (a) Digital holographic microscopy. The recorded k -vectors are shifted back according to momentum conservation to provide object vectors: the OTF depicts a cap of sphere of a large lateral, but limited, longitudinal extension. (b) When using inclined illumination in TDM-IR, the same positions of the recorded vectors provide new object vectors. (c) A large set of illuminations results in a filled and extended OTF: TDM-IR provides improved-resolution, higher-quality 3D images. Note, however, the presence of a so-called “missing cone” along the optical axis z , limiting longitudinal resolution and sectional capabilities. (d) OTF for TDM-SR. An almost completely filled sphere is obtained, but of lesser extension than in the previous case. (e) OTFs obtained for TDM-IRSR when combining TDM-IR with 0° , $(0^\circ; 90^\circ)$, and $(0^\circ; 45^\circ; 90^\circ; 135^\circ)$ specimen rotations [displayed at half-scale compared with (a)–(d)]. A missing-cone-free and extended support is obtained, showing that TDM-IRSR can deliver 3D, isotropic-, and improved-resolution images. (h) 3D complex RI of betula pollen grain observed with TDM. First row, real part of RI; second row, imaginary part of RI (absorption). Note the higher index of refraction of the pollen walls, especially near the pores (double-headed arrow), and the double-layer outer wall (arrow). Scale bar: 10 μm . Reprinted with permission from [130]. Copyright 2017 Optical Society of America.

categorized into linearization approaches based on Born or Rytov approximations and nonlinear iterative approaches [154].

3. PRINCIPLES OF SLIM

3.1. Theory

3.1a. Zernike Phase-Contrast Microscope

The phase information of the object is hidden in bright-field microscopic images. In the 1930s, Zernike solved this problem by inserting a $\pi/2$ phase retarder in the objective pupil plane, introducing extra $\pi/2$ phase delay between the incident and scattered fields [18]. As a result, the information of the phase object can be retrieved quantitatively from four intensity images. We can illustrate this based on the scattering theory discussed in Subsection 2.1a. Recall that, for phase objects, the total field of the forward scattering under the first-order Born approximation and paraxial approximation has the form [91]

$$U_f(r_{\perp}, z, \omega) = A(\omega)e^{i\beta z} \{1 - i\beta [n(r_{\perp}, \omega) - n_0] L\}. \quad (35)$$

Thus, the intensity can be calculated as

$$\begin{aligned} I &= U_f U_f^* \\ &\simeq A^2(\omega). \end{aligned} \quad (36)$$

We can see that the information of the weak phase object is lost in conventional bright-field microscopy. After inserting a phase $\pi/2$ retarder into the incident field, the forward scattering field becomes

$$\begin{aligned} U_{\text{PC}}(r_{\perp}, z, \omega) &= A(\omega)e^{i\beta z} \{i - i\beta [n(r_{\perp}, \omega) - n_0] L\} \\ &= A(\omega)e^{i\beta z} i \{1 - \beta [n(r_{\perp}, \omega) - n_0] L\}. \end{aligned} \quad (37)$$

Now the intensity has the expression

$$\begin{aligned} I_{\text{PC}}(x, y) &= U_{\text{PC}} U_{\text{PC}}^* \\ &\simeq A^2(\omega) \{1 - 2\beta [n(r_{\perp}, \omega) - n_0] L\}^2. \end{aligned} \quad (38)$$

It can be seen that the object information appears as a linear term in the intensity of the phase-contrast microscope, resulting in a much higher contrast for phase objects. The diagram of Zernike's phase-contrast microscope is presented in Fig. 8. In the objective pupil plane, Zernike introduced a phase retarder to give a $\pi/2$ shift to the unscattered field. This filter also attenuates the unscattered field to further decrease the background light. In commercial microscopes, the pupil function is designed to match the annular illumination given by

$$P(r) = \begin{cases} 1 & r < R_i \\ \pm ai & R_i \leq r \leq R_o \\ 1 & R_o \leq r \leq R \end{cases}, \quad (39)$$

where R_i and R_o are the inner and outer radii of the ring retarder, R is the radius of the aperture, and the \pm sign corresponds to positive and negative phase contrast.

3.1b. Phase Retrieval in SLIM

SLIM is implemented as an add-on module to the commercial phase-contrast microscope, it combines the spatial uniformity associated with white-light illumination and the stability of common-path interferometry [111,155]. The schematic setup is illustrated in Fig. 9(a). The spatial light modulator (SLM) in the add-on module provides further phase shifts in the pupil plane with increments of $\pi/2$, and the active pattern on the SLM is calculated to precisely match the size and the position of the objective phase-ring image. As a result, the phase delay between the scattered and unscattered fields is controlled and the four images corresponding to each phase shift are recorded on the camera.

The white-light illumination in SLIM can be considered as spatially coherent, but temporally of low coherence. The phase information in SLIM can be understood as that of an effective monochromatic field oscillating at the average frequency of the broadband fields. For broadband fields, the cross-spectral density of the incident and scattered fields is defined as

$$W_{is}(\mathbf{r}, \omega) = \langle U_i^*(\omega) U_s(\mathbf{r}, \omega) \rangle, \quad (40)$$

Figure 8

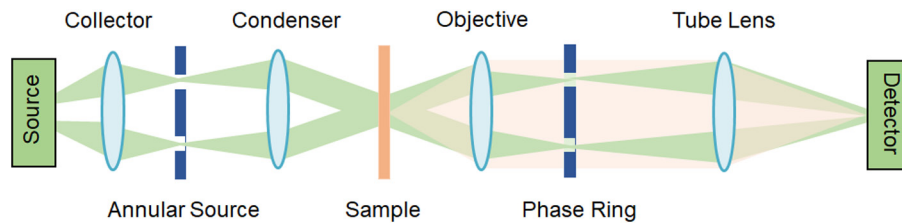
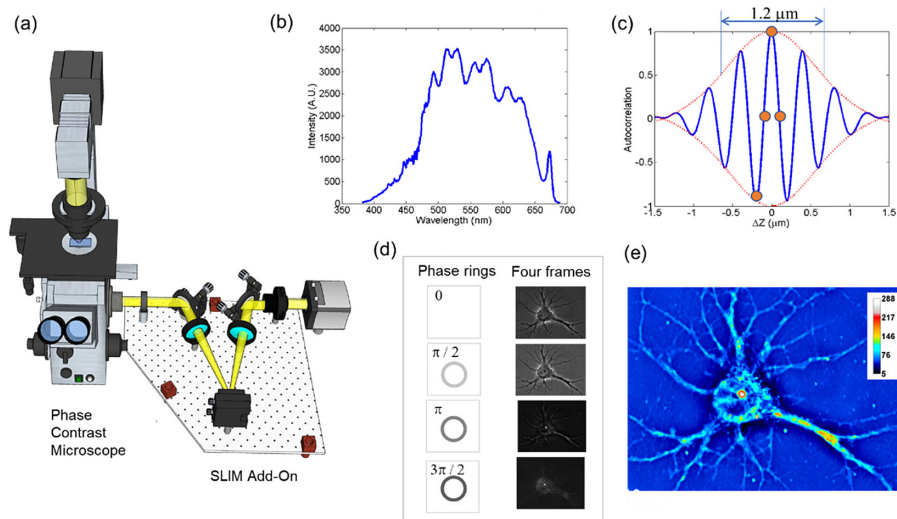


Diagram of Zernike phase-contrast microscopy.

Figure 9



SLIM principle. (a) Schematic setup for SLIM. (b) Spectrum of the white light emitted by the halogen lamp. The center wavelength is 552.3 nm. (c) Autocorrelation function (blue solid line) and its envelope (red dotted line). The four circles indicate the phase shifts produced by SLM. (d) Phase rings and their corresponding frames recorded by the camera. (e) SLIM quantitative phase image of a hippocampal neuron. The color bar indicates optical path length in nanometers. Reprinted with permission from [111,161]. Copyright 2011 and 2018 Optical Society of America.

where U_i and U_s are the incident and scattered fields, \mathbf{r} is the spatial coordinate, and ω is the frequency of the light. The total field on the image plane is thus

$$\begin{aligned} U(\mathbf{r}, \omega) &= U_i(\omega) + U_s(\mathbf{r}, \omega) \\ &= |U_i(\omega)| e^{i\phi_0(\omega)} + |U_s(\mathbf{r}, \omega)| e^{i\phi_1(\mathbf{r}, \omega)}. \end{aligned} \quad (41)$$

$\Delta\phi(\mathbf{r}, \omega) = \phi_1(\mathbf{r}, \omega) - \phi_0(\omega)$ is the phase delay between the incident and scattered fields. For most transparent specimens of interest here, we consider the dispersionless case, i.e., ϕ independent of ω . With the mean frequency ω_0 of the broadband fields, the cross-spectral density can be expressed as

$$W_{is}(\mathbf{r}, \omega - \omega_0) = |W_{is}(\mathbf{r}, \omega - \omega_0)| e^{i\Delta\phi(\mathbf{r})}. \quad (42)$$

The temporal autocorrelation function is obtained by taking the Fourier transform of Eq. (42) with respect to ω ,

$$\Gamma_{is}(\mathbf{r}, \tau) = |\Gamma_{is}(\mathbf{r}, \tau)| e^{i[\omega_0\tau + \Delta\phi(\mathbf{r})]}. \quad (43)$$

The phase map retrieved from phase-shifting measurements is equivalent to that of coherent monochromatic light at frequency ω_0 . The intensity in the plane of interest is thus a function of the time delay as

$$I(\mathbf{r}, \tau) = I_i^2 + I_s^2 + 2 |\Gamma_{is}(\mathbf{r}, \tau)| \cos[\omega_0\tau + \Delta\phi(\mathbf{r})]. \quad (44)$$

The magnitude of the correlation function $|\Gamma_{is}(\mathbf{r}, \tau)|$ around $\tau = 0$ can be assumed to vary slowly at each phase shift. Therefore, the phase delay between the incident and scattered fields can be calculated as

$$\Delta\phi(\mathbf{r}) = \tan^{-1} \left[\frac{I(\mathbf{r}, \tau_3) - I(\mathbf{r}, \tau_1)}{I(\mathbf{r}, \tau_0) - I(\mathbf{r}, \tau_2)} \right], \quad (45)$$

where $\tau_j = j\pi/2$, $j = 0, 1, 2, 3$. If we define $a(\mathbf{r}) = |U_s(\mathbf{r})|/|U_i|$, then the phase delay between the incident and the total fields can be reconstructed as

$$\phi(\mathbf{r}) = \tan^{-1} \left[\frac{a(\mathbf{r}) \sin[\Delta\phi(\mathbf{r})]}{1 + a(\mathbf{r}) \cos[\Delta\phi(\mathbf{r})]} \right]. \quad (46)$$

From four successive intensity measurements for each phase shift [Fig. 9(d)], the phase information of the object is retrieved [Fig. 9(e)]. The spectrum of the halogen lamp is presented in Fig. 9(b). The real part of the autocorrelation function Γ_{is} (blue solid line) and its magnitude (red dotted line) are depicted in Fig. 9(c). The four circles show the phase shifts produced by the liquid crystal phase modulator (LCPM).

Figure 10 compares the spatial accuracy of SLIM and atomic force microscopy (AFM) by imaging an amorphous carbon film deposited on glass. The topography measurements by SLIM and AFM, respectively, are presented in Figs. 10(a) and 10(b). The two types of measurements agree within a fraction of a nanometer. Unlike AFM, SLIM is non-contact, parallel, and faster by more than 3 orders of magnitude. Thus, SLIM can optically measure an area of $75 \mu\text{m} \times 100 \mu\text{m}$ in 0.5 s compared to a $10 \mu\text{m} \times 10 \mu\text{m}$ field of view measured by AFM in 21 min. To further compare to diffraction phase microscopy (DPM), an off-axis laser-based technique that was interfaced with the same microscope, the background images (i.e., no sample) from SLIM and DPM are shown in Figs. 10(d) and 10(e). SLIM's spatial uniformity and accuracy

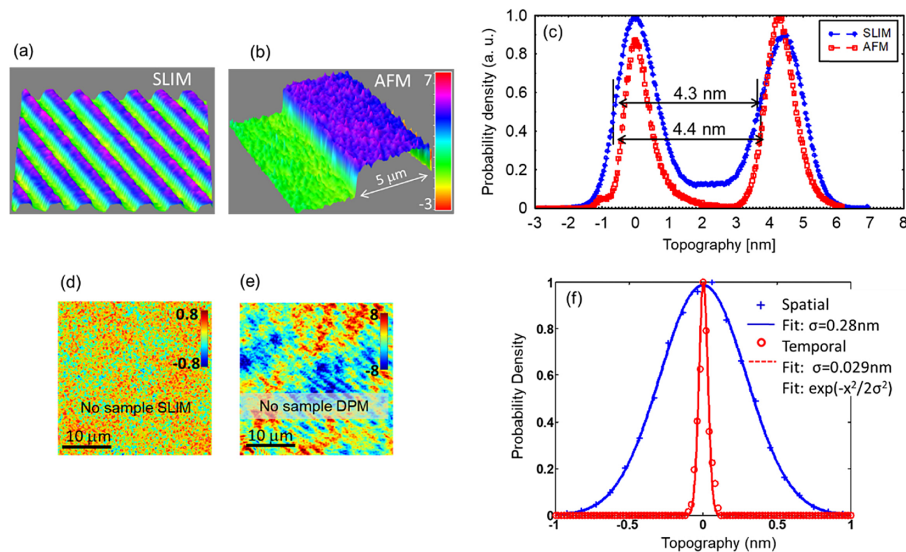
for structural measurements are substantially better than DPM's due to the lack of speckle effects granted by its white-light illumination. To quantify the spatiotemporal phase sensitivity, a 256-frame stack of background images was obtained using SLIM. Figure 10(f) illustrates the spatial and temporal histograms associated with the OPD shifts across a $10\ \mu\text{m} \times 10\ \mu\text{m}$ field of view and over the entire stack. These noise levels, 0.3 nm, and 0.03 nm represent the limit in OPD sensitivity across the image and between frames, respectively.

3.1c. Halo Removal

Because the illumination in phase-contrast microscopy is not perfectly spatially coherent, the images in SLIM are affected by a coherent artifact, known as the phase-contrast “halo,” which resembles a glow around the edges of the cell. In SLIM, as in phase-contrast microscopy, a phase ring at the pupil plane is used to controllably delay the transmitted light relative to the scattered light. The final result is a greatly improved sensitivity to OPD shifts [18].

This ring illumination creates a spatial coherence area that is generally smaller than the field of view. As such, in reality, the description of image formation that assumes the imaging instrument can unambiguously separate “scattered” and “transmitted” components is an idealization (Fig. 11) [139]. In phase-contrast microscopy and SLIM, actual components of the modulated field are determined by the shape of the phase-contrast pupil as well as the coherence properties of the illumination. In practice, the illuminating pupil cannot be made too small [156]; thus practical designs lead to the introduction of cross-talk between the scattered and transmitted fields [139]. In effect, a low-resolution version of the object is imparted into the reference field, which leads to an unwanted halo-like glow around the sample [Fig. 12(a)]. This effect is particularly acute for low-frequency structures such as flat semiconductors while

Figure 10



SLIM figures of merit. (a) SLIM image of an amorphous carbon film (40X/0.75NA objective). (b) AFM image of the same sample. The color bar indicates thickness in nanometers. (c) Topographical histogram for AFM and SLIM, as indicated. (d) No-sample background of SLIM. (e) No-sample background of DPM. (f) Optical path-length noise level measured spatially and temporally. The solid lines indicate Gaussian fits, with the standard deviations as indicated. Reprinted with permission from [111]. Copyright 2011 Optical Society of America.

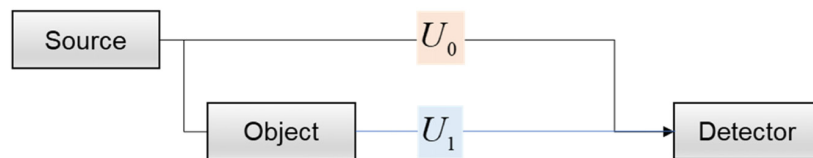
being almost absent in intracellular details such as nucleoli or mitochondria. As the SLIM image is a faithful measurement of the field associated with the phase-contrast microscope, it, too, suffers from halos.

Unlike phase contrast, where the amplitude is coupled to phase, performing phase interferometry, SLIM recovers the deterministic signal associated with the optical field, which, in turn, provides a computational strategy to remove the halo artifacts [157]. The most complete model for halo formation is presented in [158], where the authors use a variation of the transmission cross coefficients (TCC) to model image

Figure 11

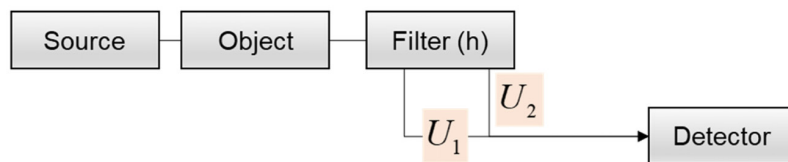
(a) Traditional Interferometry

$$I \propto |U_0||U_1|\cos(\phi)$$



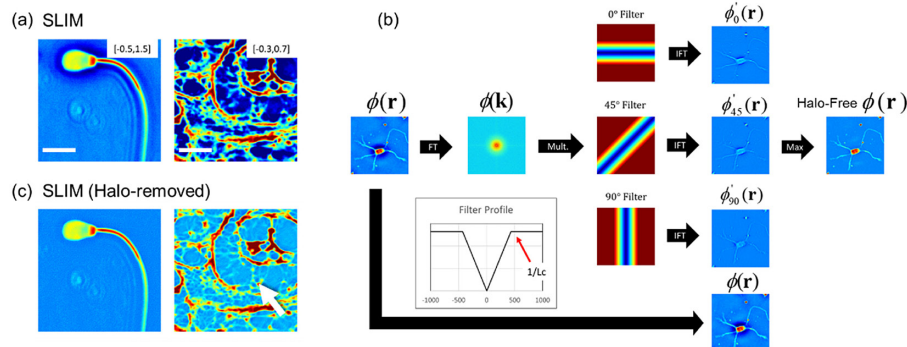
(b) Common-Path Interferometry

$$I \propto |U_1||U_2|\cos(\phi - \phi \otimes h)$$



In traditional interferometry, interference occurs between the scattered field (U_1) and reference field (U_0), while in common-path configurations the reference field U_2 is generated from the sample.

Figure 12



(a) Halo artifact appears as unwanted glow around the specimen (sperm and tissue biopsy, $40\times/0.75$ SLIM). (b) The halo artifact can be partially corrected by using a nonlinear computational algorithm. In the direct halo removal algorithm, a series of directional derivative images is combined with the original image using a pixel-wise maximum. (c) The resulting SLIM images highlight details that were previously submerged by the halo (white arrow).

formation (Hopkin's TCC) [159,160]. In general, a TCC-based approach is difficult to invert, motivating the authors to simplify image formation to [161]

$$\phi_m(\mathbf{r}) = \phi(\mathbf{r}) - \arg [e^{i\phi(\mathbf{r})} \odot_r h(\mathbf{r})]. \quad (47)$$

Here, ϕ_m is the measured SLIM image, ϕ is the desired phase associated with the object, and $h(\mathbf{r})$ is an impulse response-like function related to the condenser and illumination shape that captures the spatial incoherence of the system. Noting that the Fourier transform of $h(\mathbf{r})$, $h(\mathbf{k})$ resembles the physical aperture, we see that as $h(\mathbf{k})$ approaches a pinhole, $h(\mathbf{k}) \approx \delta(\mathbf{k})$ in Eq. (47), we recover the phase without error: $\phi_m(\mathbf{r}) \approx \phi(\mathbf{r})$. In practice, $h(\mathbf{k})$ is built into the microscope. While $h(\mathbf{k})$ can be adjusted via the condenser aperture in bright-field instruments, in phase-contrast microscopes, the apertures do not permit easy manipulation as they are matched to the phase rings inside the objectives. This approach was extended to 3D imaging by approximating the halo as a linear high-pass filter [162].

Using the observation that the halo artifact mostly corrupted low-spatial frequencies, a nonlinear filtering technique was proposed, using directional derivatives [161] (Fig. 12). In this method, a series of images is collated by taking the pixel-wise maximum of the derivative images and the original halo-corrupted image. Importantly, this approach is non-iterative and can be applied to real-time operations without the need to measure complicated impulse responses.

3.2. Instrumentation

3.2a. Alignment and Calibration

In SLIM, an active modulating element introduces controlled phase shifts at the pupil plane, modulating the delay between the scattered and transmitted light. The resulting implementation resembles an external form of phase contrast with a tunable phase ring. When compared to off-axis methods [163], by using a series of temporal modulations to acquire the complex field, SLIM trades temporal bandwidth (more images) for spatial bandwidth (better use of the camera sensor) in a way that improves image quality.

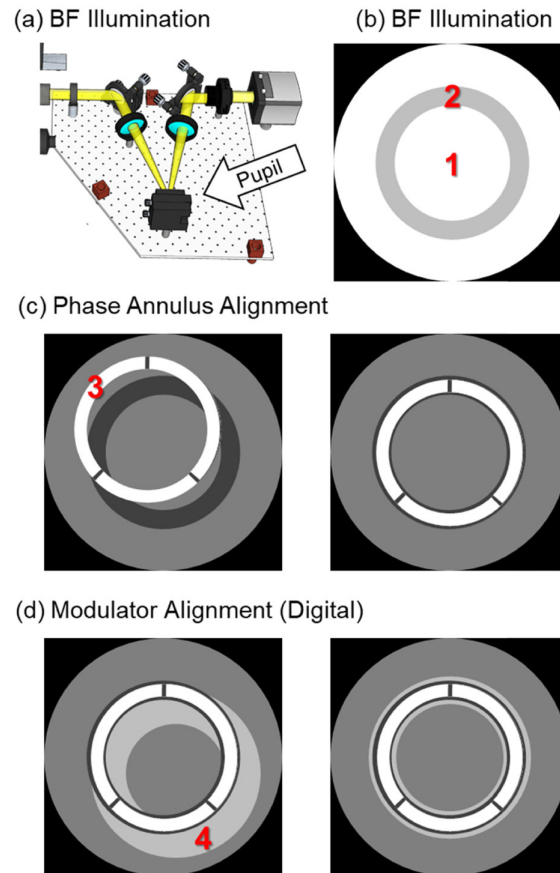
SLIM performs modulation on a pupil plane conjugate to the back focal plane of the objective (phase ring of the objective). This reduces fixed pattern noise as the fringes are generated at the pixel level, in time, by modulating a retarder rather than spatially, with an off-axis reference field. At this plane, misalignment introduces directional shading rather than a grid-like pattern. In practice, misalignment rarely occurs as the ring-like illumination and attenuation from the phase-contrast objective provide a convenient fiducial marker for alignment (Fig. 13).

By far the most popular method to modulate a ring shape involves the use of a SLM [164]. This device contains a digitally addressable grid of pixel-like variable retarders, each of which uniquely modulates the polarization state of one polarization relative to another. For SLIM imaging, these are mostly reflective devices, although at least one attempt was made to use a lower cost twisted nematic transmission SLM [165]. Other authors have noted that the same SLM can be multiplexed for optical trapping [166].

The relationship between the instrument's defined voltage units or "gray levels" and the imparted phase shift depends on the illumination spectrum and detector response. In practice, this relationship is determined on a per-instrument basis by recording a sequence of amplitude images with increasing phase modulation. In the case of SLMs, this is accomplished by placing the modulator between crossed polarizers.

The resulting amplitude curves can be analyzed using a Hilbert transform technique where a complex analytic signal is constructed from the measured data by performing a Hilbert transform [111] [Figs. 14(b) and 14(c)]. The argument of this complex analytic signal yields the instantaneous phase response at the configured gray level. In practice, the Hilbert transform is calculated by way of the fast Fourier transform, which requires continuity and periodicity assumptions to be met [167]. Further, SLMs have fixed modulation levels leading to discretization errors. This problem is particularly acute as the number of actual gray levels is only a fraction of the total addressable range. For example, a common SLM may provide 50 gray levels over an

Figure 13



Alignment of a commercial SLIM system. (a) The SLIM add-on interferometer is implemented as a 4-f system with a reflective spatial light modulator manipulating the pupil plane of a commercial phase-contrast microscope. For alignment, an additional lens with an integrated analyzer is positioned after the pupil plane. (b) SLIM alignment begins by configuring the microscope into bright-field illumination. Here #1 is the bright background due to a fully open condenser and #2 represents the attenuation due the phase ring typical of phase-contrast objectives. The square root of the average intensity values between #1 and #2 is a per-objective attenuation constant used during the image reconstruction process. (c) Next, the microscope's condenser is configured for phase-contrast illumination. #3 shows the illumination ring, which is then aligned to the match the objective's phase ring. (d) Lastly the modulation (#4) is aligned to the phase ring by digitally adjusting the pattern on the spatial light modulator. In general, this procedure must be performed for each objective, and in some cases a zoom lens immediately before the add-on module is used to adjust the location of the pupil plane on a per-objective basis.

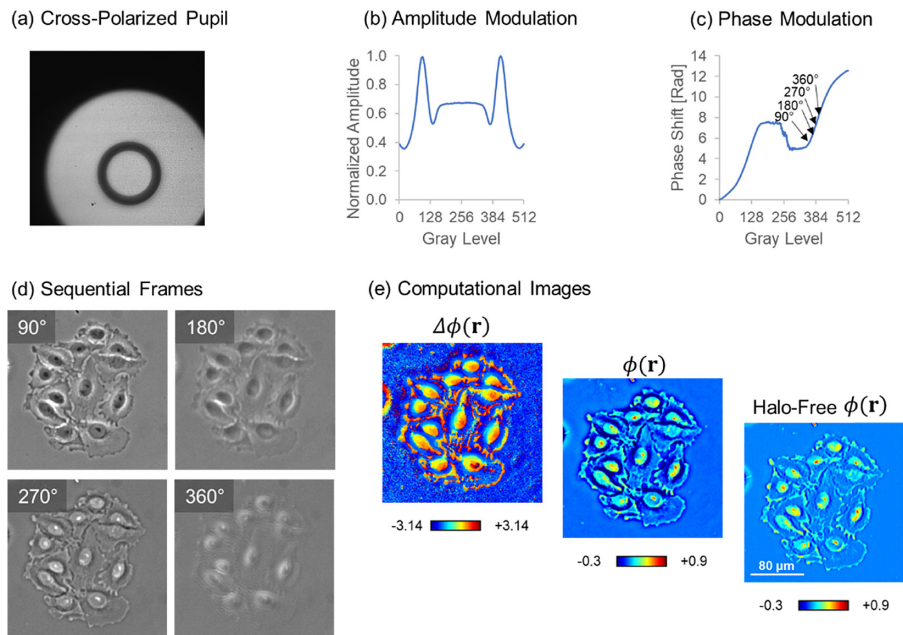
addressable range of 256 values (8-bit). One proposed solution to increase the number of gray levels is to write a checkboard style dithering pattern where neighboring pixels are averaged to achieve an intermediate discrete phase-shift value [158], although a more robust method involves refining the reconstruction formulas to match the discrete phase shifts [95].

As SLIM is rate-limited by the speed of the SLM, some authors have explored using mirrors attached to piezoelectronics to improve frame rates [47,48]. For example, in [47] the authors used a three-step phase-shifting algorithm to achieve 50 Hz imaging (reported as 150 Hz with “interlacing”). So far, these efforts have fallen short of the potential imaging rates due to trouble synchronizing acquisition with camera exposure. For example, these attempts used software triggering, which uses an extra readout step and effectively halves frame rates when compared to continuous acquisition. Further, most implementations wait for the SLM to stabilize (stop-and-go) instead of performing modulation simultaneous with camera acquisition (bucket integration) [119]. An unsolved challenge with mirror-based approaches is the need to adjust the modulating element on a per-objective basis. In a parallel development, overdrive techniques have pushed SLM switching times to the kilohertz regime where light budget concerns begin to dominate [168]. These advances make SLM-based approaches more competitive.

3.2b. High-Throughput Acquisition

Besides the SLM, the throughput of a SLIM system depends on the extent to which the acquisition process is parallelized [169]. In general, the SLIM acquisition process involves translating the stage or focus, introducing a phase shift, exposing the

Figure 14

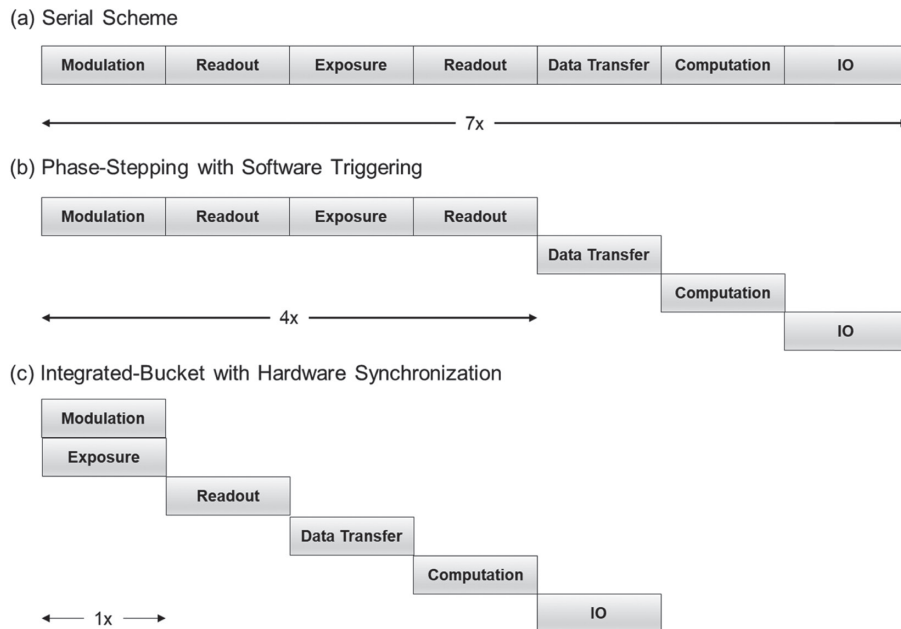


Spatial light modulators consisting of a grid of addressable variable retarders capable of imparting a phase shift at each pixel. The relationship between the digitally controlled phase value and the actual achieved phase delay depends on the spectral properties of illumination and is usually calibrated for each light source. (a) One calibration strategy involved inserting a lens containing a polarizer to visualize the pupil plane. (b) A series of images is acquired with increasing phase modulation producing an amplitude curve (Meadowlark XY series, shown). (c) A Hilbert transform is used to find the instantaneous phase shift associated with each gray level. (d) Captured four frames after calibration. (e) Reconstructed phase maps.

camera, reading out the image, phase retrieval, rendering the result, and saving the data. Figure 15 presents three possible acquisition schemes; a serial version, a parallel version, and a theoretically optimal, but yet unrealized, variant. Unsurprisingly, the optimal version performs 10x faster than the serial version.

In early implementations of the SLIM design, the rate-limiting factors were found to be computational [170], yet in more modern revisions, the rate-limiting steps are reported to be the exposure time or SLM stability. In a broader context, the shift from computational back to optical limitations highlights a trend in imaging where computational techniques have advanced faster than the optical elements. This is likely to remain the case as computing bottlenecks (GPUs or hard drives) can be scaled by adding more computing hardware while similar approaches do not apply to the construction of an optical crystal. Notably, the theoretically optimal performance remains unrealized. While this would appear to be strictly due to deficient software implementation, in reality, it is difficult to implement bucket integration with a digitally controlled device. This is because a sinusoid rather than a fixed level signal must be supplied to the SLM elements. Achieving a smooth sinusoidal modulation, rather than a unique-wave form for each modulation [168], requires a yet to be realized calibration procedure or some other fundamental change in the existing SLM hardware.

Figure 15



(a) Serial SLIM acquisition is the most popular computational imaging scheme for home-built instruments. In that scheme, all steps of the acquisition process are performed in series. (b) The commercial instrument implements a more advanced scheme where hardware events are overlapped with computation. The principal limitation of this scheme is due to the need to discard extra charge during software triggering. In software triggering modes the camera must discard the charge on the detector to ensure correct exposure time by performing a charge readout, which effectively halves frame rates. The advantage of software triggering and hardware analogs is that a variable amount of time can elapse before the image is recorded. Thus, this mode is preferred when the microscope is expected to move before each acquisition. (c) A potentially faster but unrealized approach exists where camera exposure is overlapped with modulation.

In general, image acquisition and computation can occur in parallel, meaning that the current image can be processed while the next one is acquired. An important but often understated limitation is that not all programming languages are well suited for task-parallel operations. For example, C++, C#, or LabView have individually addressable threads, but those constructs are more challenging to use in Python or MATLAB. This design limitation is evident by the choice of language used in some SLIM implementations. In [111], LabView was used to control the modulator, while stage and camera control was performed by the microscope control software (Zeiss, AxioVision). In [170] the authors used a combination of C++ (backend) and C# (frontend), while the Cell Vista Pro (PhiOptics Inc) is written in C++ and uses Qt as the widget kit to facilitate parallelized rendering.

When imaging with SLIM and fluorescence microscopy, one needs to take into account that the SLIM add-on module reduces the intensity by approximately half, due to the polarizer in the optical path. If necessary, for higher sensitivity fluorescence measurements, one can also use a second separate port of the microscope. The SLIM software can automatically switch between the two ports, with a switching time of 0.7 s.

3.2c. Whole Slide Imaging

Multiscale experiments such as high-content phenotypic screening [171], or 4D imaging of mesoscopic structures [172], present challenges to image acquisition and data storage [173]. As a point of reference, a free-running 5 MP camera is capable of producing approximately 4 TB of data in an hour [174]. To obtain ample storage, most authors have preferred to use a combination of high-speed networking and large hard drive arrays [175]. While such strategies are often able to meet total data storage requirements, throughput is often difficult to achieve, especially when data redundancy is required [176]. For example, RAID 6 parity reduces throughput by six times. Further, achieving optimal performance requires using multiple threads to saturate the write cache, and ensure that the hard drives are constantly writing/reading. An alternative strategy for burst imaging is to use solid-state-based storage [177], which affords more throughput at a lower cost but comes at a fraction of the storage capacity [178]. Thus, to achieve both high throughput and total capacity, some authors have preferred a combination of SSDs and external storage. In this case, acquired data are written onto an SSD disk and a multithreaded copy (robocopy.exe) is used to perform data transfer. This approach is well suited to storage computers running Windows, which, unlike Linux (Samba), supports multithreaded data transfer [179]. Further, using an intermediate local drive introduces a measure of tolerance for network disruptions.

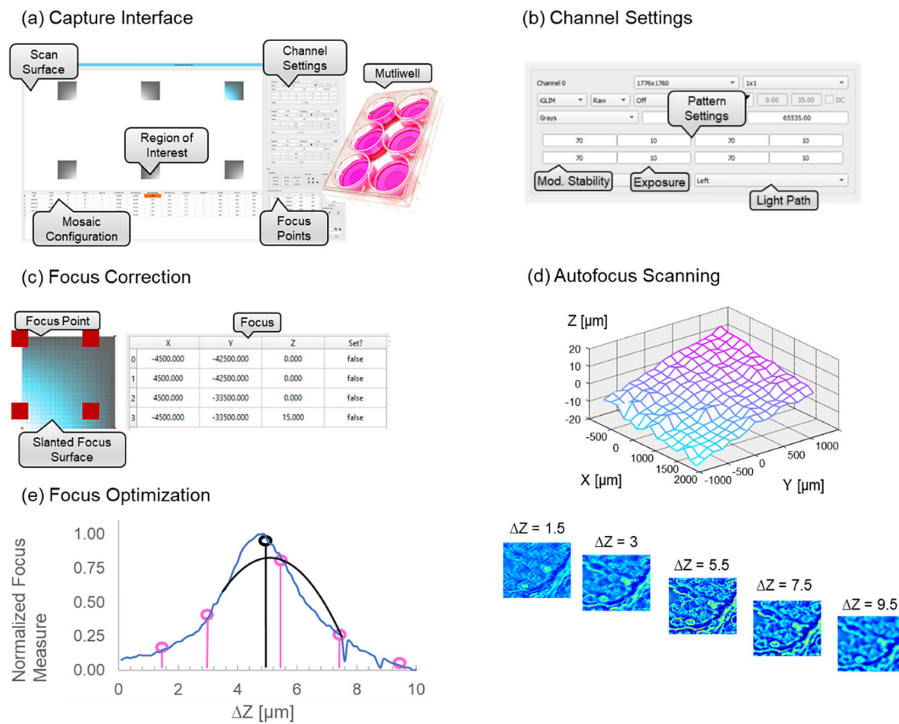
In addition to challenges due to computer storage constraints, it was found that a purpose-built graphical user interface and digitization strategies are crucial for SLIM's operation. The Z-focus is controlled using the piezo stage in the microscope; the resolution is tens of nanometers. One difficulty was in maintaining focus when imaging large surfaces such as microscope slides or multiwell plates (128 mm × 85 mm). In [169] the authors developed an axial scanning technique where the plane of best focus is determined by finding the point where the variance of the phase within mid-range frequency bands is maximized (Fig. 16). This strategy is typically impractical as a large number of axially scanned samples need to be acquired, yet it was found that in most cases the plane of best focus resembled a tilt (due to the sample being slightly tilted), which in turn improved the speed of the autofocus algorithm. Further, with phase imaging and interpolation, it was possible to reduce the number of axial samples to five. To scan samples with discrete regions (such as multiwells) a graphical interface was developed to represent the plane of best focus as a collection of "focus points." These points were then used to construct a

Delaunay triangulation for interpolating the focus at each mosaic tile [171]. In practice, this procedure is relatively quick with less than a second used to optimize each mosaic tile.

3.2d. Mosaic Tile Registration

To acquire samples larger than the field of view, SILM relies on a stage scanning strategy, where a series of high-resolution mosaic tiles are composited to form a larger image. While this strategy has the advantage that individual frames do not suffer from motion blur and that samples much larger than the objective can be acquired [180], the motion of the microscope stage introduces rigid misalignment that must be compensated through digital methods. The most popular method to perform rigid image registration relies on identifying the peak values in the cross correlation [181] and merging disagreements between neighboring tiles using a least-squares approach [182]. It was found that this algorithm was well suited to GPU computation and that the rate-limiting factor was disk access, motivating a caching strategy to avoid redundant reads [169]. A challenge with phase correlation is that dense regions of the

Figure 16



Graphical user interface to configure complex imaging experiments (such as those involving multiwells) including SLIM imaging specific features. (a) The capture interface enables scanning multiple regions of interest with separate focusing points. (b) Channels such as fluorescence microscopy are presented side-by-side with phase imaging specific features such as control with exposure and modulator stability on a per-pattern basis. (c) To account for variations in the plane of best focus, a Delaunay triangulation constructed from “focus points” is interpolated to determine the ultimate coordinates of each mosaic tile. (d) Some slide scanning instruments include an auto-focusing feature where a small through-focus stack is acquired offset from a manually configured plane of best focus. (e) Following a focus optimization scheme, the most in-focus position (black) is selected from a series of sub-optimally focused images (pink, shown).

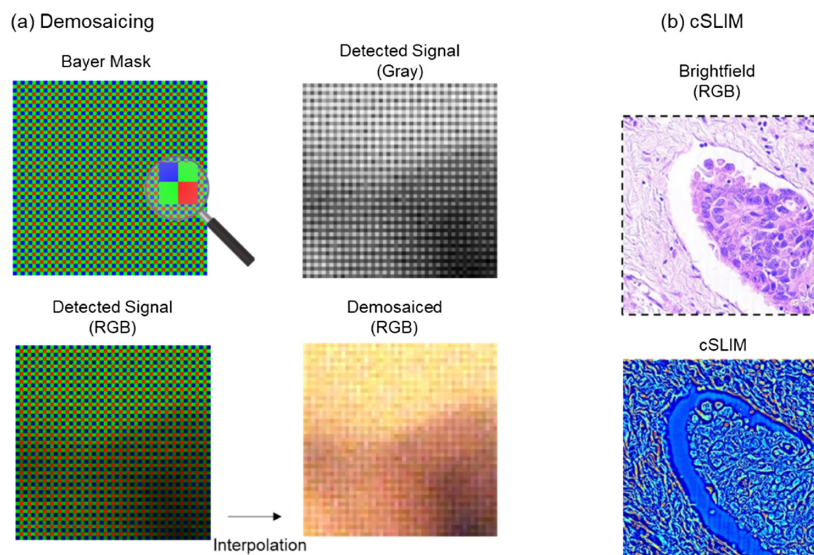
sample produce spurious or unwanted peaks in the cross correlation between neighboring regions. This problem is addressed by searching for peaks within a limited window, which is adjusted iteratively [158]. Further error suppression occurs by performing phase correlation on background-corrected images, with the background generated by averaging a large number of images acquired during the experiment.

3.2e. SLIM with a Color Camera

Most pathology applications rely on colored stains such as H&E to introduce specificity for cellular structures such as nuclei and cytoplasm. To facilitate co-localized QPI and histopathological imaging, a variant of SLIM was developed using a bright-field objective and color camera. This setup enabled the authors to acquire co-localized gray-scale SLIM and stain images such as H&E (Fig. 17) [183]. While H&E images are rendered in full color, the SLIM image contains a single channel and represents the composite of the three colors on the detector. Importantly, it was found that the microscope's illumination spectrum was, on average, green, which lies between the red and blue of the H&E stain, reducing dispersion-related errors. An alternative strategy is to treat each color channel independently producing a three-color phase map from a single phase-shifting sequence.

In most color cameras, the field is sampled by a specialized Bayer mask consisting of a chromatic filter (RGB) at each pixel [184]. As only one color is detected at each position, a demosaicing interpolation procedure is performed to estimate the missing color values from neighboring elements. This procedure introduces additional computational considerations as industrial camera vendors often do not supply adequate

Figure 17



(a) Most color imaging sensors consist of a Bayer mask where every pixel has a preferential spectral sensitivity. The acquired data contains a single gray level at each pixel that can be interpreted as a color value (detected signal). As part of routine processing, the missing color information is interpolated so that each pixel contains three values corresponding to red, green, and blue (demosaiced). (b) The color imaging instrumentation was used for cSLIM, where ring illumination was used in conjunction with a bright-field objective to form what resembled a conventional bright-field image when the SLM acted as a mirror. As outlined in that work, the three-color channels were reweighted to produce a gray-scale image that was subsequently used for phase reconstruction.

demaicing algorithms. For example, the authors implemented a variation of the “high-quality linear” algorithm to preserve the resolution of the analog-to-digital converter [185]. Further, as interpolation is used during demosaicing, color SLIM instruments require a factor of $\sqrt{2}$ denser sampling at the image plane compared to their gray-scale counterparts.

3.2f. SLIM and Other QPI Methods

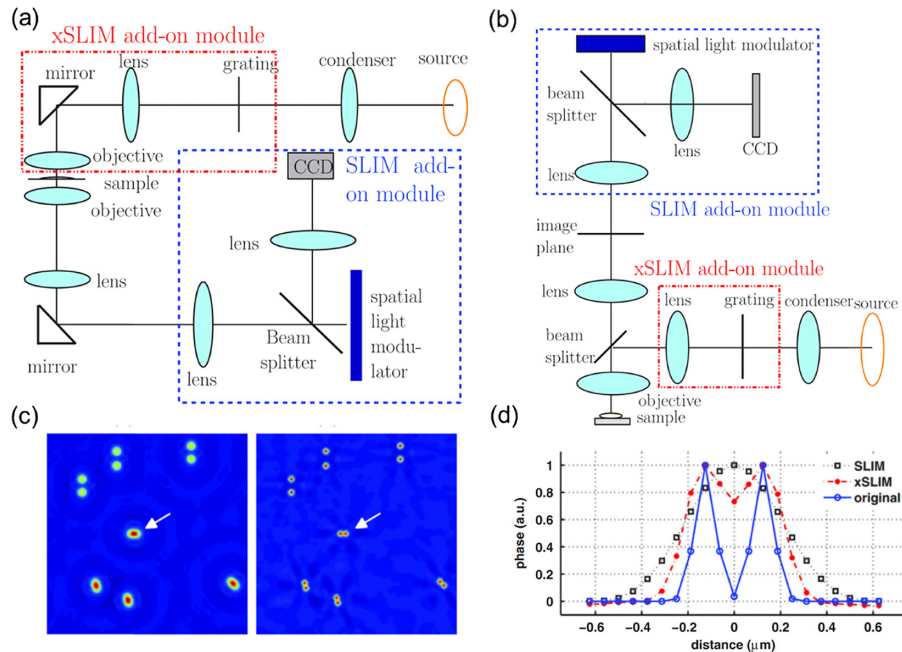
This subsection serves as a brief comparison of other QPI methods with SLIM, based on several key figures of merit: time-bandwidth product, space-bandwidth product, temporal phase sensitivity, and spatial phase sensitivity. The QPI methods include off-axis, phase-shifting, common-path, and white light [186–189]. Note that some methods can be characterized by more than one configuration. For example, SLIM is simultaneously a phase-shifting, common-path, and white-light method.

Table 2. QPI Methods and Their Figures of Merit^a

	Time-Bandwidth Product	Space-Bandwidth Product	Temporal Phase Sensitivity	Spatial Phase Sensitivity
Off-axis	✓			
Phase-shifting		✓		
Common path			✓	
White-light				✓

^aSLIM occupies the regions highlighted in green.

Figure 18



Proposed setups for xSLIM where the grating is relayed to the sample plane through a 4F system. The dashed box indicates the add-on module for SLIM. The dashed-dotted box indicates the add-on module for xSLIM. (a) Transmission mode. (b) Reflection mode. (c) Simulated images of randomly positioned bead pairs by SLIM and xSLIM. The two beads denoted by white arrows are 0.5 μm apart. (d) Cross sections of the images of these two beads by SLIM, xSLIM, and the original sample. Reprinted with permission from [49]. Copyright 2012 Optical Society of America.

Since they use spatial modulation to extract the phase image, *off-axis* methods provide better time-bandwidth products. Examples of such methods include digital holographic microscopy and Hilbert phase microscopy ([15], Chapter 9). Conversely, phase-shifting methods give better space-bandwidth products. Digitally recorded interference microscopy with automatic phase shifting, optical quadrature microscopy, and, of course, SLIM are examples of phase-shifting methods ([15], Chapter 10). Common-path interferometric geometries allow for high temporal phase sensitivity. Examples of such techniques include Fourier phase microscopy, diffraction phase microscopy, and SLIM (see [15], Chapter 11). Finally, white-light methods have the capability to average out the speckles inherent to coherent light imaging and, thus, achieve high spatial phase sensitivity. Examples of white-light methods include the transport of intensity equation, white-light diffraction phase microscopy, and SLIM (see [15], Chapter 12). Table 2 presents these four fundamental approaches and their performance.

Super-resolution SLIM is possible with structured illumination [49]. The proposed setups and the simulated results are illustrated in Fig. 18. More importantly, white-light illumination eliminates the speckles and spurious coherence noise. Compared to off-axis methods, SLIM has better performance in lateral resolution, temporal sensitivity, and phase sensitivity [46]. However, off-axis methods are faster, as they are single-shot.

3.3. Diffraction Tomography using SLIM

3.3a. White-Light Diffraction Tomography

White-light tomography extends the theory of diffraction tomography to white-light illumination [141]. Using SLIM images, the scattering potential is solved by deconvolving with the impulse response for white light under Born approximation. The axial dimension of the object is reconstructed by scanning the focus through the object. This method is capable of rendering 3D tomograms for unlabeled live cells with 350 nm transverse and 950 nm axial resolution.

The scattered field for the incident plane wave, $U_i = A(\omega)e^{i\beta(\omega)z}$, under Born approximation, can be calculated as [Fig. 19(a)]

$$U_s(\mathbf{k}_\perp, z; \omega) = -\frac{\beta_0^2(\omega)A(\omega)e^{i\gamma z}}{2\gamma} \chi[\mathbf{k}_\perp, \gamma - \beta(\omega)] \quad (48)$$

(see derivations in Section 2.1). The scattering potential can be reconstructed with the knowledge of the coherent transfer function (CTF) and the correlation function between the incident and scattered field $\Gamma_{is}(\mathbf{r}_\perp, z; \tau) = \langle U_i^*(z, t + \tau)U_s(\mathbf{r}_\perp, z; t) \rangle$ as

$$\chi(\mathbf{k}) = \frac{\Gamma_{is}(\mathbf{k}; 0)}{\Sigma(\mathbf{k})}, \quad (49)$$

where the CTF $\Sigma(\mathbf{k})$ can be calculated as

$$\Sigma(\mathbf{k}) = \frac{1}{8\bar{n}^2} \frac{(Q^2 + k_\perp^2)^2}{Q^3} S\left(-\frac{Q^2 + k_\perp^2}{2Q}\right), \quad (50)$$

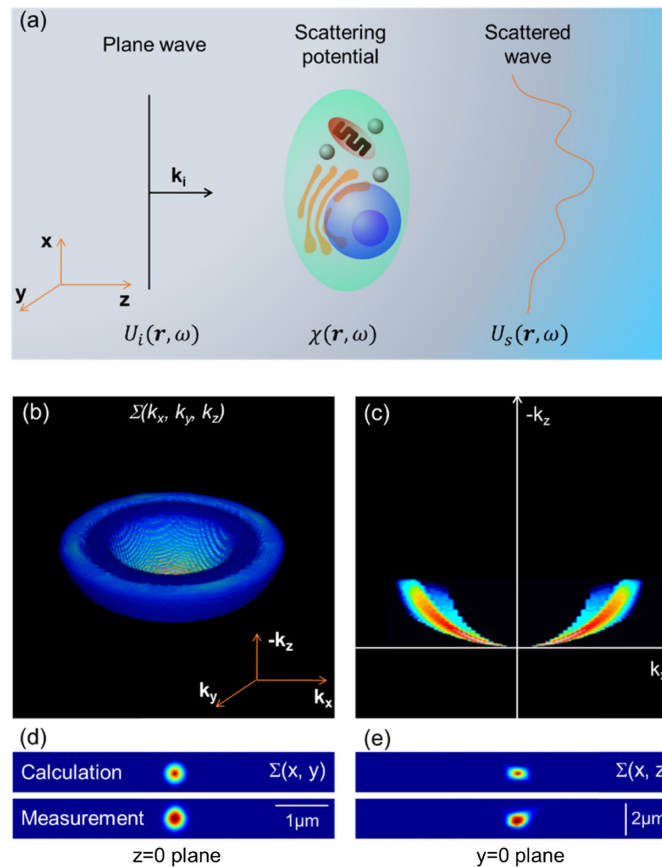
where S is the spectral density and $Q = \sqrt{\beta^2 - \mathbf{k}_\perp^2} - \beta$. The Fourier transform of the CTF gives the point spread function (PSF). We can see from this relation that broader spectral density and higher numerical aperture (NA) will give a narrower PSF. Figures 19(b) and 19(c) illustrate the transfer function $\Sigma(\mathbf{k})$ for the system. It can be seen that the width of k_z coverage increases with larger k_x , meaning that the

sectioning is stronger for finer structures. The transverse and longitudinal cross sections of the calculated and measured $\Sigma(x, y, z)$ are shown in Figs. 19(d) and 19(e). The structure of the object is finally recovered via a sparse deconvolution algorithm. Figure 20 presents the WDT of HT 29 cells.

3.3b. Wolf Phase Tomography

Wolf phase tomography (WPT) [103] is a fast 3D RI reconstruction method, based on the Wolf equations for propagating correlations of partially coherent light. This approach involves minimal computational steps, and renders high-resolution RI tomograms, without time-consuming deconvolution operations. WPT decouples the refractive-index distribution from the thickness of the sample directly in the space-time domain, without the need for Fourier transformation. From three independent intensity measurements corresponding to each phase shift in SLIM, the RI distribution is reconstructed right away from the Laplacian and second time derivative of the complex correlation functions. WPT is capable of extracting intrinsic refractive-index changes in live cells with a sensitivity on the order of 10^{-5} . The 3D RI can be reconstructed by

Figure 19



Scattering problem. (a) Illustration of light scattering under the first-order Born approximation where a plane wave's wavefront is perturbed by the object. (b) Three-dimensional rendering of the instrument transfer function, using the proposed WDT calculation. (c) Cross section of the transfer function at the $k_y = 0$ plane. (d) Calculated and measured PSF at the $z = 0$ plane. (e) Calculated and measured PSF in the $y = 0$ plane. Reprinted by permission from Macmillan Publishers Ltd.: Kim *et al.*, Nat. Photonics **8**, 256–263 (2014) [141]. Copyright 2014.

$$n(\mathbf{r}) = \sqrt{\frac{m(\mathbf{r}) - n_0^2 [1 - g(\mathbf{r})]}{1 + g(\mathbf{r})}}, \quad (51)$$

where the functions m and g are defined as

$$m(\mathbf{r}) = \frac{c^2 (\nabla^2 \Re[\Gamma_{is}(\mathbf{r}, \mathbf{r}, \tau)] + \zeta(\mathbf{r}))}{\frac{\partial^2 \Re[\Gamma_{is}(\mathbf{r}, \mathbf{r}, \tau)]}{\partial \tau^2}} \Bigg|_{\tau = -\pi/\langle \omega \rangle}, \quad (52)$$

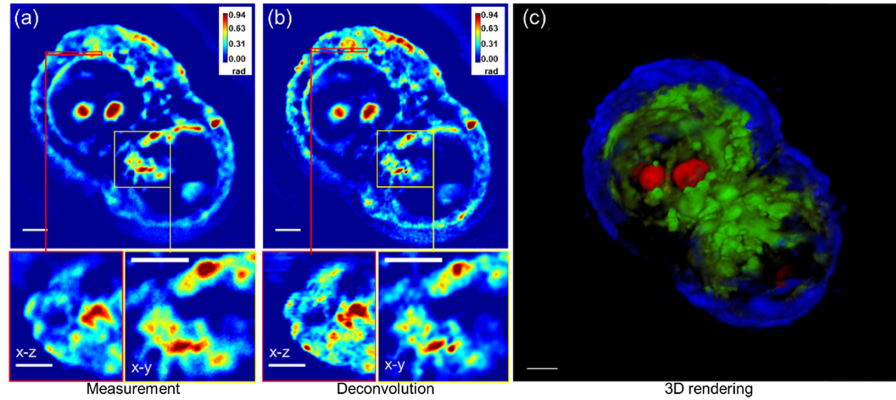
$$\zeta(\mathbf{r}) = -2\Re \int_0^\infty \langle \nabla U_i^*(\mathbf{r}, \omega) \cdot \nabla U_s(\mathbf{r}, \omega) \rangle e^{i\omega\pi/\langle \omega \rangle} d\omega, \quad (53)$$

$$g(\mathbf{r}) = \frac{\frac{\partial^2 \Re[\Gamma_{ii}(\mathbf{r}, \mathbf{r}, \tau)]}{\partial \tau^2}}{\frac{\partial^2 \Re[\Gamma_{is}(\mathbf{r}, \mathbf{r}, \tau)]}{\partial \tau^2}} \Bigg|_{\tau = -\pi/\langle \omega \rangle}, \quad (54)$$

where c is the speed of light in vacuum, and n_0 is the refractive index of the background. The correlation functions are defined as $\Gamma_{pq}(\mathbf{r}_1, \mathbf{r}_2, \tau) = \langle U_p^*(\mathbf{r}_1, t) U_q(\mathbf{r}_2, t + \tau) \rangle_t$, $p, q = \{i, s\}$. \Re denotes the real part. Γ_{is} is the correlation function between the incident and scattered fields, and Γ_{ii} is the autocorrelation function of the incident fields. The term in Eq. (53) does not substantially contribute to the final RI and can be omitted for faster construction.

The normalized spectrum of the halogen source measured by the spectrometer (Ocean Optics) is shown in Fig. 21(a). The real part of the normalized autocorrelation Γ_{ii} is obtained by taking the Fourier transform of the spectrum. The second-order time

Figure 20



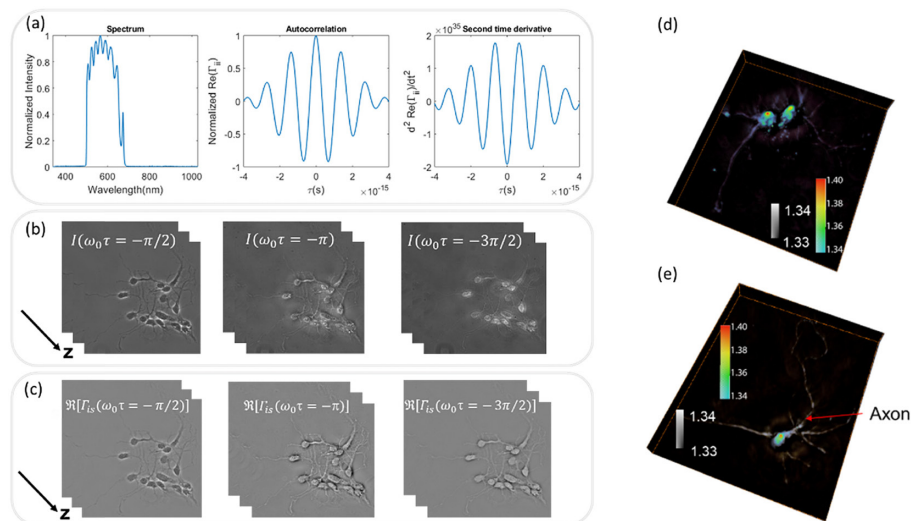
WDT of HT29 cells. (a) Measured z -slice (top), cross section at the area indicated by the red box (bottom left) and a zoomed-in image of the area indicated by the yellow box (bottom right), measured using a $\times 63/1.4$ NA oil immersion objective. (b) Deconvolved z -slice corresponding to the measurement shown in (a) (top), cross section at the area indicated by the red box (bottom left) and a zoomed-in image of the area indicated by the yellow box (bottom right). By comparing (a) and (b), the resolution increase can be clearly seen. (c) False-color three-dimensional rendering of the deconvolution result. We used z -stacks of 140 images, each with dimensions of 640×640 . Owing to the large image dimensions, the image is split into 25 sub-images for faster deconvolution. Overall, the deconvolution process took approximately 1 h. Scale bars in all panels, $5 \mu\text{m}$. Reprinted by permission from Macmillan Publishers Ltd.: Kim *et al.*, Nat. Photonics **8**, 256–263 (2014) [141]. Copyright 2014.

derivative of Γ_{ii} is depicted in Fig. 21(a). The real part of Γ_{is} can be solved from SLIM images [see Figs. 21(b) and 12(c)]. The Laplacian in Eq. (52) is calculated using three images of $\Re[\Gamma_{is}]$ [shown in Fig. 21(c)] with the first-order finite difference approximation. The z component of the Laplacian was computed using three axially distributed frames, separated by a distance that matches the $x - y$ pixel sampling and is much smaller than the diffraction spot. The second-order derivatives in Eqs. (52) and (54) are calculated in MATLAB, using three phase-shifted frames. The WPT algorithm requires 40 ms to reconstruct the refractive-index map at one z position, with a 3-megapixel field of view.

The 3D RI tomography of neurons is presented in Figs. 21(d) and 21(e). The 3D rendering of a bovine sperm cell is displayed in Fig. 22(a). In the sperm head, the acrosome and the nucleus can be identified with RI values between 1.35 and 1.37. The centriole and mitochondria-rich midpiece of the sperm cell yield high refractive-index values [Fig. 22(b)]. The tail of the sperm has an RI value of 1.35, and the axial filament inside the tail with a slightly higher RI value of 1.36 can be recognized. The end piece of the sperm has the lowest RI value of approximately 1.34.

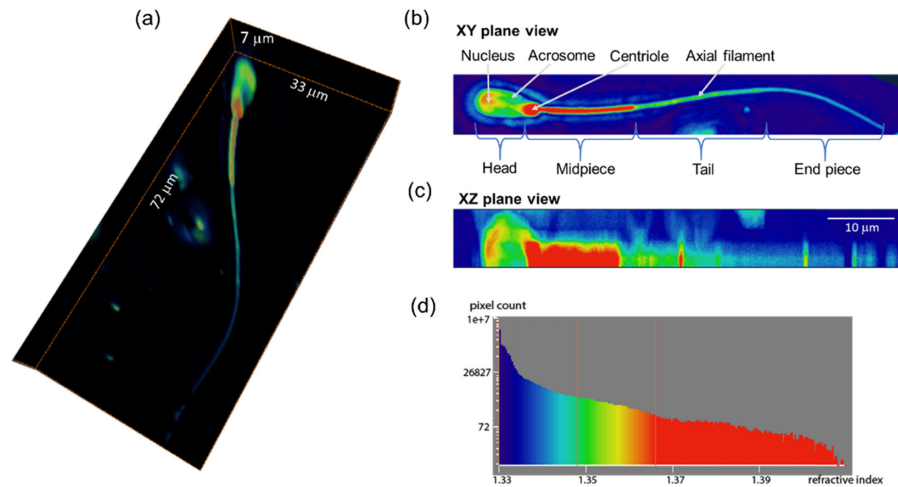
Due to the high throughput, low phototoxicity, absence of photobleaching, and easy sample preparation, WPT is capable of studying real-time volumetric biological events in living cells. We imaged the growth and proliferation of hippocampal neurons over the course of several days, in six-well plates. The RI distribution of the whole well of neurons is displayed in Fig. 23(a). One tile zoom in of the whole well and its distribution of RI are shown in Fig. 23(b). Figure 23(c) describes the average of the RI within this tile versus time. Figure 23(d) shows that the variance of the RI for this tile increases with time as well.

Figure 21



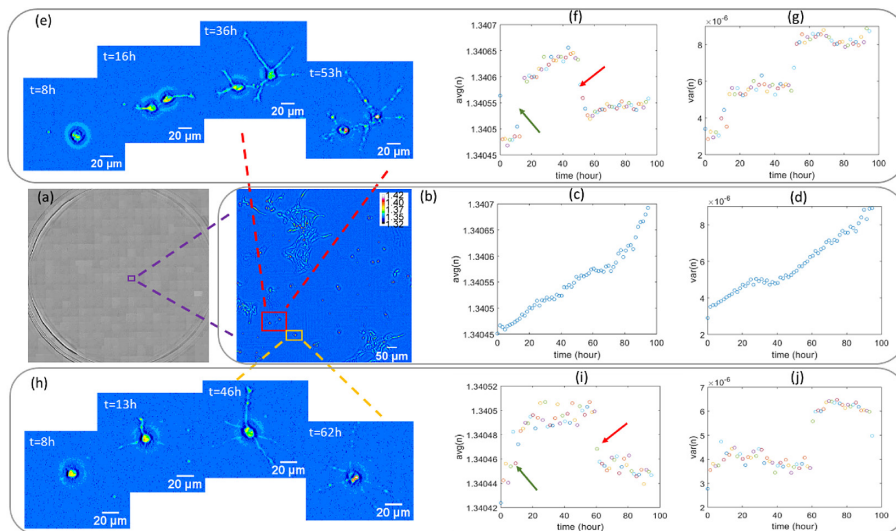
Working principle of WPT. (a) Spectrum, autocorrelation, and second-order derivative of the autocorrelation of the halogen source measured by the spectrometer. (b) Three phase-shifted frames of hippocampal neurons ($40\times/0.75\text{NA}$ objective). (c) Real part of the correlation function at three different time-lags. (d), (e) 3D rendering of RI tomograms of the hippocampal neurons. Two colormaps as indicated are used to enhance the dendrites and axons. The axon is pointed with a red arrow. Reprinted by permission from Macmillan Publishers Ltd.: Chen *et al.*, Light Sci. Appl. 9, 142 (2020) [103]. Copyright 2020.

Figure 22



WPT of sperm cells. (a) 3D RI tomogram of a spermatozoon ($40\times/0.75\text{NA}$ objective). (b) XY plane projection view. The nucleus, acrosome, centriole, and axial filament of the sperm cell are pointed by the white arrows. (c) XZ plane projection view. (d) Histogram of the RI of the sperm cell. Reprinted by permission from Macmillan Publishers Ltd.: Chen *et al.*, *Light Sci. Appl.* **9**, 142 (2020) [103]. Copyright 2020.

Figure 23



Dynamic WPT of live cells across multiwell plates. (a) RI map across a whole well of living hippocampal neurons ($10\times/0.3\text{NA}$ objective) composed of 20×21 mosaic tiles, each of $214\ \mu\text{m}\times 204\ \mu\text{m}$ area. (b) Zoomed-in RI map of the purple box in (a) with (c) average and (d) variance of the RI versus time. (e) Zoomed-in RI map of the red box in (b) with (f) average and (g) variance of the RI. The green arrow indicates the increase of the RI when the two neurons separated and their dendrites appeared; the red arrow shows the decrease in RI when the two neurons died. (h) Zoomed-in RI map of the yellow box in (b) with (i) average and (j) variance of the RI. The green arrow indicates the jump of the RI when the dendrites appeared; the red arrow shows the decrease in RI when the neuron died. Reprinted by permission from Macmillan Publishers Ltd.: Chen *et al.*, *Light Sci. Appl.* **9**, 142 (2020) [103]. Copyright 2020.

Figure 23(e) shows a zoomed-in image of the red box in Fig. 23(b) containing two neurons. The neurons spread out into two regions at around $t = 16$ h, kept growing until around $t = 53$ h, and then died. We can see that both the average and variance of the RI show three different stages [Figs. 23(f) and 23(g)]. One significant change in the average and variance of the RI appeared when the two neurons were separated (red arrows). Another change was visible when the two neurons died (green arrows). The death event was accompanied by a decrease in the mean RI, likely due to the membrane permeability, which allowed for water influx. Figure 23(h) shows a zoomed-in image of the yellow box in Fig. 23(b) containing one neuron. The neuron dendrites started to appear at approximately the $t = 13$ h time point, resulting in a jump in the average RI [Fig. 23(i)]. The neuron kept growing until approximately $t = 62$ h and then died, leading to a decrease in the average RI. Some oscillations in the variance [Fig. 23(j)] of the RI appeared before the neuron died, while exhibiting a clear change after the neuron died.

4. SLIM APPLICATIONS

4.1. Basic Science Applications

4.1a. Cell Dynamics

SLIM is an ideal candidate to study cellular dynamics for a long period ranging from seconds to days because of its extremely low spatial noise (0.3 nm) and temporal stability (0.03 nm) [45]. As an early example, the dynamics of mixed glial–microglial cell culture are presented in Fig. 24 based on 397 SLIM images over 13 min. The comparison of phase-contrast and SLIM images is presented in Fig. 24(b). We can see that the cell is bigger in the phase-contrast image due to the halo around the edge of the cell. Figure 24(c) shows the path-length changes due to both membrane displacements and local refractive-index changes caused by cytoskeleton dynamics and particle transport at two arbitrary points on the cell. It reveals an interesting, periodic behavior. Moreover, the rhythmic motions have different periods at two locations inside of the cell, which may indicate different rates of metabolic or phagocytic activity. The probability distribution of path-length displacements between two successive frames was retrieved with a dynamic range of more than five orders of magnitude [Fig. 24(d)]. This distribution can be fitted very well with a Gaussian function up to path-length displacements $\Delta s = 10$ nm, at which point the curve crosses over to exponential decay. The normal distribution suggests that these fluctuations are the result of numerous uncorrelated processes governed by equilibrium. On the other hand, exponential distributions indicate the deterministic motions, mediated by metabolic activity.

As another example of cellular dynamics, SLIM can be used to examine the diameter and axonal mass transport of the neurons [190]. The reconstructed SLIM image of an axon is shown in Fig. 25(a). The average diameter and average phase of axons treated with different drugs are monitored in Figs. 25(b) and 25(c) over time. Disrupting actin filaments resulted in an increase [Fig. 25(b), red] in average diameter while disrupting microtubules [Fig. 25(b), blue] led to a decrease in average diameter after 60 min of drug treatment. SLIM images revealed that the average phase increased when actin was disrupted [Fig. 25(c), red]. The average phase remained unchanged upon microtubule disruption [Fig. 25(c), blue] or Y-27632 treatment [Fig. 25(c), cyan].

4.1b. Cell Growth

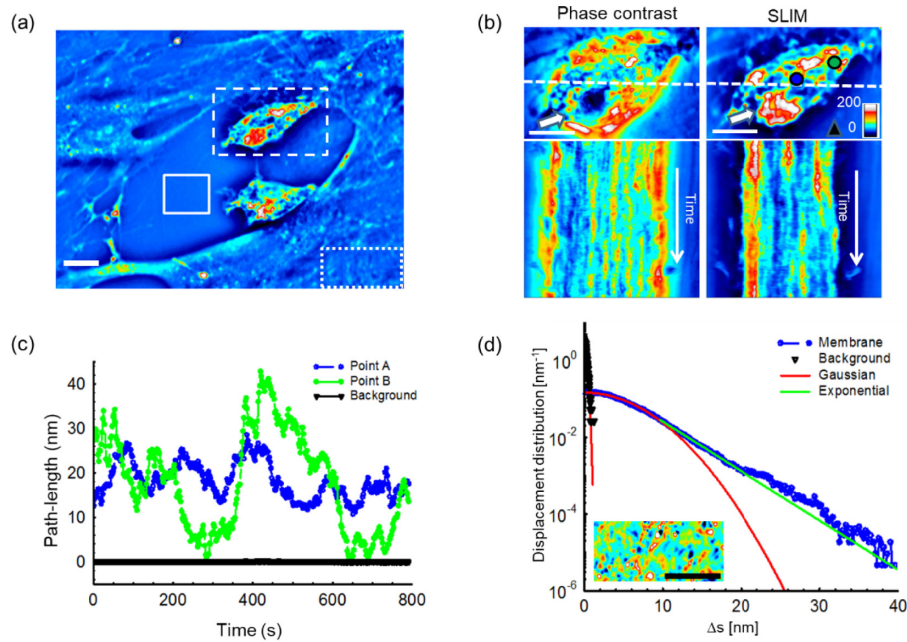
The age-long debate about cell growth is whether the growth rate is constant (linear growth) or is proportional to the cell mass (exponential growth). Each growth pattern conveys its own biological significance. To distinguish these two patterns, a resolution of $< 6\%$ in cell size is required [191]. SLIM can accomplish this task with

spatial and temporal sensitivities of 1.5 and 0.15 fg/ μm^2 , respectively. SLIM has been serving as an imaging tool to study cell-growth-related problems [43,192].

The phase in SLIM images represents the integral of the refractive-index difference between the object and the medium and the thickness of the object, i.e., $\phi = \int (n - n_0)dt$. The concept of dry mass was proposed to quantify the dry weight of protein in cells without the need for measuring the refractive index and thickness. The relationship between the phase in SLIM images and dry mass is as follows [193–195]:

$$M(x, y) = \frac{\lambda}{2\pi\gamma} \phi(x, y), \quad (55)$$

Figure 24



SLIM dynamic imaging of mixed glial–microglial cell culture. (a) Phase map of two microglia cells active in a primary glial cell culture. The solid line box indicates the background used in (d), the dashed line box delineates a reactive microglial cell used in (b), and the dotted line box indicates the glial cell membrane used in (d). (b) Phase-contrast image and SLIM image of the cell shown in (a). Pseudocoloration is for light intensity signal and has no quantitative meaning for phase contrast. Registered time-lapse projection of the corresponding cross section through the cell as indicated by the dashed line in (b). The arrows in (b) point to the nucleus, which is incorrectly displayed by PC as a region of low signal. (c) Path-length fluctuations of the points on the cell [indicated in (b)] showing intracellular motions (blue- and green-filled circles). Background fluctuations (black) are negligible compared to the active signals of the microglia. (d) Semi-logarithmic plot of the optical path-length displacement distribution associated with the glial cell membrane indicated by the dotted box in (a). The solid lines show fits with a Gaussian and exponential decay, as indicated in the legend. The distribution crosses over from a Gaussian to an exponential behavior at approximately 10 nm. The background path-length distribution, measured from the solid line box, has a negligible effect on the signals from cells and is fitted very well by a Gaussian function. The inset shows an instantaneous path-length displacement map associated with the membrane. Scale bars, 10 μm . Reprinted with permission from [111]. Copyright 2011 Optical Society of America.

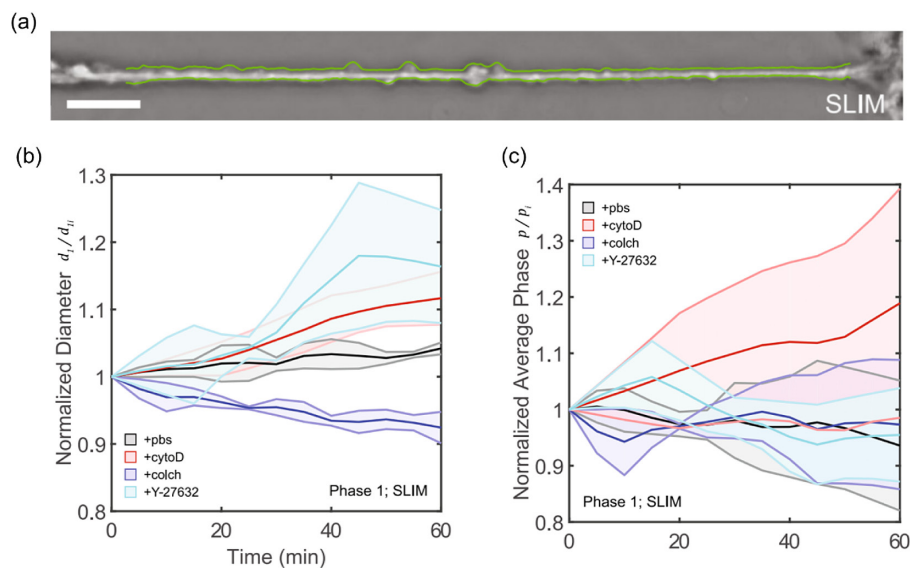
where λ is the center wavelength; γ is the refractive increment, which lies within the range of 0.18–0.21 ml/g for most biological samples; and $\phi(x, y)$ is the measured phase.

As an example, SLIM can quantify the cell-to-cell lipid-content heterogeneity of *Yarrowia lipolytica* cells in both volume and dry-mass ratios (Fig. 26) [44]. The SLIM phase image is presented in Fig. 26(a) with arrows pointing at cytosolic lipid droplets (LD). To calculate the dry mass of lipid droplets (LD) that are loaded with triacylglycerol (TAG) at a negligible protein content, the number-density of TAG molecules was determined by the Clausius–Mossotti equation. This was confirmed by characterizing the cytosolic and LD elemental composition with nanoscale secondary ion mass Spectrometry (NanoSIMS) [196]. The cytosol is uniformly composed of naturally abundant nitrogen (^{14}N), as illustrated in Fig. 26(c). LDs, which were co-localized by transmission electron microscopy (TEM) via osmium staining and NanoSIMS, were found to be composed primarily of ^{13}C and a comparable ^{14}N content to the extracellular background [Fig. 26(d)].

As an example, Fig. 27 presents the dry-mass growth curves for *E. coli* cells using SLIM [47]. The dry-mass noise is characterized from a region without any cells and having the same area as the average cell size, with a STD of the dry mass of 2.97 fg. Background fluctuations are negligible, compared to the average cell dry mass (0.2655 pg).

As another example of cell proliferation, we performed long imaging of cell growth to estimate the “influence” of cellular clusters on their neighbors [197]. We analyzed

Figure 25



(a) Reconstructed SLIM image of a cleaned axon. Green lines labeled the boundaries determined by the analysis algorithm. Scale bar at 10 μm . (b) SLIM measurements of average diameter over time of axons treated with PBS (gray), cytoD (red), noco/colch (blue), and Y-27632 (cyan). (c) Average phase measured by SLIM of axons treated with PBS (gray), cytoD (red), colch (blue), and Y-27632 (cyan). The average density of the cytoplasm and the cytoskeletal components increases with time with the disruption of actin, but not with microtubules. All shaded regions indicate error bars in the standard deviation. Unpaired two-sample t -test used to obtain p -values. Reprinted by permission from Macmillan Publishers Ltd.: Fan *et al.*, *Sci. Rep.* 7, 14188 (2017) [190]. Copyright 2017.

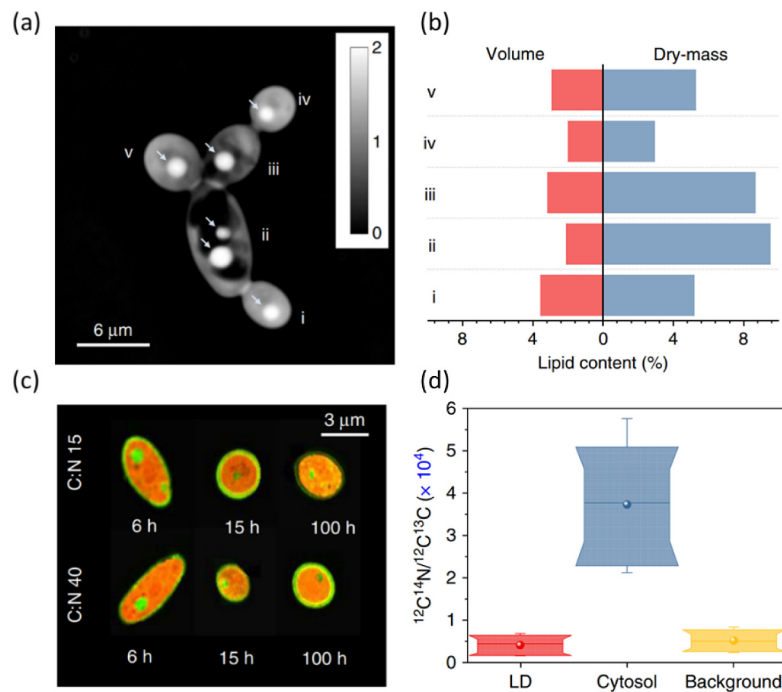
epithelial and fibroblast cultures imaged over several days. Figure 28 shows cell growth and division based on SLIM images. We can see that the time-lapse images of cells resemble “genealogical” trees, with cells splitting into branches after each division.

We can define a growth rate as the dry-mass doubling time, b , from the fit of the exponential equation $M(t)/M(0) = 2^{bt}$. The covariance between distance and growth rate is $\text{cov}(r, b^{-1})$, such that the Pearson correlation coefficient between growth and distance is

$$\rho = \frac{\text{cov}(r, b^{-1})}{\sqrt{\sigma_r \sigma_{b^{-1}}}}, \quad (56)$$

where σ_r and $\sigma_{b^{-1}}$ are the variances of the variables r and b^{-1} . The distributions of the correlation coefficients for clusters of fibroblasts (NIH/3T3, ATCC CRL-1658) and epithelial (HeLa, ATCC CCL-2) cells are presented in Figs. 29(b) and 29(d). We can see that there is a significant number of cells characterized by a medium correlation between their growth rate and distance (modulus of the Pearson coefficient between

Figure 26



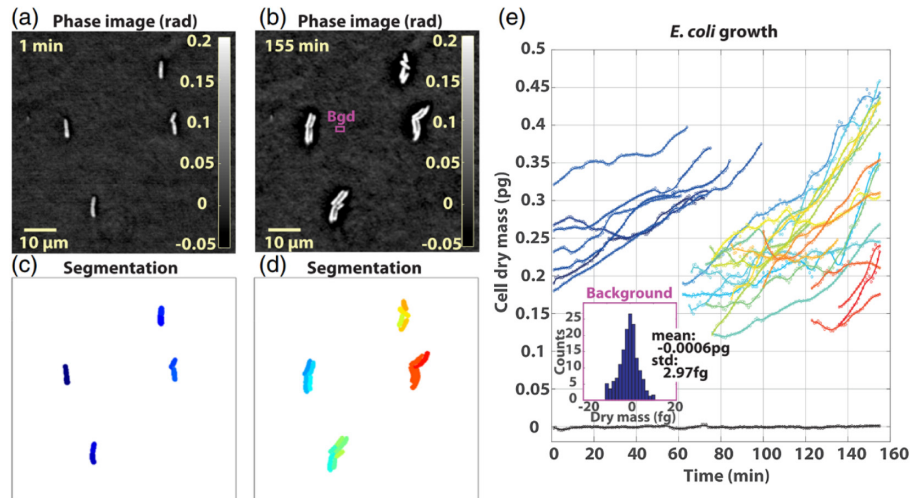
(a) Optical-phase image of individual *Y. lipolytica* cells labeled from (i) to (iv); arrows indicate the cytosolic LDs, and scale bar is displayed in micrometers. (b) Histogram of the lipid-content in percentage volume ($V_{\text{TAG}}/V_{\text{biomass}}$) and dry-mass ($DM_{\text{TAG}}/DM_{\text{biomass}}$) ratios for the cells shown in (a); importantly, the single-cell volumetric lipid content is seen to scale inversely with the DM lipid content specifically for cells (i), (ii), and (iii). (c) Elemental composition of *Y. lipolytica*: NanoSIMS images of the MTYL038 strain at two C/N growth conditions for 6, 15, and 100 h; the cytosolic pools of naturally abundant ^{14}N and the LD content of ^{13}C are highlighted in red and green, respectively. (d) Box plots of $^{12}\text{C}^{14}\text{N}/^{12}\text{C}^{13}\text{C}$ ratio of the cytosolic LD droplets (red), the cytosol excluding the LDs (blue), and the extracellular background (yellow) for 40 individual single-cell and single-LD observations, for cells sampled at C/N:15 and C/N:40 at 6, 15, and 100 h. Reprinted by permission from Macmillan Publishers Ltd.: Vasdekis *et al.*, Nat. Commun. **10**, 848 (2019) [44]. Copyright 2019.

0.25 and 0.5). A small percentage of cells exhibit strong correlations, which we label as “influencer” cellular clusters.

4.1c. Cell Migration

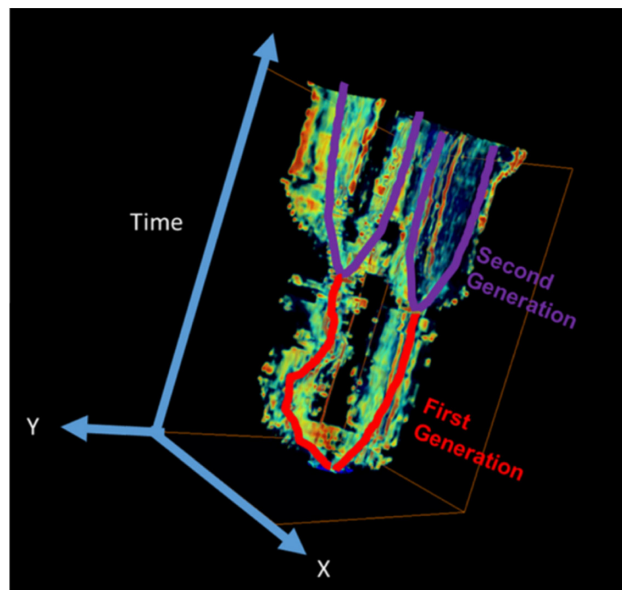
Cell growth and motility are both crucial parts for understanding a proliferating cellular system. To study cell motility, we used SLIM to track single cells [198]. The

Figure 27



SLIM measurement of *E. coli* growth. (a) and (b) SLIM phase images at time $t = 0$ h and 2 h 35 min, respectively. (c),(d) Corresponding segmented images. (e) Dry mass versus time for the segmented cells in (c),(d). Inset: histogram of the dry-mass fluctuations associated with a background region having the same area as the average cell size and highlighted in (b). Reprinted with permission from Coquoz *et al.*, *J. Biomed. Opt.* **21**, 126019 (2016) [47].

Figure 28



Cell growth resembles a genealogical tree when time is taken as the third dimension, with two daughter cells after the first division (red) and four daughter cells (purple) after the second division. Reprinted with permission from Kandel *et al.*, *Biomed. Opt. Express* **10**, 4664–4675 (2019) [197].

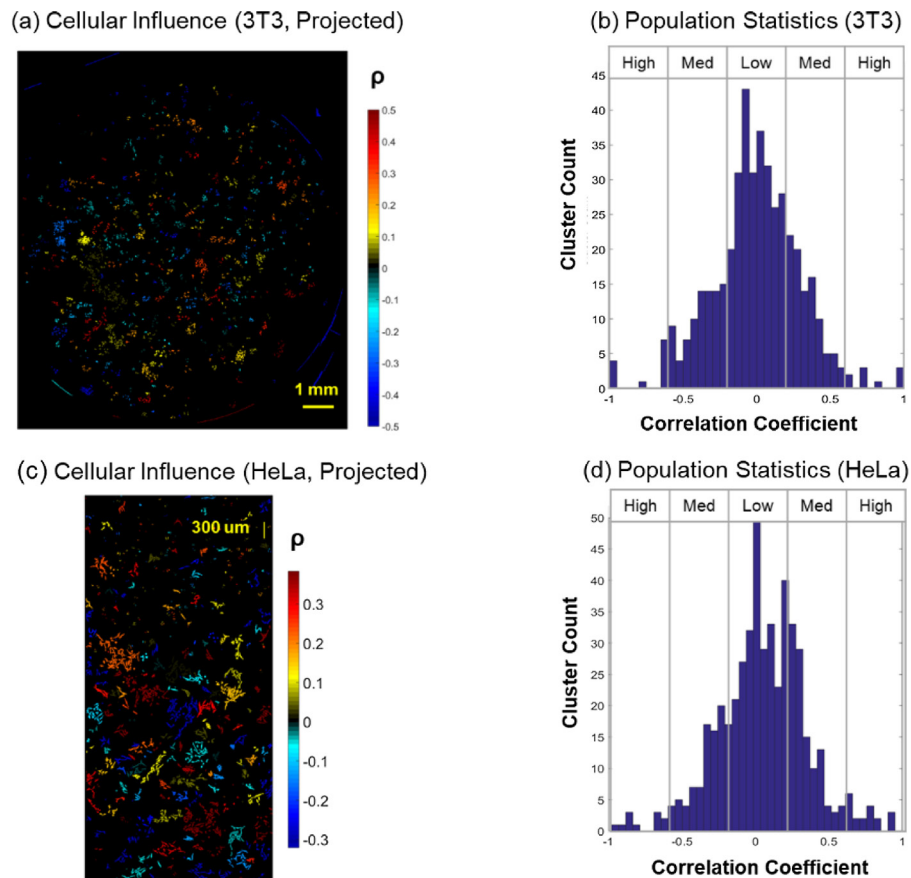
trajectories of the attached (red) and motile cells (black) are shown in Fig. 30(a). Clearly, the cell associated with the red trace is attached to the glass surface, as the motion exhibits very limited motion. The dry-mass analysis for the attached and motile cells is illustrated in Fig. 30(b). We can see that cells with lower mean square displacements (MSDs) ($<10 \mu\text{m}^2$) present low or negative dry-mass growth. The MSDs for these two cells are depicted in Fig. 30(c). Figure 31(a) shows that the MSD increases by four orders of magnitude between the first and fourth generations. Figure 31(b) compares the maximum MSD for each cell with its fitted linear growth rate, indicating that the MSD and growth rate are related exponentially.

4.1d. Intracellular Transport

Dispersion relation phase spectroscopy (DPS) is a technique to characterize mass transport using SLIM [177,199]. It starts with the assumption that the dry-mass density satisfies the diffusion-advection equation, namely,

$$\left(-Dq^2 + i\mathbf{q} \cdot \mathbf{v} - \frac{\partial}{\partial t}\right) \eta(\mathbf{q}, t) = 0, \quad (57)$$

Figure 29

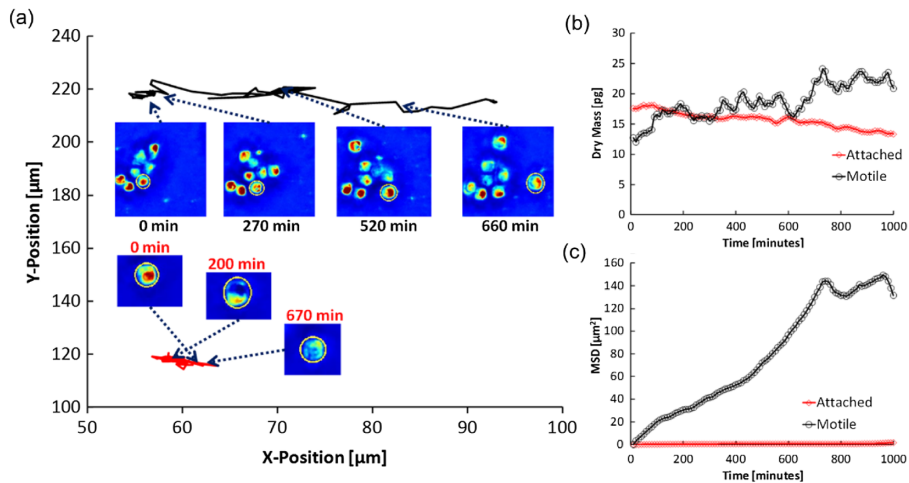


Projection of cellular influence. (a) Correlation coefficients for the 3T3 culture are projected onto the segmentation map at the end of the experiment. This gives a spatial distribution of correlation coefficients. (b) Histogram of the correlation coefficient for all 3T3 clusters. (c) Correlation coefficients for the HeLa culture are projected onto the segmentation map at the end of the experiment. (d) Histogram of the correlation coefficient for all HeLa clusters. Reprinted with permission from Kandel *et al.*, *Biomed. Opt. Express* **10**, 4664–4675 (2019) [197].

where D is the diffusion coefficient, \mathbf{v} is the velocity of the advection motion, and \mathbf{q} is the spatial frequency, the Fourier conjugate to the 3D spatial coordinate. Under the assumption that the advection velocity distribution is Lorentzian with width Δv and mean advection velocity v_0 , the spatial Fourier transform of the temporal autocorrelation of dry-mass density is in the form of

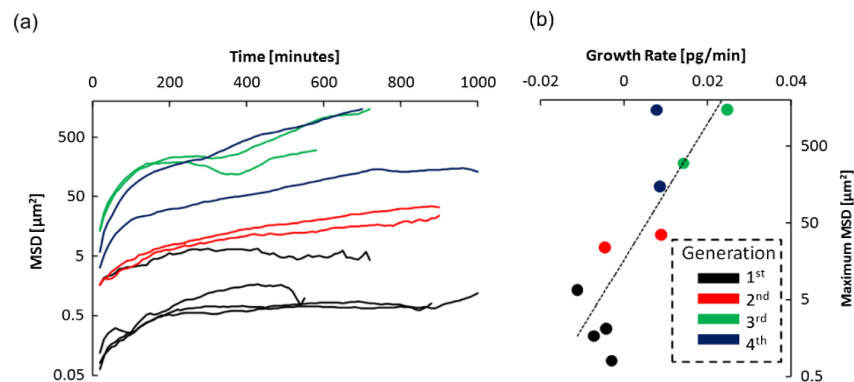
$$\langle g(\mathbf{q}, \tau) \rangle_v = \exp(iq v_0 \tau) \exp[-(Dq^2 + \Delta v q) \tau], \quad (58)$$

Figure 30



(a) Trajectories of attached (red line) and motile (black line) cells. Time-stamped insets show the tracked cell at various time points. The motile cell exhibits clear directional motion over time, whereas the adherent cell is jostling in place. (b) Dry-mass growth of the two cells shown in (a); the attached cell exhibits no growth, whereas the motile cell approximately doubles its mass. (c) MSD for the two cells shown in (b). Reprinted with permission from Sridharan *et al.*, Biomed. Opt. Express **2**, 2815–2820 (2011) [198].

Figure 31



(a) Semilogarithmic plot MSD versus time for all the individual cells tracked. It can be seen that the MSD increases by three to four orders of magnitude between the first and fourth generations (b) Semilogarithmic plot of the maximum MSD versus the approximated linear growth rate for each cell. Reprinted with permission from Sridharan *et al.*, Biomed. Opt. Express **2**, 2815–2820 (2011) [198].

where $\langle \rangle_v$ denotes the ensemble average over the velocity distribution. Therefore, the mean advection velocity produces a modulation frequency qv_0 to the temporal autocorrelation, whose envelope decays exponentially at a rate

$$\Delta\omega(q) = Dq^2 + \Delta vq. \quad (59)$$

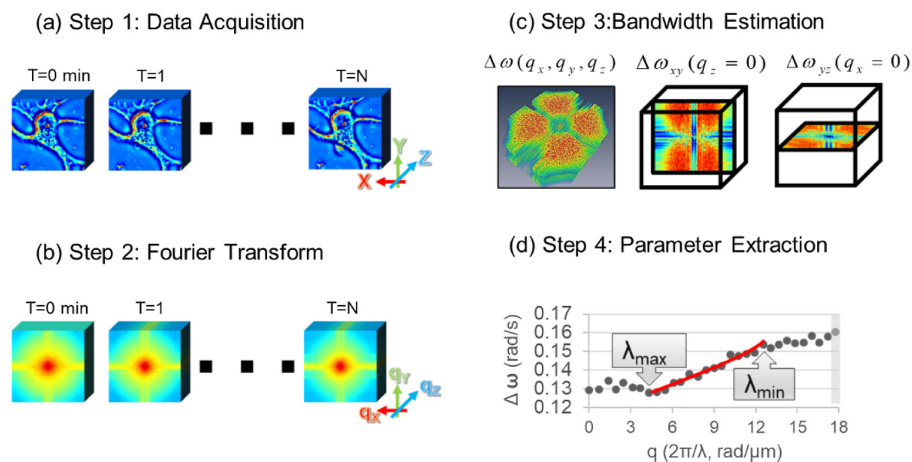
This relationship describes the dispersion relation associated with intracellular mass transport. The detailed steps are illustrated in Fig. 32. Through the time-lapse phase measurement (Fig. 32 Step 1) using SLIM, the Fourier transform of the temporal autocorrelation function (Fig. 32 Step 2) can render the decay rate $\Delta\omega(q)$ with the bandwidth estimation (Fig. 32 Step 3). The diffusion coefficient D and the velocity Δv are obtained by fitting the $\Delta\omega(q)$ function (Fig. 32 Step 4). Note that the diffusion coefficients and applicable spatial scales (λ_{\min} , λ_{\max}) are expected to vary between individual specimens, due to the diversity of transport phenomena in living cells.

As an example, we used the dispersion relation to study microtubule motility [200]. Figure 33 shows the DPS procedure for analyzing full-field, time-lapse SLIM images of microtubules. The value of Δv considerably decreases linearly in time after approximately 20 min, most likely due to ATP depletion. This result implied that the velocity distribution narrows; i.e., the probability of having high speeds decreases over time. This linear decrease with time reveals a deceleration in microtubule activity commensurate with a reduced availability of ATP.

4.1e. Applications in Neuroscience

The emergence of a neuronal network in a developing nervous system is a complicated process involving a multitude of chemical, mechanical, and electrical signals. Studying neuronal networks is essential to understanding brain connectivity and the mechanisms involved in central nervous system disease.

Figure 32



Dispersion relation calculated from the bandwidth of the Fourier transformed volumes. (a) The DPS transport assay consists of four steps. First, time-lapse tomograms are acquired, and the Fourier transform is taken of each volume. (b) To estimate the dispersion relation at each spatial mode, we perform a forward difference, which reduces the 3D data to a single cube. (c) This cube is then reduced to two lines by taking the radial average along the XY and YZ dimensions. (d) Yielding relations for horizontal and vertical motion. Kandel *et al.*, Cytometry Part A **91**, 519–526 (2017) [177]. Copyright Wiley-VCH Verlag GmbH & Co. KGaA. Reproduced with permission.

SLIM can measure several fundamental properties of neural networks from the sub-cellular to the cell population level [201]. For instance, SLIM can calculate the correlations between trends in the growth, transport, and spatial organization of neural networks [202]. It was found that cell density (confluence) significantly affects both the growth rate and mass transport [203].

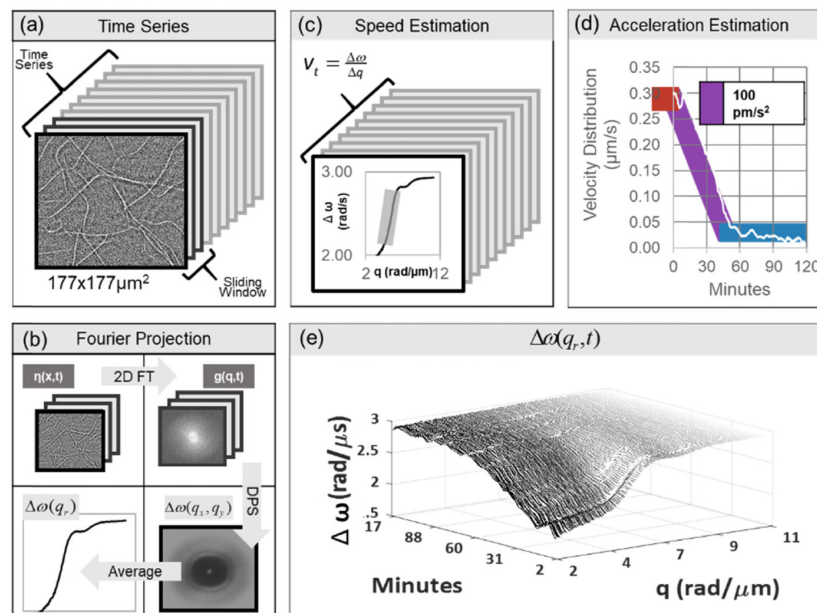
The topological properties of the neuronal culture networks were analyzed to elucidate how neurons connect through time-lapse imaging with SLIM [204]. Figures 34(a)–34(c) show the SLIM images for three different timeframes. The zoomed portions of the middle region of the neurons are presented in Figs. 34(d)–34(f). The reconstructed neuronal culture networks are depicted in Figs. 34(g)–34(i) with the tracing algorithm. Different colors represent the different identifications for each neuron and neurite. After constructing the adjacency matrices from the tracing and segmentation algorithm, the visualization of the network layouts is illustrated for different timeframes in Figs. 34(j)–34(l).

4.2. Clinical Applications

4.2a. Cancer Screening

The current practice of surgical pathology relies on external contrast agents to reveal tissue architecture, which is then qualitatively examined by a trained pathologist

Figure 33

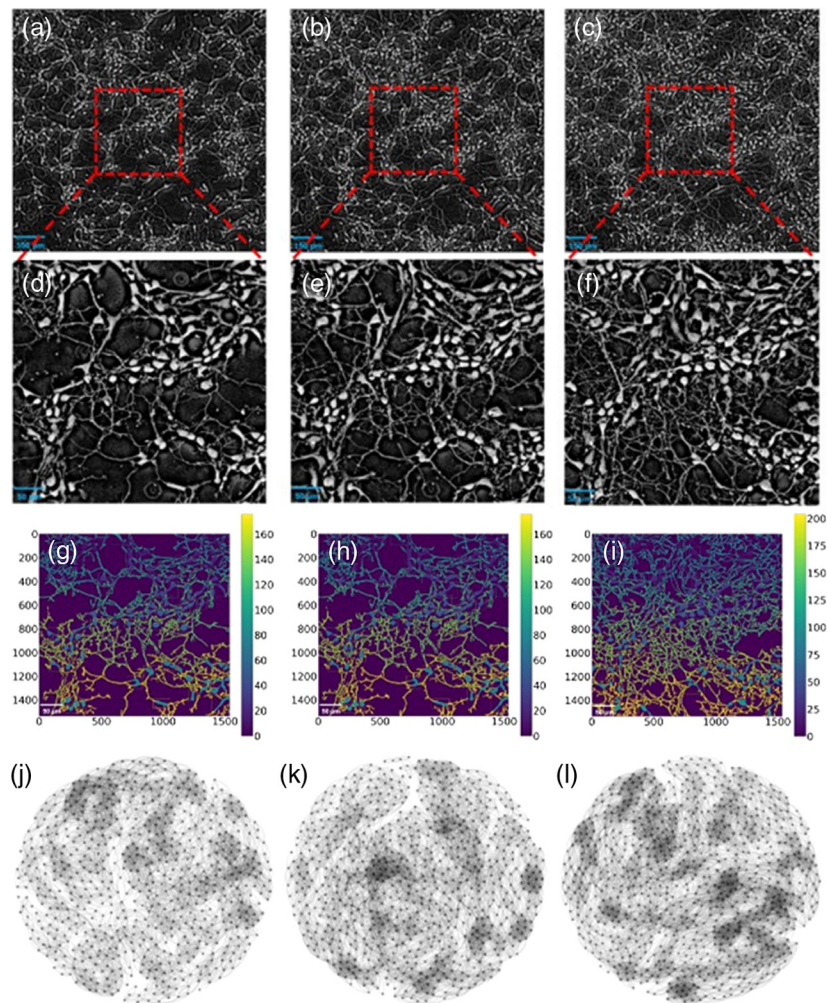


Long-term imaging reveals deceleration of microtubules. (a) Illustration of the time-resolved SLIM image stacks. (b) The dispersion relation is computed over a temporal window of 128 frames for each time point in the series. In short, the method involves taking the 2D Fourier transform of each image and computing the decay (or temporal bandwidth) at each spatial frequency. After the isotropic assumption, the volumetric data is reduced to a single dimension. When the window is advanced, one of the old Fourier transforms is discarded and the bandwidth is recomputed. (c) Microtubule gliding velocity standard deviation was calculated using DPS, on a rolling basis over approximately 15,000 frames, taken 0.475 s apart. (d) In this run, after 20 min, the spread of the velocity distribution begins to decrease, with virtually no significant motion after the 60 min mark. (e) DPS signals versus time shows continuous change in slope. Reprinted with permission from Kandel *et al.*, ACS Nano 11, 647–655 (2017) [200]. Copyright 2017 American Chemical Society.

[205]. The diagnosis is based on the comparison with standardized empirical, qualitative assessments. Moreover, the analysis of the stained tissue is affected by staining strength, color balance, and imaging conditions.

SLIM is a label-free approach to pathology with unstained biopsies, which provides quantitative OPD measurements that are sensitive to the nanoscale tissue architecture [206–208]. With our highly parallelized, dedicated software algorithms for data acquisition, SLIM allows us to image at a throughput comparable to that of commercial tissue scanners [169]. Based on the measured phase information, we implemented software tools for autofocusing during imaging, as well as image archiving and

Figure 34



Layouts for neuronal culture networks at three representative time points. (a)–(c) Neurons at the start of the experiment at (a) time $t = 0$ h and (b) $t = 7$ h; (c) neurons at the end of the experiment, $t = 14$ h. (d)–(f) Magnification zoom of the neurons at (d) $t = 0$ h, (e) $t = 7$ h, and (f) $t = 14$ h. (g)–(i) Identified neurons and their connections obtained with our algorithm (see Section 3 in [204]) for the three corresponding time points (each neuron and neurite is identified by a unique color). After constructing the adjacency matrices from the tracing and segmentation algorithm, the visualization of the network layouts at (j) $t = 0$ h, (k) 7 h, and (l) 14 h is presented. Reprinted by permission from Macmillan Publishers Ltd.: Yin *et al.*, *Sci. Rep.* **10**, 15078 (2020) [204]. Copyright 2020.

data access. To illustrate the potential of our technology for large volume pathology screening, we established an “intrinsic marker” for the colorectal disease that detects tissue with dysplasia or colorectal cancer and flags specific areas for further examination, potentially improving the efficiency of existing pathology workflows [169]. Figure 35 presents the automated processing workflow for SLIM images, and the procedure for tissue classification. In short, cancer is detected through these two parameters: solidity (“glandular solidity”) and median phase value. We use a support vector machine (SVM) to determine their optimal fusion (Fig. 36). We can see that the flagged regions based on the SVM model agree well with the classifications by the pathologist in Fig. 37.

4.2b. Cancer Diagnosis

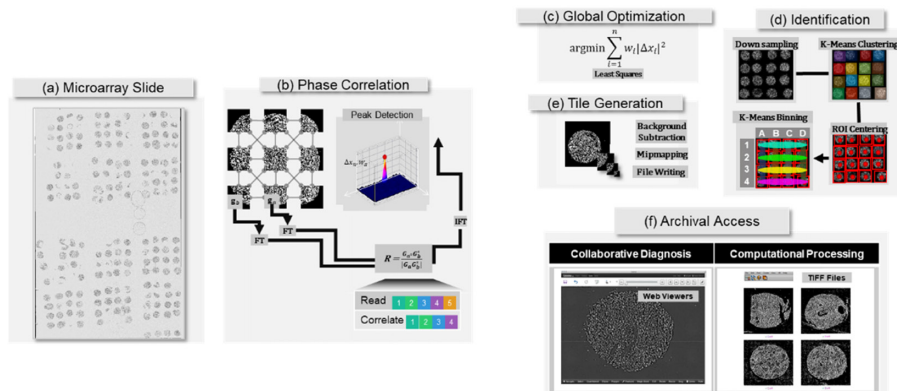
Normal and diseased tissues are characterized by different scattering parameters. Thus, SLIM can serve as a scattering-based diagnosis tool by measuring the scattering mean-free path l_s and anisotropy factor g , defined as [207]

$$l_s = \frac{L}{\langle \Delta\phi^2(\mathbf{r}) \rangle_r}, \quad (60)$$

$$g = 1 - \left(\frac{l_s}{L} \right)^2 \frac{\langle |\nabla[\phi(\mathbf{r})]^2| \rangle_r}{2k_0^2}. \quad (61)$$

Here, $L \ll l_s$ is the tissue slice thickness, $\langle \Delta\phi^2(\mathbf{r}) \rangle_r = \langle [\phi(\mathbf{r}) - \langle \phi(\mathbf{r}) \rangle_r]^2 \rangle_r$ is the phase variance, and k_0 is the wavenumber of the illumination. The definition of g (anisotropy) is the average cosine of the scattering angle associated with a slice of thickness l_s . This way, the assumption that the tissue is made of discrete particles

Figure 35

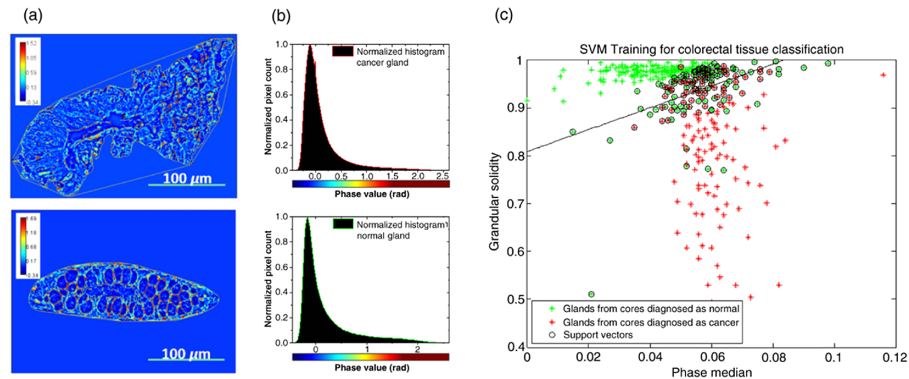


Automated processing workflow for gigapixel SLIM images. (a) Typical samples used in this paper consist of tens of thousands of tiles. (b) The tiles are assembled using a “phase correlation” scheme where the optimal displacement between neighboring tiles is determined by the location of the peak in the correlation image. (c) In our implementation disk access is overlapped with the correlation procedure, with performance dependent on the longer disk read and write operations. (d) Disagreements between estimated tile positions are resolved with a least-squares fit, and the resulting positions are used to generate image pyramids typically used for archival access. (e) Optimally, regularly spaced tissue microarray cores are cropped and labeled by way of a thresholding technique. (f) Resulting images are ready for computational processing and collaborative diagnosis. Reprinted with permission from Kandel *et al.*, *J. Biomed. Opt.* **22**, 66016 (2017) [169].

is removed. Figure 38(a) shows the SLIM image of a tissue slice cut from a three-month-old rat liver. The scattering mean-free-path map and the anisotropy factor map are shown in Figs. 38(b) and 38(c).

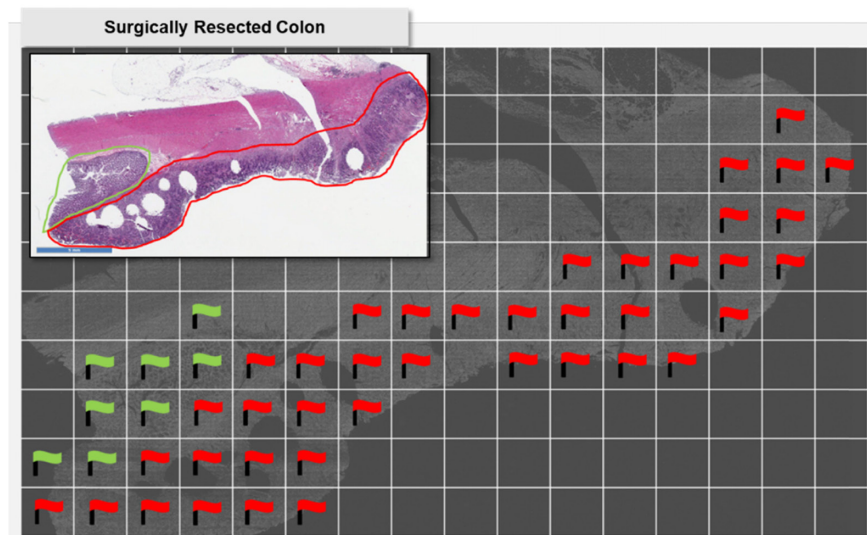
Another metric that can potentially be an intrinsic cancer marker is the spatial auto-correlation length, defined as the variance of the autocorrelation function of the

Figure 36



Quantitative parameters for classification. Our classification method augments phase information with the geometric structure of the gland. Scanned images are manually segmented into glands, whose solidity (“glandular solidity”) and median phase value are used to train the SVM-based classifier used in this work. (a) Gland identification, (b) feature extraction, and (c) classification. Reprinted with permission from Kandel *et al.*, *J. Biomed. Opt.* **22**, 66016 (2017) [169].

Figure 37

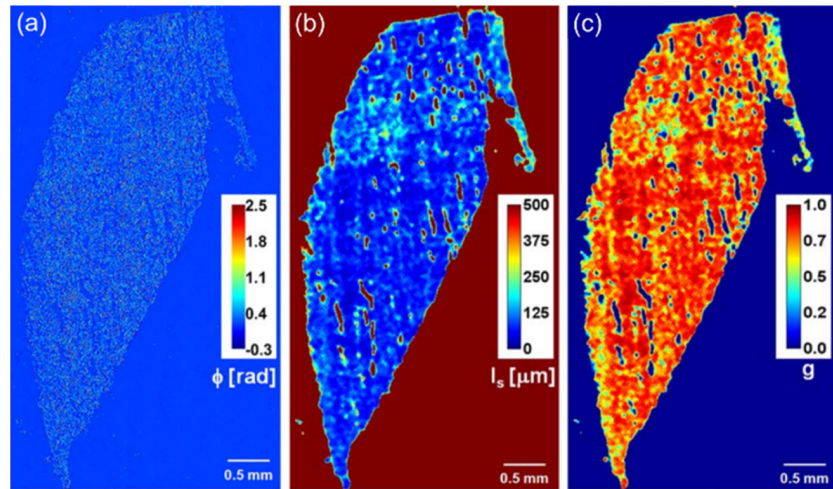


Biopsy flagged with regions of “high” (red) and “low” (green) suspicion. After assembly, the image was analyzed in chunks of $10,000 \times 10,000$ pixel regions with glands in each region evaluated according to the SVM model. The consensus of constituent glands is represented with a green or red flag, indicating low or high index of suspicion, respectively. Inset: H&E stained parallel section, showing the red-bordered tumor and green-border benign region, as indicated by the pathologist. Reprinted with permission from Kandel *et al.*, *J. Biomed. Opt.* **22**, 66016 (2017) [169].

phase from SLIM images [209]. Figure 39 presents the SLIM images, the spatial autocorrelation maps, and the spatial autocorrelation maps after filtering.

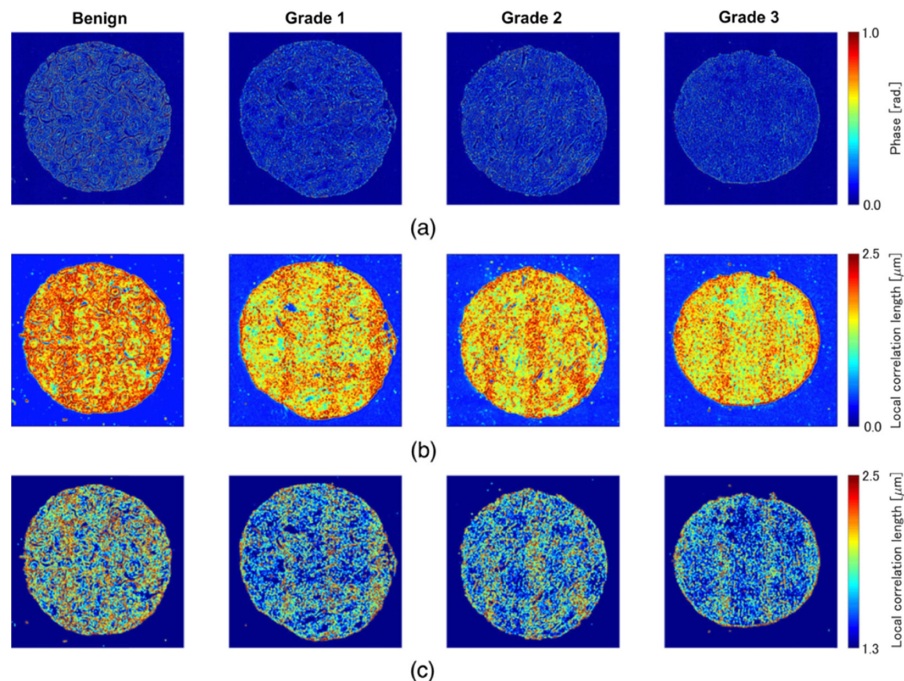
Figure 40 shows the comparison between the H&E stained bright-field microscopy and SLIM images [210]. Pathologists can be trained with SLIM images to diagnose cancer with about 88% agreement with the results diagnosed with H&E images [210].

Figure 38



Maps of (a) ϕ , (b) l_s , and (c) g for a tissue slice across an entire rat liver; the g map is thresholded to show $g = 0$ for background. Color bars show ϕ , l_s , and g , as indicated. Reprinted with permission from [207]. Copyright 2011 Optical Society of America.

Figure 39



Example of local spatial autocorrelation length maps. (a) Quantitative phase images, (b) local correlation length maps, and (c) local correlation length maps. Reprinted with permission from Takabayashi *et al.*, *J. Biomed. Opt.* **24**, 016502 (2019) [209].

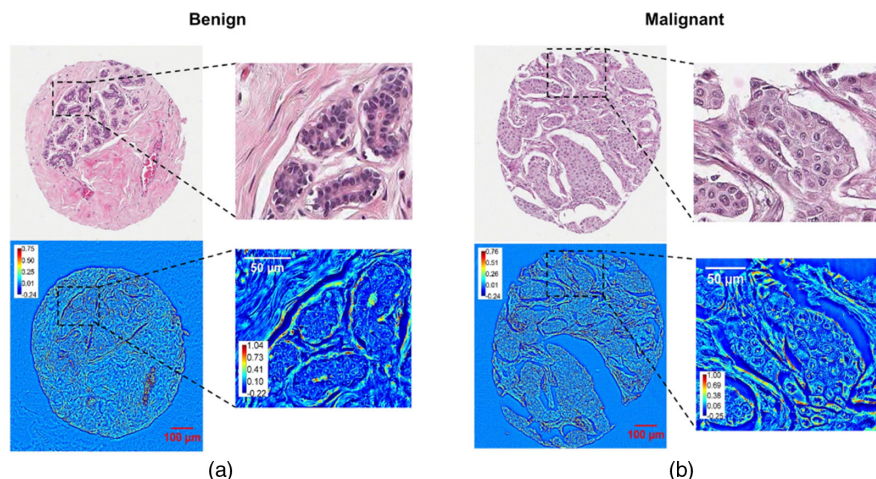
With machine learning techniques, the accuracy of diagnosis can be improved, which we will discuss in detail in Section 5.

4.2c. Cancer Prognosis

Cancer prognosis is an estimate of how the disease will proceed. It includes the recovery rate, the recurrence rate, and the clinicians' predictions for the course of the disease. Cancer prognosis can be affected by many factors, such as the type of cancer, the stage of cancer, cancer's grade, and certain traits of the cancer cells. SLIM can help with cancer prognosis in the aspects of cancer recurrence rate and tumor progression [211,212].

Prediction of the recurrence risk of prostate cancer is after prostatectomy critical for determining whether the patient would benefit from adjuvant treatments. The method based on the optical anisotropy g [see Eq. (61)] of SLIM images can identify recurrent cases with 73% sensitivity and 72% specificity, which is superior for the same sample set to that of CAPRA-S, a current state-of-the-art method. Optical anisotropy g was calculated in the single stromal layer adjoining 6–18 glands from each of the 33 patients with post-prostatectomy biochemical recurrence of prostate cancer and 159 patients who did not have a recurrence. The calibrated anisotropy value in the recurrent cases (0.913 ± 0.028 ; median = 0.92) was lower than that in the non-recurrent cases (0.932 ± 0.023 ; median = 0.938). The difference in anisotropy values in the cancer-adjacent stroma from the recurrent and non-recurrent groups was statistically significant (one-way ANOVA, $p = 7.05 \times 10^{-5}$). Figure 41(a) summarizes these results. Kaplan–Meier survival analysis was performed to test the utility of anisotropy for predicting biochemical recurrence as the end-point. The anisotropy ranges tested were 0.68–0.93 (67 patients) and 0.93–0.97 (125 patients), and the results are shown in Fig. 41(b). The figure shows that patients with low anisotropy values had a higher likelihood of disease progression. The three-year and five-year recurrence-free probability dropped from 95% and 90%, respectively, for patients with high anisotropy values to 70% and 65%, respectively, for patients with low anisotropy values. The

Figure 40



Comparison between H&E stained bright-field microscopy (top row) and SLIM (bottom row) images in their respective abilities to resolve tissue morphology for (a) benign and (b) malignant cases. The H&E images were obtained from stained sections that were adjacent to the unstained sections used for SLIM imaging. Color bars are in radians. Reprinted with permission from Majeed *et al.*, *J. Biomed. Opt.* **20**, 111210 (2015) [210].

comparison of the ability of anisotropy to other methods is shown in Fig. 41(c) using the receiver-operating curve analysis.

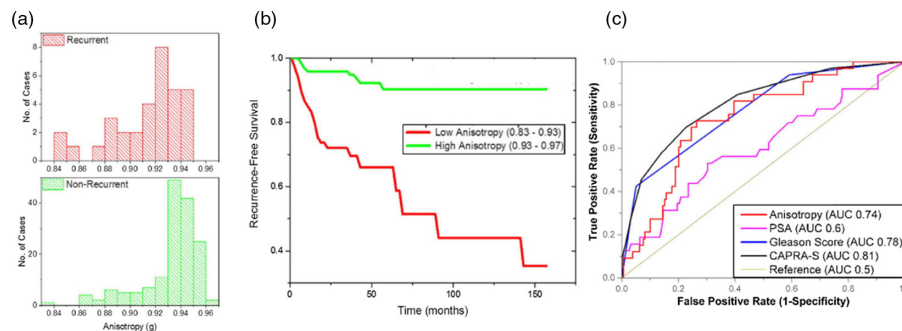
SLIM can also assist with the pancreatic ductal adenocarcinoma (PDAC) prognosis by quantitative analysis of the PDAC fiber structures [213]. Fibrillar collagen in PDAC exhibits an inverse relationship between survival data and fiber width and length ($p < 0.05$). PDAC patients with high alignment per length of segmented fibers show significantly reduced survival rates [Fig. 42(a)]. In low survival cases, fiber width and length were greater [Figs. 42(b) and 42(c)]. The straightness has less predictive value in survival rates [Fig. 42(d)]. SLIM was also used for the prognosis of breast cancer [183].

4.2d. SLIM as Assisted Reproductive Technology

The high incidence of male factor infertility affects human and animal reproduction. The ability to evaluate sperm at the microscopic level, at high throughput, is valuable for assisted reproductive technologies (ARTs), as it can allow specific selection of sperm cells for *in vitro* fertilization (IVF). SLIM, as a non-invasive label-free imaging modality with high sensitivity, can assist with this task [214].

To introduce specificity to SLIM images, we trained a deep-convolutional neural network to perform semantic segmentation, which we will discuss more in detail in Section 6. This method can efficiently analyze thousands of sperm cells and identify correlations between dry-mass content and artificial-reproduction outcomes.

Figure 41



(a) Histograms of the distribution of anisotropy in the single layer of stroma surrounding 6–18 glands from 33 patients with post-prostatectomy biochemical recurrence of prostate cancer and 159 non-recurrent patients. The bin size on the histogram was set at 0.02. The anisotropy value is lower in the recurrent patients, compared to the non-recurrent patients (one-way ANOVA, $p = 7.05 \times 10^{-5}$) (b) Kaplan–Meier survival curve with end-point as disease recurrence for 67 patients with low anisotropy values (0.83–0.93) and 125 patients with high anisotropy values (0.93–0.97). (c) Comparison of recurrence prediction metrics. The performance of anisotropy measured on quantitative phase images, pre-surgical prostate-specific antigen (PSA) levels, Gleason score, and CAPRA-S as post-prostatectomy biochemical recurrence predictors was studied in 192 prostatectomy cases (33 recurrent, 159 non-recurrent). The best performance was observed with CAPRA-S (AUC 0.81) and Gleason scores (AUC 0.78). The discriminatory ability of anisotropy (AUC 0.74) was lower than that of CAPRA-S and Gleason score. However, at the optimal performance point, anisotropy had a sensitivity of 72.7% and specificity of 73.6% compared to the 69.6% sensitivity and 77.4% specificity of CAPRA-S. Pre-surgical PSA level (AUC 0.6) was a poor predictor of recurrence. Reprinted by permission from Macmillan Publishers Ltd.: Sridharan *et al.*, *Sci. Rep.* **6**, 33818 (2016) [211]. Copyright 2016.

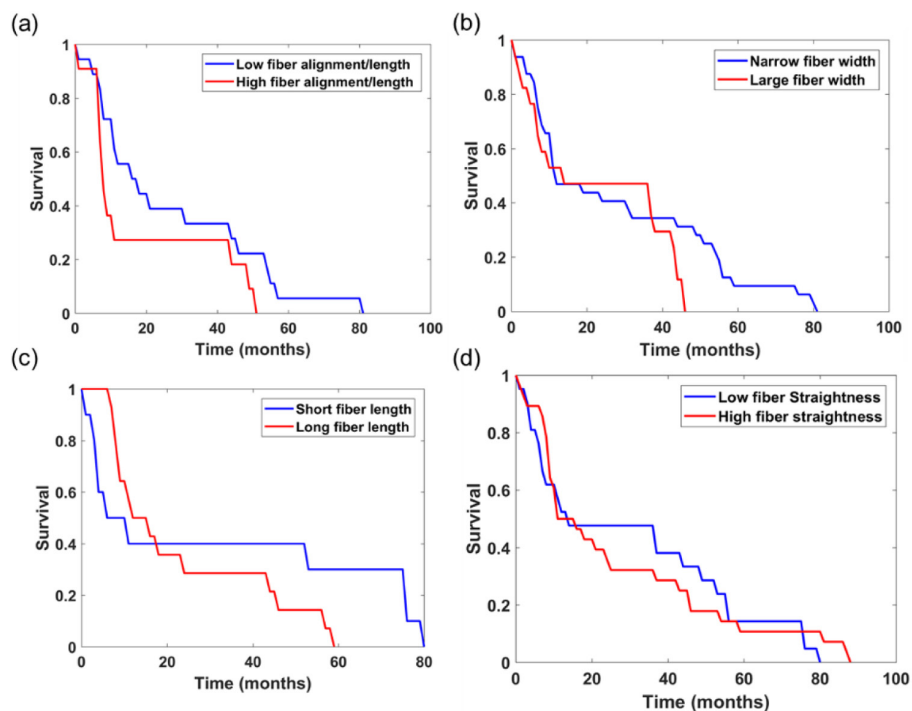
Specifically, we found that the dry-mass content ratios between the head, midpiece, and tail of the cells can predict the rate of success for zygote cleavage and embryo blastocyst formation. Figure 43(a) shows a mosaic made from 27,000 tiles, covering an area of 7.1 cm². After the halo removal procedure [Fig. 43(b)], the 3D reconstructed sperm cell is shown in Fig. 43(c). The summary of the outcomes with this method will be presented in detail in Section 5.

4.2e. Blood Testing

Impedance counters and flow cytometers are common laboratory methods to detect, identify, and count specific cells from blood samples. However, those methods are often limited to population-level statistics for morphology and bulk measurement in the case of hemoglobin concentration. In some cases, the morphological properties of a single blood cell are necessary for diagnosis such as leukemia [215–217]. The morphological properties are also important to assess the banked blood because stored red blood cells (RBCs) undergo numerous biochemical, structural, and functional changes, commonly referred to as storage lesions. SLIM can measure the thickness, refractive index, and membrane fluctuation of the RBCs, which can report further on the cell stiffness [218]. This property directly affects the cell's ability to transport oxygen in the microvasculature.

Figure 44(a) presents the temporal standard deviation (σ_T) map from the 128 SLIM images. The histogram of the σ_T map is shown in Fig. 44(b). The arrow points to the spatial average of the σ_T map, which we use as the representative displacement parameter for the particular RBC. The histograms of the σ_T for different weeks are summarized in Fig. 44(c). The arrows show the mean phase fluctuation

Figure 42



Kaplan–Meier survival curves for pancreatic ductal adenocarcinoma (PDAC), comparing different grades of (a) fiber alignment/length, (b) fiber width, (c) fiber length, and (d) fiber straightness. Log-rank χ^2 of 50.7 (str), 37.43 (width), 25.7 (al), and 50.8 (length). Reprinted with permission from Fanous *et al.*, Biomed. Opt. Express **11**, 1354–1364 (2020) [213].

of $N = 110 \pm 15$ cells. It can be seen that the position of these arrows consistently shifts toward lower values with time, indicating that the cell stiffness increases over time.

The mean cell hemoglobin (MCH) can be obtained by calculating the dry mass of the RBCs. Figure 45 depicts the MCH as a function of storage time for all the samples. Note that the MCH does not change with storage time. This result indicates that, while cells can undergo volume changes during storage, they do not lose hemoglobin into the storage solution.

5. EMERGING TRENDS IN SLIM IMAGING

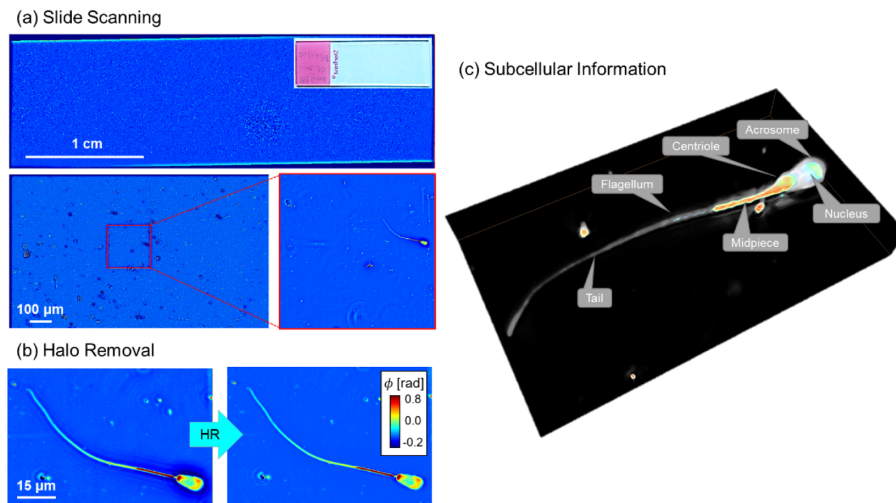
5.1. Phase Imaging with Computational Specificity

Phase imaging with computational specificity (PICS) aims to use recent advances in artificial intelligence to introduce specificity for structures or biological processes with the ultimate goal of simplifying the analysis of label-free data [219]. This is typically accomplished by providing a semantic segmentation feature map where a class label is assigned to each pixel in the phase map.

Central to these AI approaches was the development of neural networks capable of efficiently integrating local textural information with contextual shape information such as the U-Net architecture [220].

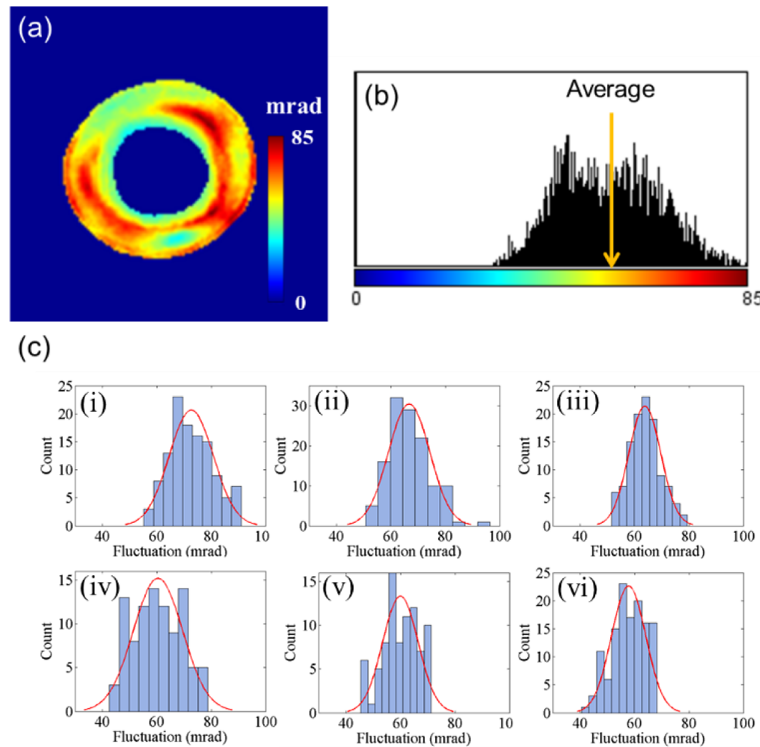
In general, deep-convolutional neural networks consist of a series of pixel-wise non-linear operations that remap the values in the input image into another form such as a

Figure 43



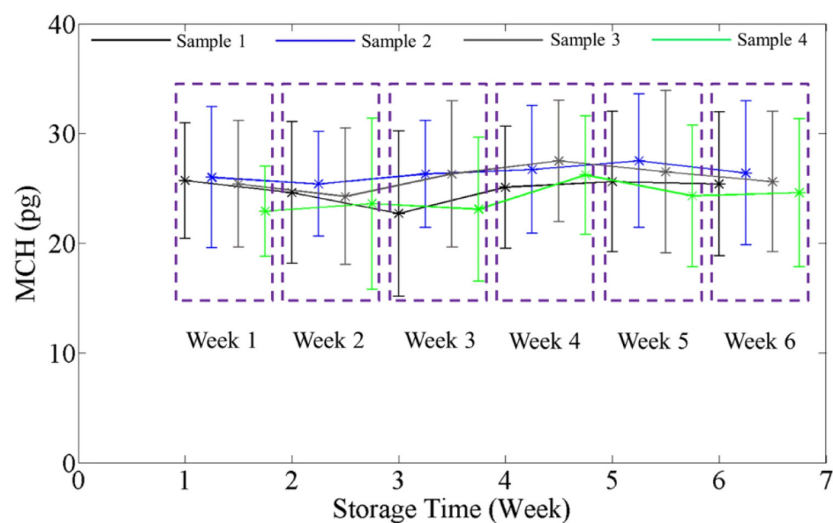
SLIM can image sperm as a fully automated slide scanner, with thousands of samples on each slide. (a) A large number of samples in each slide motivates the use of automated segmentation techniques. (b) The superior sensitivity of SLIM images is, in part, due to the use of spatially and temporally broadband fields. The partially coherent illumination corrupts the low frequencies, evident as a halo glow surrounding the cell. The halos are corrected by solving a nonlinear inverse problem. (c) Tomographic rendering of a spermatozoon using SLIM. The mitochondria-rich midpiece appear as substantially higher in dry-mass density. Rendering of the tomogram was performed using AMIRA with the “physics” colormap corresponding to high phase values and a gray-scale colormap corresponding to the lower phase values in the nucleus and tail. Reprinted with permission from Kandel *et al.*, Proc. Natl. Acad. Sci. USA **117**, 18302–18309 (2020) [214].

Figure 44



RBC fluctuation: (a) Temporal standard deviation map of a single RBC. (b) Histogram of the STD map in (a); a representative average of the STD map is shown by the arrow. (c) Histogram of the average STD values for 110 6 15 RBCs at different weeks. Reprinted by permission from Macmillan Publishers Ltd.: Bhaduri *et al.*, *Sci. Rep.* **4**, 6211 (2014) [218]. Copyright 2014.

Figure 45

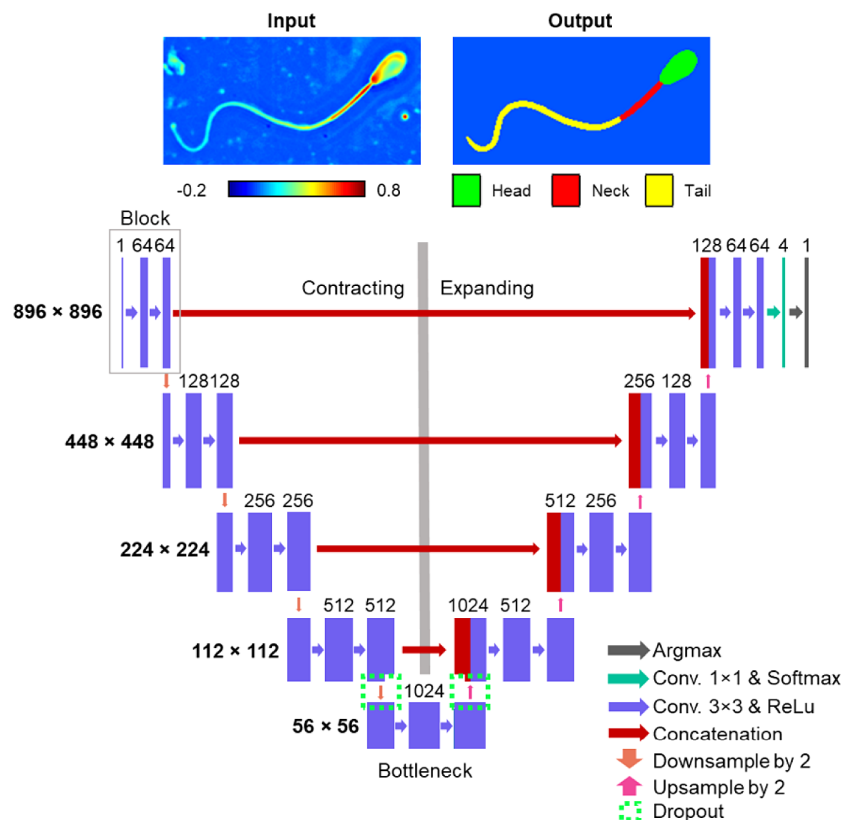


Variation in mean cell hemoglobin with storage time. Data points for different samples are shifted to distinguish them from each other and grouped by the week of the measurement. The error bars in the plots are twice the standard deviation of the MCH calculated over the groups of cells (N 5 110 6 15). Reprinted by permission from Macmillan Publishers Ltd.: Bhaduri *et al.*, *Sci. Rep.* **4**, 6211 (2014) [218]. Copyright 2014.

single number, class probability vector, or whole image [221,222]. The architecture shown in Fig. 46 is divided into a “contracting” and “expanding” path that is linked by a “bottleneck” at the bottom. Importantly, the U-Net architecture includes concatenation layers that copy the output from previous levels to stabilize the training procedure, which in turn results in an improvement in resolution.

Each “block” of the contracting path results in a smaller version of the input image that has been processed in a nonlinear way. We note that without nonlinear operations, the entire neural network transformation could reduce to a single convolution. The first block consists of a filter bank of randomly initialized convolution kernels that expand the number of channels in the input image [223]. The values of the convolution kernels are updated at each training step so that the network output will, hopefully, converge to the training data after some number of optimization steps. To introduce nonlinearity, the convolution is paired with a nonlinear “activation” function such as a threshold that removes negative outputs [224] or otherwise has

Figure 46



U-Net architecture consists of several nonlinear operations that map one image into another. In this case a SLIM image is mapped into an annotated image. The series of operations, or architecture, consists of a contracting path that decreases the height and width of the image while increasing the number of channels. After passing the “bottleneck” the image is upsampled and the number of channels is reduced. In U-Net the contracting path is connected to the expanding path at each layer with a concatenation operation that improves accuracy and provides numerical stability during training. During training random convolution at the bottleneck is removed (dropout) to introduce a degree of redundancy and regularization in the network. Reprinted with permission from Kandel *et al.*, Proc. Natl. Acad. Sci. USA **117**, 18302–18309 (2020) [214].

some saturation effect [225]. After application of the convolution and activation, the resulting images resemble a distorted version of the input, and the operation is repeated a second time with different weights. The values are propagated to the next block by downsampling the image such that successive blocks decrease the image size while increasing the number of channels. After passing the “bottleneck”—the point in the network where the data has the lowest resolution but the greatest number of channels—the image is successively upsampled by a series of blocks where the resolution is increased, and the number of channels decreased. In those blocks, an upsampling operation is used to increase the resolution, and convolution is used to decrease the number of channels. These operations are followed by nonlinear activation. To improve numerical stability, the input to the filter bank is combined with the output of layers that have matching dimensionality. The result of this procedure is a many channel image equal to the size of the input, and a final convolution and activation result in the target output.

5.2. SLIM and AI in Cell Biology

Fluorescence microscopy addresses the principle deficit of scattered light imaging, by highlighting stains or proteins that are specific to molecular structures or cellular chemistry [226]. This modality is compatible with SLIM imaging as the modulating element in SLIM can be easily configured to behave like a mirror and, therefore, it is straightforward to co-localize fluorescence and phase images on the same camera. Alternatively, in non-commercial designs, which are prone to ambient light leakage, separate light paths have been employed to measure more challenging specimens such as fluorescently conjugated antibodies and proteins [58,111,192]. While straightforward, multiplexing fluorescence microscopy and phase imaging negate many of the advantages of SLIM by introducing contrast agents, increasing phototoxic stress, and decreasing acquisition rates.

Fortunately, recent developments in artificial intelligence (AI) offer a way to perform label-free imaging while maintaining the specificity advantage associated with fluorescence microscopy. In PICS, these computationally generated annotations are used to analyze the SLIM data for parameters such as the cellular dry mass [171].

One of the biggest challenges in live-cell imaging is the automated analysis of high-content time-lapse sequences used in drug discovery [227]. In general, these sequences consist of several experimental conditions segregating into wells that are imaged at fixed intervals (Fig. 47). With thousands of individual cells monitored over weeks, data volumes and observational bias have motivated the development of purely computational analysis strategies. For these applications, co-localized fluorescence and phase images are readily available to generate semantic segmentation maps for PICS-style experiments.

This approach is illustrated in (Fig. 47) and is motivated by the ability of deep-convolutional neural networks [228] to perform image-to-image translation [222,229,230]. In short, a time-lapse sequence consisting of the biologically relevant portion of the experiment is acquired without labels. Then, the cells are fixed and stained followed by co-localized fluorescence and QPI imaging to produce a training corpus that estimates the fluorescent signal. After training, the resulting neural network is applied to the unstained time-lapse sequence. In this way, staining is avoided during the biologically relevant portion of the experiment.

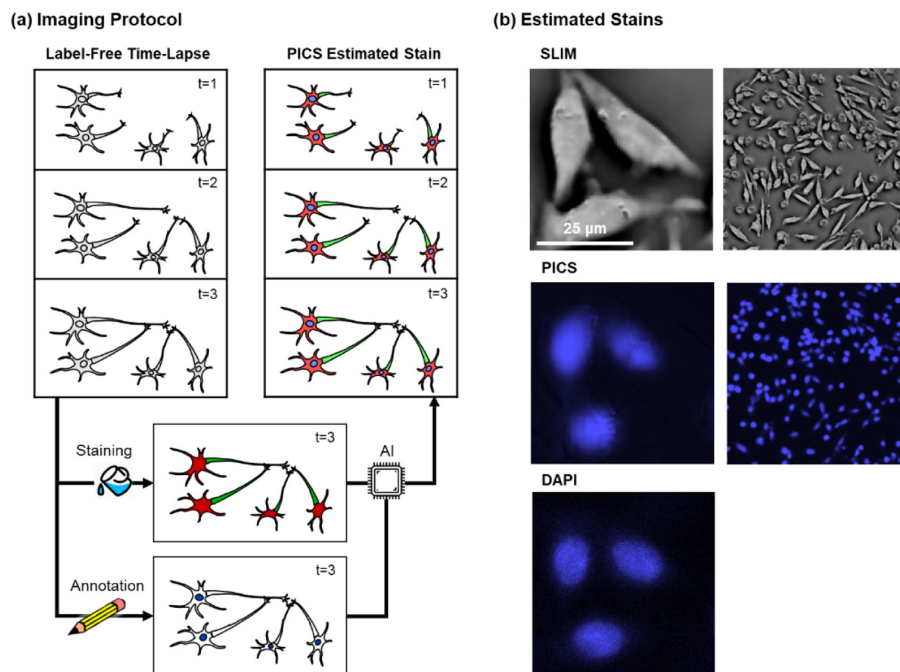
When this procedure is applied to SLIM imaging, the SLIM system can estimate the DAPI stain with only a small loss of resolution that plays little role in semantic segmentation (Fig. 47). The associated semantic maps are then used to perform a per-cellular compartment analysis of the data [171]. While the principal motivation

for PICS is to avoid toxicity or destructive fixation due to fluorescent stains, a further advantage comes from the digital nature of the procedure. The transmitted light signal is often more intense than in fluorescence microscopy, meaning that the PICS estimated signal is typically an order of magnitude faster to acquire compared with its true chemical counterpart [171,219]. Additionally, as PICS staining is a digital process, a larger number of fluorescent stains can be estimated from a single label-free image than what is otherwise possible with conventional spectral-based fluorescence multiplexing strategies.

Although an emerging technology, PICS has been shown relevant for a variety of cellular systems. The initial PICS publication [171] included SW480 and SW620 cells, which are cancer cells derived from the same patient and are frequently used to study disease progression. In that work, it was shown that PICS could replace DiI and DAPI stains. Importantly, PICS provided an automated and label-free approach to estimate the ratio of nuclear and cytoplasmic dry mass, which is a prognostic marker for cancer progression (for example, in [231]).

When PICS was first presented, two important observations were made: 1) that training could be performed on fixed (dead) cells and evaluated on living (unmodified) specimens and 2) that the neural network was surprisingly tolerant to variations in cellular morphology. The latter was evidenced by the ability of the network to be trained on more round, stressed, and confluent cells at the end of the experiment with

Figure 47



PICS imaging for estimating fluorescent signals. (a) Live-cell imaging with computational specificity is performed in two imaging steps. During the first step, unmodified cells are imaged using a label-free technique such as SLIM. After the experiment is over, the cells are stained and imaged with co-localized fluorescence producing a raining corpus for the neural network. After the network is trained, it can be used to digitally stain the experiment, thus avoiding a toxic chemical staining. (b) PICS performance closely matches chemical analogs ($20\times/0.3$). Reprinted by permission from Macmillan Publishers Ltd.: Kandel *et al.*, Nat. Commun. **11**, 6256 (2020) [219]. Copyright 2020.

the inference still accurate for intact fibroblast shapes observed at the start of the experiment. This observation further contributes to the trend where computational neural networks are understood to learn more general rules that are applicable beyond the dataset used to train them. Further, the same training corpus was used for both cell lines (SW480 and SW620). Additionally, due to the high sectioning and suppression of multiple scattering in QPI, it was possible to perform PICS-style imaging in liver cancer spheroids using a purely 2D training approach. This approach should be relatively straightforward to extend to 2.5D and 3D network architectures [232].

As an emerging technique, the limitations of PICS-style imaging are the subject of current investigations and are usually phrased in terms of the ability of the underlying network to learn the image remapping. The preferred quality scores are derived from the Pearson correlation between actual and imputed fluorescence, as well as more wholistic measurements such as cell counts performed on training pairs. When considering a nuclear stain such as DAPI, it was observed the neural network had “learned” (or more formally responded to) both local textural information as well as higher-order features adjacent to the cells. Therefore, the network incorporated morphological information from sounding regions to estimate the expected DAPI signal.

The extent to which morphology contributes to protein concentration estimation was experimentally evaluated in subsequent work [233]. There, PICS was used to impute fluorophores associated with antibody staining—specifically Tau and MAP2 concentration levels, a pair of proteins whose differential expression distinguished between axons and dendrites [234]. The associated semantic maps were then used to measure dry-mass traffic inside the annotated structures using the DPS method mentioned in previous sections [199].

The observation that morphology could serve as a proxy for staining levels was further validated in [235], where PICS was used to overcome the toxicity of a common cellular viability assay. In that work, the commonly used, but toxic, system of Hoechst 33342 and SYTOX Green provided a chemically motivated fluorescent marker for cellular viability. To produce a network capable of matching the stain, the U-Net architecture was revised to use MobileNet blocks following Google’s EfficientNet proposal [236]. Next, transfer learning from ImageNet was used to boost accuracy. As cell viability is primarily a function of membrane integrity and is only readily identifiable in the most pathological of cases, within a broader context, PICS continues a trend in machine learning where computers can identify features with more accuracy than human annotators.

5.3. SLIM and AI in Pathology

SLIM imaging in conjunction with artificial intelligence offers a solution to outstanding challenges in digital pathology. As histopathological resected tissue is most often imaged with the aid of exogenous contrast agents such as H&E [111,237], variability in staining procedures can frustrate comparison across specimens and instruments. In addition to variation introduced during the staining procedure, diagnosis is performed by a pathologist, which leads to observational bias and errors. Lastly, many procedures in pathology are labor-intensive, and the non-trivial time to analyze samples often puts a practical limitation on morphological analysis.

In this context, it is not surprising that early efforts were made to automate diagnosis on SLIM images using what are today considered “classical” methods. A step towards removing observational bias was taken in [169], where the phase values inside the glands were used to identify tissue as potentially cancerous. In that work, features

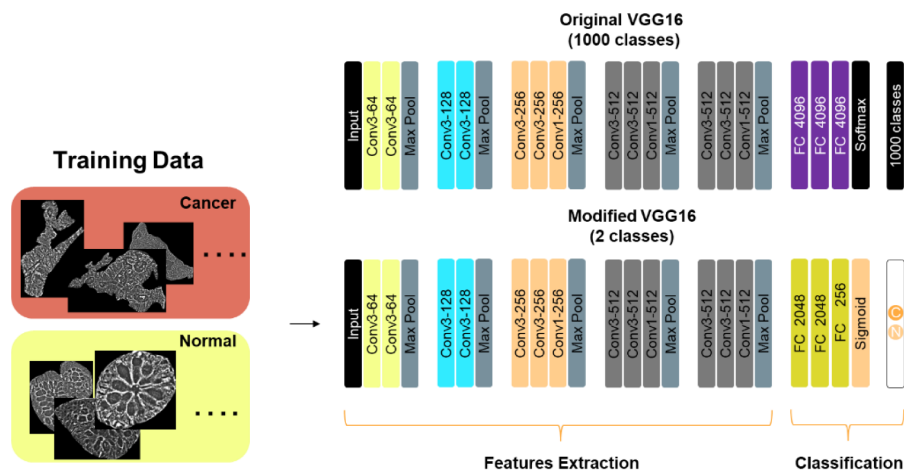
derived from tissue glandular solidity (fill factor) and structural anisotropy were combined in a nonlinear fashion using a SVM [238]. A similar procedure was developed, where a VGG16 convolutional neural network [239] was used to implicitly generate and combine those classical features (Figs. 48 and 49) [240].

While these methods helped address observational bias, they nevertheless required a pathologist to manually circumscribe the gland. A step towards fully automated analysis was taken in [241], where “texons” were used to produce a semantic segmentation map. In that approach, much like in convolutional neural networks, a filter bank is used to expand the SLIM image into a series of variations, which are nonlinearly composited to form a semantic segmentation map. This procedure was, ultimately, used to grade prostate cancer biopsies [241].

The tradeoff between intrinsic imaging and external contrast agents is particularly acute in reproductive pathology. When inspecting gametes such as sperm cells, the use of fluorescence labels has enabled new cell-sorting strategies and given insights into developmental biology. Nevertheless, these methods are considered too invasive for use in a clinical setting. Thus, artificial reproduction procedures such as intracytoplasmic sperm injection rely on transmitted light imaging [242]. These microscopes are most often boosted with label-free contrast enhancement techniques such as DIC, phase-contrast, or Hoffman modulation contrast. Invariably, similar difficulties arise to those encountered when analyzing cancer biopsies, namely that the data is qualitative and subject to acquisition specific variation, and the analysis is subject to the judgment of a pathologist. In addition to observational bias, relying on human observers makes it time-consuming to ascertain morphological features such as the dimensions of the organelles within a population of cells [243]. While a tedious morphological annotation can be performed by hand for fixed specimens [233], it is difficult to imagine manual annotation for time-critical decisions such as when selecting live, moving, sperm cells.

In these cases, SLIM imaging can be used to perform interferometrically normalized data acquisition, while artificial intelligence can automatically annotate the samples. This approach is exemplified by the efforts in [214] to relate morphological

Figure 48

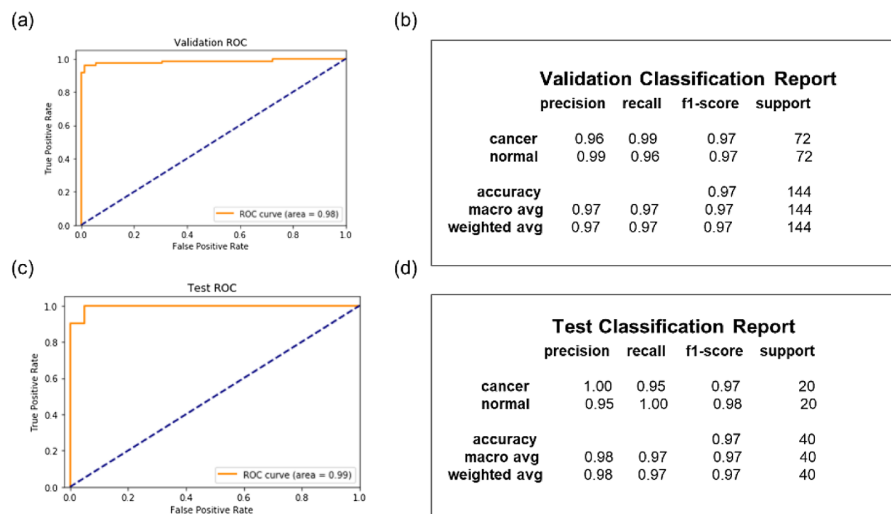


Modified VGG16 network. Input image size is $256 \times 256 \times 3$. A pad of length 1 is added before each Max Pool layer. Conv1, convolutional layer with 1×1 filter; Conv3, convolutional layer with 3×3 filter; Max Pool, maximum pooling layer over 2×2 pixels (stride = 2); all hidden layers are followed by RELU activation. First FC layer is followed by 0.5 dropout. Reprinted with permission from Zhang *et al.*, APL Photon. **5**, 040805 (2020) [240]. Copyright 2020 AIP Publishing LLC.

differences in sperm cells with reproductive outcomes (Fig. 50). In that work, the authors digitized a large number of slides generated from animals with known fertility rates. A large number of samples motivated an end-to-end analysis strategy based on machine learning. A U-Net architecture was trained to segment the spermatozoan into compartments [220]. The training was performed unconventionally, with a two-step procedure resembling a generative adversarial network [244]. This procedure aimed to produce a larger training corpus in a time-efficient manner and consisted of a fine annotation performed on a limited dataset. Then, a coarse correction was performed, followed by a final training round. It was found that the neural network training procedure was able to merge differences between annotators, which in turn helped to mitigate intraobserver variation. The semantic segmentation was used to address a biologically relevant question, specifically, the effect of morphology on cleavage and blastocyst rates. The results (Fig. 51) confirmed the well-known theory that fertilization success is connected to hydrodynamic properties while providing further, although somewhat indirect, evidence that blastocyst formation rates are connected to male-factor cytoskeletal structures such as the centriole.

In the broader context of AI algorithms, it was observed that semantic segmentation-based scoring was able to inform better on the underlying biological process when compared to end-to-end metrics. Specifically, by having an annotated image rather than a single number for each cell's "fertility" potential, the authors were able to interpret their results in terms of hydrodynamic properties as well as identify important cellular ultrastructures within the semantic maps (such as the centriole). A further motivation for using semantic segmentation was the lack of a direct correspondence between individual sperm cells and reproductive fate. Unsurprisingly, constructing a training corpus, for example, one where individual sperm cells are matched to fertility

Figure 49



Receiver-operating characteristics (ROC) curve, with AUC (area under the curve), and classification reports for the validation dataset and the test dataset, respectively. The AUC score is 0.98 for the validation dataset and 0.99 for the test dataset, as indicated. The two classes, cancer and normal, have balanced support for both the validation dataset and the test dataset, with the validation dataset providing 72 actual occurrences for each class and the test dataset providing 20 actual occurrences for each class. The accuracy hits 97% for both the validation and the test. Reprinted with permission from Zhang *et al.*, *APL Photon.* **5**, 040805 (2020) [240]. Copyright 2020 AIP Publishing LLC.

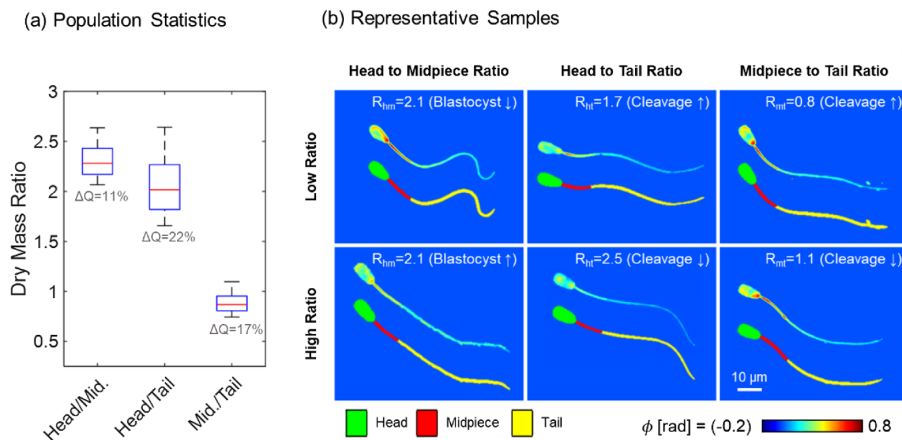
outcomes, remains the greatest challenge for using AI in reproductive medicine. However, the ability of SLIM to generate pairs of phase and fluorescence images from the same field of view greatly simplifies the problem of generating ground truth data. For several applications, it has been shown that these data can be generated automatically, with no manual intervention.

6. SUMMARY AND OUTLOOK

In sum, we described SLIM as a label-free imaging method, which upgrades existing phase-contrast microscopes and, thus, can make a broad impact in the field by its ease of adoption. Not surprisingly, SLIM suffers from certain limitations as well. Because it relies on the incident light as the reference for its interferometric principle, SLIM produces lower contrast images as the specimens become thicker, subject to multiple scattering (Fig. 52). This limitation was the motivation for creating gradient light interference microscopy [26]. The acquisition rate in SLIM is limited by the liquid crystal modulator to ~ 12 – 15 frames/s, depending on the time devoted to SLM stabilization. While this temporal resolution is adequate for most dynamic biological phenomena associated with live cells, it is insufficient for measuring fast phenomena, such as action potentials. Finally, the SLM at the heart of the SLIM operation is an expensive component, especially when a high refresh rate is desired.

However, SLIM combines certain features that are matched by existing QPI instruments. Common-path interferometry and white-light illumination allow for speckle-free and sub-nanometer path-length stability, as shown in Sections 2 and 3. The phase in the SLIM image is reconstructed with four intensity frames corresponding to each phase shift. The halo effect from the phase-contrast microscope can be

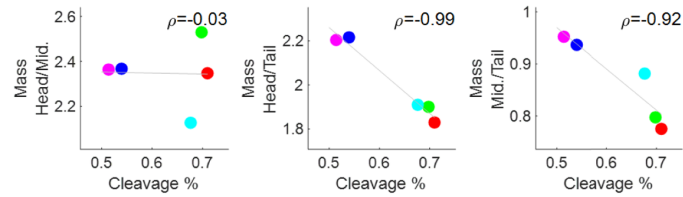
Figure 50



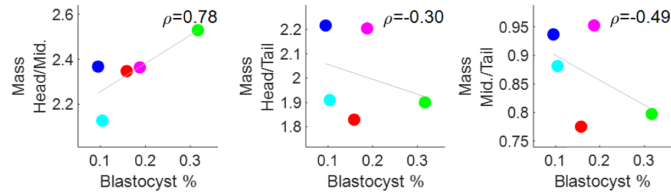
Deep learning tracks subtle but significant differences in sperm morphology. (a) A histogram of the distribution of sperm dry-mass ratios shows that structural differences between sperm cells are relatively narrow, as evidenced by the percentage difference between the first and third quartiles, for the head to midpiece, head to tail, and midpiece to tail are (only) 11%, 24%, and 17%, respectively. (b) Dry-mass maps of representative sperm cells along with semantic segmentation are labeled with their dry-mass ratios (R_{hm} , R_{ht} , R_{mt}). Additionally, \uparrow denotes an increase or \downarrow a decrease in ART outcome. These differences are especially difficult to visualize with conventional techniques, as typical microscope images are not proportional to dry mass and the naked eye is unable to segment, integrate, and divide portions of an image ($40\times/0.75$, SLIM). Reprinted with permission from Kandel *et al.*, Proc. Natl. Acad. Sci. USA **117**, 18302–18309 (2020) [214].

Figure 51

(a) Embryo Cleavage

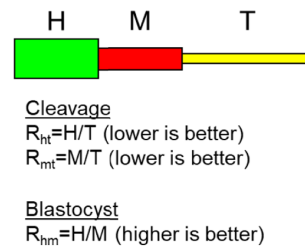


(b) Blastocyst Formation



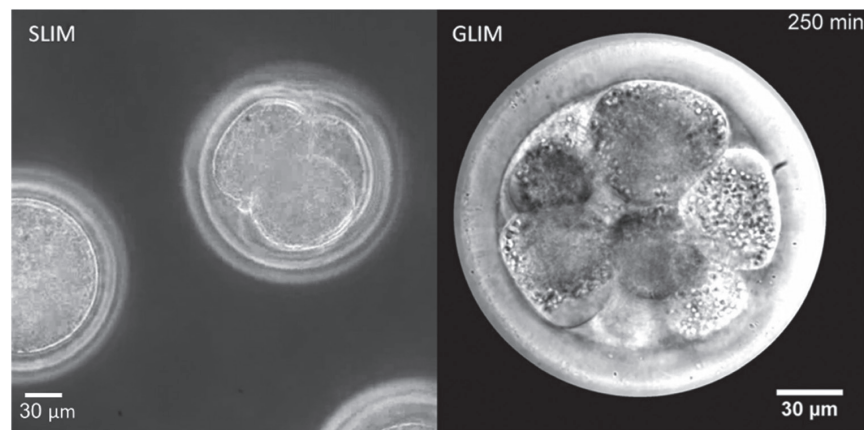
(c) Summary of ART Outcomes

Embryo Cleavage	Pearson's R	P-Value
Head / Midpiece	-0.03	>0.36
Head / Tail	-0.99	<0.01
Midpiece / Tail	-0.98	<0.01
Blastocyst Formation		
Head / Midpiece	+0.78	0.05
Head / Tail	-0.30	0.31
Midpiece / Tail	-0.49	0.22



Summary of outcomes. (a) Cleavage is strongly favored by a more massive tail, while (b) blastocyst development is favored by a heavier head. (c) Summary across the five bulls for cleavage and blastocyst rates. Reprinted with permission from Kandel *et al.*, Proc. Natl. Acad. Sci. USA **117**, 18302–18309 (2020) [214].

Figure 52



Imaging embryos with SLIM (left) versus GLIM (right). Here, bovine embryos are imaged with both techniques. While SLIM brings information at various depths into focus, GLIM is more depth selective. The middle (thickest) part of the embryo imaged using SLIM lost contrast due to multiple scattering. This is not the with the GLIM image. In summary, GLIM has better depth sectioning compared to SLIM. Reprinted by permission from Macmillan Publishers Ltd.: Nguyen *et al.*, Nat. Commun. **8**, 210 (2017) [26]. Copyright 2017.

removed using a halo removal numerical algorithm. The software developed in-house enables high-throughput acquisition, whole slide scanning, mosaic tile registration, and imaging with a color camera. WDT and WPT are two 3D tomographic methods developed with SLIM (Section 3).

Particularly because of its inherent stability, SLIM enables a large number of basic science and clinical applications (Section 4). SLIM can study cell dynamics, cell growth and proliferation, cell migration, mass transport, etc. In clinical settings, SLIM can assist with cancer studies, reproductive technology, and blood testing. Recently, the development of deep learning has brought new exciting opportunities for SLIM imaging (Section 5). AI adds computational specificity to SLIM data and allows for in-depth applications in cell biology and pathology. We anticipate that, due to these unique capabilities, SLIM will be embraced by the broader community in the years to come.

FUNDING

National Science Foundation (CBET0939511 STC, NRT-UtB 173525); National Institutes of Health (CA238191, GM129709).

DISCLOSURES

GP: Phi Optics, Inc. (F).

REFERENCES

1. C. A. Combs and H. Shroff, "Fluorescence microscopy: a concise guide to current imaging methods," *Curr. Protoc. Neurosci.* **79**, 2.1.1 (2017).
2. R. A. Hoebe, C. H. Van Oven, T. W. J. Gadella, Jr., P. B. Dhonukshe, C. J. F. Van Noorden, and E. M. M. Manders, "Controlled light-exposure microscopy reduces photobleaching and phototoxicity in fluorescence live-cell imaging," *Nat. Biotechnol.* **25**, 249–253 (2007).
3. P. P. Laissue, R. A. Alghamdi, P. Tomancak, E. G. Reynaud, and H. Shroff, "Assessing phototoxicity in live fluorescence imaging," *Nat. Methods* **14**, 657–661 (2017).
4. E. C. Jensen, "Use of fluorescent probes: their effect on cell biology and limitations," *Anatomical Rec.* **295**, 2031–2036 (2012).
5. D. W. Piston and G. J. Kremers, "Fluorescent protein FRET: the good, the bad and the ugly," *Trends Biochem. Sci.* **32**, 407–414 (2007).
6. J. C. Waters, *Accuracy and Precision in Quantitative Fluorescence Microscopy* (The Rockefeller University, 2009).
7. D. A. Zacharias, J. D. Violin, A. C. Newton, and R. Y. Tsien, "Partitioning of lipid-modified monomeric GFPs into membrane microdomains of live cells," *Science* **296**, 913–916 (2002).
8. C. Seniya, C. Towers, and D. Towers, "Improvements in low-cost label-free QPI microscope for live cell imaging," in *European Conference on Biomedical Optics* (Optical Society of America, 2017).
9. B. Joshi, I. Barman, N. C. Dingari, N. Cardenas, J. S. Soares, R. R. Dasari, and S. Mohanty, "Label-free route to rapid, nanoscale characterization of cellular structure and dynamics through opaque media," *Sci. Rep.* **3**, 2822 (2013).
10. L. Cherkezyan, I. Capoglu, H. Subramanian, J. D. Rogers, D. Damania, A. Taflove, and V. Backman, "Interferometric spectroscopy of scattered light can quantify the statistics of subdiffractional refractive-index fluctuations," *Phys. Rev. Lett.* **111**, 033903 (2013).

11. P. Girshovitz and N. T. Shaked, “Generalized cell morphological parameters based on interferometric phase microscopy and their application to cell life cycle characterization,” *Biomed. Opt. Express* **3**, 1757–1773 (2012).
12. T. A. Zangle and M. A. Teitell, “Live-cell mass profiling: an emerging approach in quantitative biophysics,” *Nat. Methods* **11**, 1221–1228 (2014).
13. P. S. Carney, B. Deutsch, A. A. Govyadinov, and R. Hillenbrand, “Phase in nanooptics,” *ACS Nano* **6**, 8–12 (2012).
14. Y. Park, C. Depeursinge, and G. Popescu, “Quantitative phase imaging in biomedicine,” *Nat. Photonics* **12**, 578–589 (2018).
15. P. Gabriel, *Quantitative Phase Imaging of Cells and Tissues* (McGraw-Hill, 2011).
16. T. Kim, R. Zhou, L. L. Goddard, and G. Popescu, “Breakthroughs in photonics 2013: quantitative phase imaging: metrology meets biology,” *IEEE Photon. J.* **6**, 0700909 (2014).
17. J. Mertz, *Introduction to Optical Microscopy*, 2nd ed. (Cambridge University, 2019).
18. F. Zernike, “Phase contrast, a new method for the microscopic observation of transparent objects,” *Physica* **9**, 686–698 (1942).
19. G. Nomarski, “Differential microinterferometer with polarized waves,” *J. Phys. Rad. (Paris)* **16**, 9S (1955).
20. M. K. Kim, “Principles and techniques of digital holographic microscopy,” *SPIE Rev.* **1**, 018005 (2010).
21. V. Tychinsky, A. V. Kretushev, I. V. Klemyashov, V. D. Zverzhkhovskiy, T. V. Vyshenskaya, and A. A. Shtil, “Quantitative phase imaging of living cells: application of the phase volume and area functions to the analysis of ‘nucleolar stress’,” *J. Biomed. Opt.* **18**, 111413 (2013).
22. P. Bon, S. Lécart, E. Fort, and S. Lévêque-Fort, “Fast label-free cytoskeletal network imaging in living mammalian cells,” *Biophys. J.* **106**, 1588–1595 (2014).
23. R. Gannavaru, B. Bhaduri, K. Tangella, and G. Popescu, “Spatiotemporal characterization of a fibrin clot using quantitative phase imaging,” *PLoS ONE* **9**, e111381 (2014).
24. Z. Li, H. Chen, H. Li, and W. R. Chen, “Optical properties of tissues quantified using morphological granulometry from phase-contrast images of thin tissue samples,” *J. Xray Sci. Technol.* **23**, 111–118 (2015).
25. A. Descloux, K. S. Größmayer, E. Bostan, T. Lukes, A. Bouwens, A. Sharipov, S. Geissbuehler, A.-L. Mahul-Mellier, H. A. Lashuel, M. Leutenegger, and T. Lasser, “Combined multi-plane phase retrieval and super-resolution optical fluctuation imaging for 4D cell microscopy,” *Nat. Photonics* **12**, 165–172 (2018).
26. T. H. Nguyen, M. E. Kandel, M. Rubessa, M. B. Wheeler, and G. Popescu, “Gradient light interference microscopy for 3D imaging of unlabeled specimens,” *Nat. Commun.* **8**, 210 (2017).
27. E. Wolf, “What kind of phases does one measure in usual interference experiments?” *Opt. Commun.* **284**, 4235–4236 (2011).
28. L. Limozin and K. Sengupta, “Quantitative reflection interference contrast microscopy (RICM) in soft matter and cell adhesion,” *ChemPhysChem* **10**, 2752–2768 (2009).
29. J.-S. Park, A. Kashkanova, J. Lühr, D. Albrecht, A. Schambony, and V. Sandoghdar, “Label-free and live cell imaging by interferometric scattering microscopy,” *Chem. Sci.* **9**, 2690–2697 (2018).

30. A. H. Kashani, C. L. Chen, J. K. Gahm, F. Zheng, G. M. Richter, P. J. Rosenfeld, Y. Shi, and R. K. Wang, "Optical coherence tomography angiography: a comprehensive review of current methods and clinical applications," *Prog. Retinal Eye Res.* **60**, 66–100 (2017).
31. W. Drexler and J. G. Fujimoto, *Optical Coherence Tomography: Technology and Applications* (Springer, 2008).
32. C. Edwards, B. Bhaduri, B. G. Griffin, L. L. Goddard, and G. Popescu, "Epi-illumination diffraction phase microscopy with white light," *Opt. Lett.* **39**, 6162–6165 (2014).
33. S. Chowdhury and J. Izatt, "Structured illumination quantitative phase microscopy for enhanced resolution amplitude and phase imaging," *Biomed. Opt. Express* **4**, 1795–1805 (2013).
34. Y. Choi, T. D. Yang, K. J. Lee, and W. Choi, "Full-field and single-shot quantitative phase microscopy using dynamic speckle illumination," *Opt. Lett.* **36**, 2465–2467 (2011).
35. B. C. Platt and R. Shack, "History and principles of Shack-Hartmann wavefront sensing," *J. Refractive Surg.* **17**, S573–S577 (2001).
36. F. Soldevila, V. Durán, P. Clemente, J. Lancis, and E. Tajahuerce, "Phase imaging by spatial wavefront sampling," *Optica* **5**, 164–174 (2018).
37. J. Li, Q. Chen, J. Zhang, Y. Zhang, L. Lu, and C. Zuo, "Efficient quantitative phase microscopy using programmable annular LED illumination," *Biomed. Opt. Express* **8**, 4687–4705 (2017).
38. M. R. Kellman, E. Bostan, N. Repina, and L. Waller, "Physics-based learned design: optimized coded-illumination for quantitative phase imaging," *IEEE Trans. Comput. Imaging* **5**, 344–353 (2019).
39. S. O. Isikman, A. Greenbaum, M. Lee, W. Bishara, O. Mudanyali, T.-W. Su, and A. Ozcan, "Modern trends in imaging VIII: lensfree computational microscopy tools for cell and tissue imaging at the point-of-care and in low-resource settings," *Anal. Cell. Pathol.* **35**, 229–247 (2012).
40. R. W. Gerchberg, "A practical algorithm for the determination of phase from image and diffraction plane pictures," *Optik* **35**, 237–246 (1972).
41. G. Zheng, R. Horstmeyer, and C. Yang, "Wide-field, high-resolution Fourier ptychographic microscopy," *Nat. Photonics* **7**, 739–745 (2013).
42. C. Zuo, J. Li, J. Sun, Y. Fan, J. Zhang, L. Lu, R. Zhang, B. Wang, L. Huang, and Q. Chen, "Transport of intensity equation: a tutorial," *Opt. Laser Eng.* **135**, 106187 (2020).
43. E. R. Oldewurtel, Y. Kitahara, and G. Özbaykal, "Bacteria control cell volume by coupling cell-surface expansion to dry-mass growth," bioRxiv: doi.org/10.1101/769786 (2019).
44. A. E. Vasdekis, H. Alanazi, A. M. Silverman, C. J. Williams, A. J. Canul, J. B. Cliff, A. C. Dohnalkova, and G. Stephanopoulos, "Eliciting the impacts of cellular noise on metabolic trade-offs by quantitative mass imaging," *Nat. Commun.* **10**, 848 (2019).
45. C. King, P. Sengupta, A. Y. Seo, and J. Lippincott-Schwartz, "ER membranes exhibit phase behavior at sites of organelle contact," *Proc. Natl. Acad. Sci. USA* **117**, 7225–7235 (2020).
46. T. Juffmann, A. de los Ríos Sommer, and S. Gigan, "Local optimization of wave-fronts for optimal sensitivity phase imaging (LowPhi)," *Opt. Commun.* **454**, 124484 (2020).
47. S. Coquoz, A. Nahas, M. Sison, A. Lopez, and T. Lasser, "High-speed phase-shifting common-path quantitative phase imaging with a piezoelectric actuator," *J. Biomed. Opt.* **21**, 126019 (2016).

48. C. Seniya, C. E. Towers, and D. P. Towers, “A flexible quantitative phase imaging microscope for label-free imaging of thick biological specimens using aperture masks,” *bioRxiv*: doi.org/10.1101/709121 (2019).
49. K. Chu, Z. J. Smith, S. Wachsmann-Hogiu, and S. Lane, “Super-resolved spatial light interference microscopy,” *J. Opt. Soc. Am. A* **29**, 344–351 (2012).
50. T. Seuthe, A. Mermillod-Blondin, M. Grehn, J. Bonse, L. Wondraczek, and M. Eberstein, “Structural relaxation phenomena in silicate glasses modified by irradiation with femtosecond laser pulses,” *Sci. Rep.* **7**, 43815 (2017).
51. H. Wu, Z. Li, H. Li, and S. Wu, “Quantitative phase imaging of breast cancer cell based on SLIM,” *J. Phys. Conf. Ser.* **679**, 012003 (2016).
52. M. Sarshar, W. T. Wong, and B. Anvari, “Label-free measurements of membrane tether thickness using optical tweezers combined with SLIM,” *Proc. SPIE* **9336**, 93361M (2015).
53. O. Izotova and V. Ryabukho, “Parameter optimization of phase microscope with the interferometer as a spatial phase modulator,” *Proc. SPIE* **9529**, 95291H (2015).
54. X. Fan, Z. Tang, J. J. Healy, K. O’Dwyer, and B. M. Hennelly, “Label-free Rheinberg staining of cells using digital holographic microscopy and spatial light interference microscopy,” *Proc. SPIE* **11186**, 111860D (2019).
55. Z. El-Schich, A. Leida Mölder, and A. G. Wingren, “Quantitative phase imaging for label-free analysis of cancer cells—focus on digital holographic microscopy,” *Appl. Sci.* **8**, 1027 (2018).
56. H. Alanazi, A. J. Canul, A. Garman, J. Quimby, and A. E. Vasdekis, “Robust microbial cell segmentation by optical-phase thresholding with minimal processing requirements,” *Cytometry Part A* **91**, 443–449 (2017).
57. P. Mohammadi, G. Beaune, B. T. Stokke, J. V. I. Timonen, and M. B. Linder, “Self-coacervation of a silk-like protein and its use as an adhesive for cellulosic materials,” *ACS Macro Lett.* **7**, 1120–1125 (2018).
58. N. R. Subedi, P. S. Jung, E. L. Bredeweg, S. Nemati, S. E. Baker, D. N. Christodoulides, and A. E. Vasdekis, “Integrative quantitative-phase and airy light-sheet imaging,” *Sci. Rep.* **10**, 20150 (2020).
59. E. E. Hoover and J. A. Squier, “Advances in multiphoton microscopy technology,” *Nat. Photonics* **7**, 93–101 (2013).
60. P. J. Campagnola and L. M. Loew, “Second-harmonic imaging microscopy for visualizing biomolecular arrays in cells, tissues and organisms,” *Nat. Biotechnol.* **21**, 1356–1360 (2003).
61. S. Witte, A. Negrean, J. C. Lodder, C. P. J. de Kock, G. T. Silva, H. D. Mansvelder, and M. L. Groota, “Label-free live brain imaging and targeted patching with third-harmonic generation microscopy,” *Proc. Natl. Acad. Sci. USA* **108**, 5970–5975 (2011).
62. C. Zhang, D. Zhang, and J. X. Cheng, “Coherent Raman scattering microscopy in biology and medicine,” *Annu. Rev. Biomed. Eng.* **17**, 415–445 (2015).
63. J.-X. Cheng and X. S. Xie, *Coherent Raman Scattering Microscopy* (CRC Press, 2016).
64. X. Wu, G. Chen, J. Lu, W. Zhu, J. Qiu, J. Chen, S. Xie, S. Zhuo, and J. Yan, “Label-free detection of breast masses using multiphoton microscopy,” *PLoS ONE* **8**, e65933 (2013).
65. R. Galli, O. Uckermann, E. F. Andresen, K. D. Geiger, E. Koch, G. Schackert, G. Steiner, and M. Kirsch, “Intrinsic indicator of photodamage during label-free multiphoton microscopy of cells and tissues,” *PLoS ONE* **9**, e110295 (2014).
66. K. P. Quinn, E. C. Leal, A. Tellechea, A. Kafanas, M. E. Auster, A. Veves, and I. Georgakoudi, “Diabetic wounds exhibit distinct microstructural and metabolic

- heterogeneity through label-free multiphoton microscopy,” *J. Invest. Dermatol.* **136**, 342–344 (2016).
67. S. Zhuo, J. Yan, G. Chen, J. Chen, Y. Liu, J. Lu, X. Zhu, X. Jiang, and S. Xie, “Label-free monitoring of colonic cancer progression using multiphoton microscopy,” *Biomed. Opt. Express* **2**, 615–619 (2011).
 68. E. B. van Munster and T. W. Gadella, “Fluorescence lifetime imaging microscopy (FLIM),” in *Microscopy Techniques* (Springer, 2005), pp. 143–175.
 69. L. L. Li, K. Li, M.-Y. Li, L. Shi, Y.-H. Liu, H. Zhang, S.-L. Pan, N. Wang, Q. Zhou, and X.-Q. Yu, “BODIPY-based two-photon fluorescent probe for real-time monitoring of lysosomal viscosity with fluorescence lifetime imaging microscopy,” *Anal. Chem.* **90**, 5873–5878 (2018).
 70. J. Jenkins, S. M. Borisov, D. B. Papkovsky, and R. I. Dmitriev, “Sulforhodamine nanothermometer for multiparametric fluorescence lifetime imaging microscopy,” *Anal. Chem.* **88**, 10566–10572 (2016).
 71. A. Margineanu, J. J. Chan, D. J. Kelly, S. C. Warren, D. Flatters, S. Kumar, M. Katan, C. W. Dunsby, and P. M. W. French, “Screening for protein-protein interactions using Förster resonance energy transfer (FRET) and fluorescence lifetime imaging microscopy (FLIM),” *Sci. Rep.* **6**, 28186 (2016).
 72. W. Zheng, Y. Wu, D. Li, and J. Y. Qu, “Autofluorescence of epithelial tissue: single-photon versus two-photon excitation,” *J. Biomed. Opt.* **13**, 054010 (2008).
 73. J. Doherty, G. Cinque, and P. Gardner, “Single-cell analysis using Fourier transform infrared microspectroscopy,” *Appl. Spectrosc. Rev.* **52**, 560–587 (2016).
 74. B. R. Shakya, P. Shrestha, H.-R. Teppo, and L. Rieppo, “The use of Fourier transform infrared (FTIR) spectroscopy in skin cancer research: a systematic review,” *Appl. Spectrosc. Rev.*, doi:10.1080/05704928.2020.1791152.
 75. M. C. Yu, P. Rich, L. Foreman, J. Smith, M.-S. Yu, A. Tanna, V. Dibbur, R. Unwin, and F. W. K. Tam, “Label free detection of sensitive mid-infrared biomarkers of glomerulonephritis in urine using Fourier transform infrared spectroscopy,” *Sci. Rep.* **7**, 4601 (2017).
 76. L. V. Wang and J. Yao, “A practical guide to photoacoustic tomography in the life sciences,” *Nat. Methods* **13**, 627–638 (2016).
 77. L. V. Wang and S. Hu, “Photoacoustic tomography: *in vivo* imaging from organelles to organs,” *Science* **335**, 1458–1462 (2012).
 78. A. Gibson and H. Dehghani, “Diffuse optical imaging,” *Philos. Trans. A.* **367**, 3055–3072 (2009).
 79. J. Sharpe, “Optical projection tomography,” *Annu. Rev. Biomed. Eng.* **6**, 209–228 (2004).
 80. V. P. Zharov and D. O. Lapotko, “Photothermal imaging of nanoparticles and cells,” *IEEE J. Sel. Top. Quantum Electron.* **11**, 733–751 (2005).
 81. F. Xia, C. Wu, D. Sinefeld, B. Li, Y. Qin, and C. Xu, “In vivo label-free confocal imaging of the deep mouse brain with long-wavelength illumination,” *Biomed. Opt. Express* **9**, 6545–6555 (2018).
 82. T. F. Wu, T. M. Yen, Y. Han, Y.-J. Chiu, E. Y.-S. Lind, and Y.-H. Lo, “A light-sheet microscope compatible with mobile devices for label-free intracellular imaging and biosensing,” *Lab Chip* **14**, 3341–3348 (2014).
 83. J. Bewersdorf, A. Egner, and S. W. Hell, “4Pi microscopy,” in *Handbook of Biological Confocal Microscopy* (Springer, 2006), pp. 561–570.
 84. M. G. Gustafsson, D. Agard, and J. Sedat, “15M: 3D widefield light microscopy with better than 100 nm axial resolution,” *J. Microsc.* **195**, 10–16 (1999).
 85. B. Hecht, B. Sick, and P. Wild, “Scanning near-field optical microscopy with aperture probes: fundamentals and applications,” *J. Chem. Phys.* **112**, 7761–7774 (2000).

86. K. Goda, K. Tsia, and B. Jalali, "Serial time-encoded amplified imaging for real-time observation of fast dynamic phenomena," *Nature* **458**, 1145–1149 (2009).
87. X. Chen and O. Korotkova, "Probability density functions of instantaneous Stokes parameters on weak scattering," *Opt. Commun.* **400**, 1–8 (2017).
88. X. Chen and O. Korotkova, "Scattering of light from hollow and semi-hollow 3D scatterers with ellipsoidal, cylindrical and Cartesian symmetries," *Computer Opt.* **40** 635–641 (2016).
89. M. Born and E. Wolf, *Principles of Optics: Electromagnetic Theory of Propagation, Interference and Diffraction of Light* (Elsevier, 2013).
90. E. Wolf, Principles and Development of Diffraction Tomography, in *Trends in Optics* (Elsevier, 1996), pp. 83–110.
91. C. Hu and G. Popescu, "Physical significance of backscattering phase measurements," *Opt. Lett.* **42**, 4643–4646 (2017).
92. P. Ledwig and F. E. Robles, "Epi-mode tomographic quantitative phase imaging in thick scattering samples," *Biomed. Opt. Express* **10**, 3605–3621 (2019).
93. A. Matlock, A. Sentenac, P. C. Chaumet, J. Yi, and L. Tian, "Inverse scattering for reflection intensity phase microscopy," *Biomed. Opt. Express* **11**, 911–926 (2020).
94. L. Mandel and E. Wolf, *Optical Coherence and Quantum Optics* (Cambridge University, 1995).
95. M. E. Kandel, C. Hu, G. N. Kouzehgarani, E. Min, K. M. Sullivan, H. Kong, J. M. Li, D. N. Robson, M. U. Gillette, C. Best-Popescu, and G. Popescu, "Epi-illumination gradient light interference microscopy for imaging opaque structures," *Nat. Commun.* **10**, 4691 (2019).
96. X. Chen and O. Korotkova, "Phase structuring of 2D complex coherence states," *Opt. Lett.* **44**, 2470–2473 (2019).
97. X. Chen and O. Korotkova, "Complex degree of coherence modeling with famous planar curves," *Opt. Lett.* **43**, 6049–6052 (2018).
98. O. Korotkova and X. Chen, "Phase structuring of the complex degree of coherence," *Opt. Lett.* **43**, 4727–4730 (2018).
99. J. W. Goodman, *Statistical Optics* (Wiley, 2015).
100. J. Li, X. Chen, S. McDuffie, M. A. M. Najjar, S. M. H. Rafsanjani, and O. Korotkova, "Mitigation of atmospheric turbulence with random light carrying OAM," *Opt. Commun.* **446**, 178–185 (2019).
101. X. Chen, J. Li, S. M. H. Rafsanjani, and O. Korotkova, "Synthesis of Im-Bessel correlated beams via coherent modes," *Opt. Lett.* **43**, 3590–3593 (2018).
102. O. Korotkova, X. Chen, and T. Setälä, "Electromagnetic Schell-model beams with arbitrary complex correlation states," *Opt. Lett.* **44**, 4945–4948 (2019).
103. X. Chen, M. E. Kandel, C. Hu, Y. J. Lee, and G. Popescu, "Wolf phase tomography (WPT) of transparent structures using partially coherent illumination," *Light Sci. Appl.* **9**, 142 (2020).
104. X. Chen and O. Korotkova, "Optical beam propagation in soft anisotropic biological tissues," *OSA Continuum* **1**, 1055–1067 (2018).
105. X. Chen, J. Li, and O. Korotkova, "Light scintillation in soft biological tissues," *Waves Random Complex Media* **30**, 481–489 (2020).
106. J. Han, P. Gao, B. Yao, Y. Gu, and M. Huang, "Slightly off-axis interferometry for microscopy with second wavelength assistance," *Appl. Opt.* **50**, 2793–2798 (2011).
107. A. Hussain, J. L. Martínez, A. Lizana, and J. Campos, "Super resolution imaging achieved by using on-axis interferometry based on a spatial light modulator," *Opt. Express* **21**, 9615–9623 (2013).

108. D. S. Mehta and V. Srivastava, “Quantitative phase imaging of human red blood cells using phase-shifting white light interference microscopy with colour fringe analysis,” *Appl. Phys. Lett.* **101**, 203701 (2012).
109. Q. Zhang, L. Zhong, P. Tang, Y. Yuan, S. Liu, J. Tian, and X. Lu, “Quantitative refractive index distribution of single cell by combining phase-shifting interferometry and AFM imaging,” *Sci. Rep.* **7**, 2532 (2017).
110. B. Bhaduri, K. Tangella, and G. Popescu, “Fourier phase microscopy with white light,” *Biomed. Opt. Express* **4**, 1434–1441 (2013).
111. Z. Wang, L. Millet, M. Mir, H. Ding, S. Unarunotai, J. Rogers, M. U. Gillette, and G. Popescu, “Spatial light interference microscopy (SLIM),” *Opt. Express* **19**, 1016–1026 (2011).
112. W. S. Rockward, A. L. Thomas, B. Zhao, and C. A. DiMarzio, “Quantitative phase measurements using optical quadrature microscopy,” *Appl. Opt.* **47**, 1684–1696 (2008).
113. H. Majeed, L. Ma, Y. J. Lee, M. Kandel, E. Min, W. Jung, C. Best-Popescu, and G. Popescu, “Magnified image spatial spectrum (MISS) microscopy for nanometer and millisecond scale label-free imaging,” *Opt. Express* **26**, 5423–5440 (2018).
114. P. R. Pfau, M. V. Sivak, Jr., A. Chak, M. Kinnard, R. C. K. Wong, G. A. Isenberg, J. A. Izatt, A. Rollins, and V. Westphal, “Criteria for the diagnosis of dysplasia by endoscopic optical coherence tomography,” *Gastrointest. Endosc.* **58**, 196–202 (2003).
115. C. Remmersmann, S. Stürwald, B. Kemper, P. Langehanenberg, and G. von Bally, “Phase noise optimization in temporal phase-shifting digital holography with partial coherence light sources and its application in quantitative cell imaging,” *Appl. Opt.* **48**, 1463–1472 (2009).
116. Z. F. Phillips, M. Chen, and L. Waller, “Single-shot quantitative phase microscopy with color-multiplexed differential phase contrast (cDPC),” *PLoS ONE* **12**, e0171228 (2017).
117. M. Shan, M. E. Kandel, H. Majeed, V. Nastasa, and G. Popescu, “White-light diffraction phase microscopy at doubled space-bandwidth product,” *Opt. Express* **24**, 29033–29040 (2016).
118. W. Choi, C. Fang-Yen, K. Badizadegan, S. Oh, N. Lue, R. R. Dasari, and M. S. Feld, “Tomographic phase microscopy,” *Nat. Methods* **4**, 717–719 (2007).
119. Y. Cotte, F. Toy, P. Jourdain, N. Pavillon, D. Boss, P. Magistretti, P. Marquet, and C. Depeursinge, “Marker-free phase nanoscopy,” *Nat. Photonics* **7**, 113–117 (2013).
120. T. Kim, R. Zhou, L. L. Goddard, and G. Popescu, “Solving inverse scattering problems in biological samples by quantitative phase imaging,” *Laser Photon. Rev.* **10**, 13–39 (2016).
121. F. E. Robles, C. Wilson, G. Grant, and A. Wax, “Molecular imaging true-colour spectroscopic optical coherence tomography,” *Nat. Photonics* **5**, 744–747 (2011).
122. F. Charriere, A. Marian, F. Montfort, J. Kuehn, T. Colomb, E. Cuhe, P. Marquet, and C. Depeursinge, “Cell refractive index tomography by digital holographic microscopy,” *Opt. Lett.* **31**, 178–180 (2006).
123. X. Wang, B. W. Pogue, S. Jiang, H. Dehghani, X. Song, S. Srinivasan, B. A. Brooksby, K. D. Paulsen, C. Kogel, S. P. Poplack, and W. A. Wells, “Image reconstruction of effective Mie scattering parameters of breast tissue in vivo with near-infrared tomography,” *J. Biomed. Opt.* **11**, 041106 (2006).
124. M. Dierolf, A. Menzel, P. Thibault, P. Schneider, C. M. Kewish, R. Wepf, O. Bunk, and F. Pfeiffer, “Ptychographic x-ray computed tomography at the nanoscale,” *Nature* **467**, 436–439 (2010).

125. E. Wolf, "Three-dimensional structure determination of semi-transparent objects from holographic data," *Opt. Commun.* **1**, 153–156 (1969).
126. K. Lee, S. Shin, Z. Yaqoob, P. T. C. So, and Y. K. Park, "Low-coherent optical diffraction tomography by angle-scanning illumination," *J. Biophoton.* **12**, e201800289 (2019).
127. M. Habaza, B. Gilboa, Y. Roichman, and N. T. Shaked, "Tomographic phase microscopy with 180 degrees rotation of live cells in suspension by holographic optical tweezers," *Opt. Lett.* **40**, 1881–1884 (2015).
128. J. Jung, S.-J. Hong, H.-B. Kim, G. Kim, M. Lee, S. Shin, S. Lee, D.-J. Kim, C.-G. Lee, and Y. K. Park, "Label-free non-invasive quantitative measurement of lipid contents in individual microalgal cells using refractive index tomography," *Sci. Rep.* **8**, 6524 (2018).
129. M. Habaza, M. Kirschbaum, C. Guernth-Marschner, G. Dardikman, I. Barnea, R. Korenstein, C. Duschl, and N. T. Shaked, "Rapid 3D refractive-index imaging of live cells in suspension without labeling using dielectrophoretic cell rotation," *Adv. Sci.* **4**, 1600205 (2017).
130. B. Simon, M. Debailleul, M. Houkal, C. Ecoffet, J. Bailleul, J. Lambert, A. Spangenberg, H. Liu, O. Soppera, and O. Haeberlé, "Tomographic diffractive microscopy with isotropic resolution," *Optica* **4**, 460–463 (2017).
131. F. Macias-Garza, K. Diller, and A. Bovik, "Missing cone of frequencies and low-pass distortion in three-dimensional microscopic images," *Opt. Eng.* **27**, 276461 (1988).
132. J. Lim, K. Lee, K. H. Jin, S. Shin, S. Lee, Y. Park, and J. C. Ye, "Comparative study of iterative reconstruction algorithms for missing cone problems in optical diffraction tomography," *Opt. Express* **23**, 16933–16948 (2015).
133. M. H. Jenkins and T. K. Gaylord, "Three-dimensional quantitative phase imaging via tomographic deconvolution phase microscopy," *Appl. Opt.* **54**, 9213–9227 (2015).
134. D. Maschek, B. Goodell, J. Jellison, M. Lessard, and H. Miltz, "A new approach for the study of the chemical composition of bordered pit membranes: 4Pi and confocal laser scanning microscopy," *Am. J. Bot.* **100**, 1751–1756 (2013).
135. A. Bassi, B. Schmid, and J. Huisken, "Optical tomography complements light sheet microscopy for in toto imaging of zebrafish development," *Development* **142**, 1016–1020 (2015).
136. M. Araya-Polo, J. Jennings, A. Adler, and T. Dahlke, "Deep-learning tomography," *Leading Edge* **37**, 58–66 (2018).
137. J. Yoon, Y. J. Jo, M.-H. Kim, K. Kim, S. Lee, S.-J. Kang, and Y. K. Park, "Identification of non-activated lymphocytes using three-dimensional refractive index tomography and machine learning," *Sci. Rep.* **7**, 6654 (2017).
138. J. Li, Q. Chen, J. Sun, J. Zhang, J. Ding, and C. Zuo, "Three-dimensional tomographic microscopy technique with multi-frequency combination with partially coherent illuminations," *Biomed. Opt. Express* **9**, 2526–2542 (2018).
139. T. H. Nguyen, C. Edwards, L. L. Goddard, and G. Popescu, "Quantitative phase imaging with partially coherent illumination," *Opt. Lett.* **39**, 5511–5514 (2014).
140. J. M. Soto, J. A. Rodrigo, and T. Alieva, "Label-free quantitative 3D tomographic imaging for partially coherent light microscopy," *Opt. Express* **25**, 15699–15712 (2017).
141. T. Kim, R. Zhou, M. Mir, S. D. Babacan, P. S. Carney, L. L. Goddard, and G. Popescu, "White-light diffraction tomography of unlabelled live cells," *Nat. Photonics* **8**, 256–263 (2014).
142. N. M. Israelsen, C. R. Petersen, A. Barh, D. Jain, M. Jensen, G. Hanneschläger, P. Tidemand-Lichtenberg, C. Pedersen, A. Podoleanu, and O. Bang, "Real-time high-resolution mid-infrared optical coherence tomography," *Light Sci. Appl.* **8**, 11 (2019).

143. Z. Chen, R. M. Werkmeister, C. Blatter, and L. Schmetterer, "Optical Doppler tomography," *IEEE J. Sel. Top. Quantum Electron.* **5**, 1134–1142 (1999).
144. J. Li, Q. Chen, Z. Jialin, Z. Zhang, Y. Zhang, and C. Zuo, "Optical diffraction tomography microscopy with transport of intensity equation using a light-emitting diode array," *Opt. Laser Eng.* **95**, 26–34 (2017).
145. T. Nguyen and G. Nehmetallah, "Non-interferometric tomography of phase objects using spatial light modulators," *J. Imaging* **2**, 30 (2016).
146. C. Zuo, J. Sun, J. Zhang, Y. Hu, and Q. Chen, "Lensless phase microscopy and diffraction tomography with multi-angle and multi-wavelength illuminations using a LED matrix," *Opt. Express* **23**, 14314–14328 (2015).
147. R. Horstmeyer, J. Chung, X. Ou, G. Zheng, and C. Yang, "Diffraction tomography with Fourier ptychography," *Optica* **3**, 827–835 (2016).
148. T. R. Hillman, T. Gutzler, S. A. Alexandrov, and D. D. Sampson, "High-resolution, wide-field object reconstruction with synthetic aperture Fourier holographic optical microscopy," *Opt. Express* **17**, 7873–7892 (2009).
149. S. Chowdhury, W. J. Eldridge, A. Wax, and J. A. Izatt, "Structured illumination microscopy for dual-modality 3D sub-diffraction resolution fluorescence and refractive-index reconstruction," *Biomed. Opt. Express* **8**, 5776–5793 (2017).
150. A. M. Kingston, D. Pelliccia, A. Rack, M. P. Olbinado, Y. Cheng, G. R. Myers, and D. M. Paganin, "Ghost tomography," *Optica* **5**, 1516–1520 (2018).
151. C. G. Amiot, P. Ryczkowski, A. T. Friberg, J. M. Dudley, and G. Genty, "Ghost optical coherence tomography," *Opt. Express* **27**, 24114–24122 (2019).
152. L. V. Wang, "Multiscale photoacoustic microscopy and computed tomography," *Nat. Photonics* **3**, 503–509 (2009).
153. Y. Hoshi and Y. Yamada, "Overview of diffuse optical tomography and its clinical applications," *J. Biomed. Opt.* **21**, 091312 (2016).
154. S. Bélanger, M. Abran, X. Intes, C. Casanova, and F. Lesage, "Real-time diffuse optical tomography based on structured illumination," *J. Biomed. Opt.* **15**, 016006 (2010).
155. Z. Wang, I. S. Chun, X. Li, Z.-Y. Ong, E. Pop, L. Millet, M. Gillette, and G. Popescu, "Topography and refractometry of nanostructures using spatial light interference microscopy," *Opt. Lett.* **35**, 208–210 (2010).
156. C. Edwards, B. Bhaduri, T. Nguyen, B. G. Griffin, H. Pham, T. Kim, G. Popescu, and L. L. Goddard, "Effects of spatial coherence in diffraction phase microscopy," *Opt. Express* **22**, 5133–5146 (2014).
157. T. Kim, R. Zhu, T. H. Nguyen, R. Zhou, C. Edwards, L. L. Goddard, and G. Popescu, "Deterministic signal associated with a random field," *Opt. Express* **21**, 20806–20820 (2013).
158. T. H. Nguyen, M. Kandel, H. M. Shakir, C. Best-Popescu, J. Arikath, M. N. Do, and G. Popescu, "Halo-free phase contrast microscopy," *Sci. Rep.* **7**, 44034 (2017).
159. S. B. Mehta and C. J. Sheppard, "Using the phase-space imager to analyze partially coherent imaging systems: bright-field, phase contrast, differential interference contrast, differential phase contrast, and spiral phase contrast," *J. Mod. Opt.* **57**, 718–739 (2010).
160. H. H. Hopkins, "On the diffraction theory of optical images," *Proc. R. Soc. London Ser. A* **217**, 408–432 (1953).
161. M. E. Kandel, M. Fanous, C. Best-Popescu, and G. Popescu, "Real-time halo correction in phase contrast imaging," *Biomed. Opt. Express* **9**, 623–635 (2018).
162. T. H. Nguyen, C. Edwards, L. L. Goddard, and G. Popescu, "Quantitative phase imaging of weakly scattering objects using partially coherent illumination," *Opt. Express* **24**, 11683–11693 (2016).

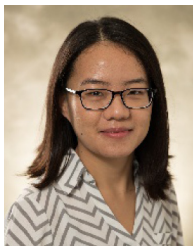
163. B. Bhaduri, C. Edwards, H. Pham, R. Zhou, T. H. Nguyen, L. L. Goddard, and G. Popescu, "Diffraction phase microscopy: principles and applications in materials and life sciences," *Adv. Opt. Photon.* **6**, 57–119 (2014).
164. N. Savage, "Digital spatial light modulators," *Nat. Photonics* **3**, 170–172 (2009).
165. T. H. Nguyen and G. Popescu, "Spatial light interference microscopy (SLIM) using twisted-nematic liquid-crystal modulation," *Biomed. Opt. Express* **4**, 1571–1583 (2013).
166. M. Sarshar, T. Lu, and B. Anvari, "Combined optical micromanipulation and interferometric topography (COMMIT)," *Biomed. Opt. Express* **7**, 1365–1374 (2016).
167. N. Geerts, *The Hilbert Transform in Complex Envelope Displacement Analysis (CEDA)* (DCT Rapporten, 1996).
168. G. Thalhammer, R. W. Bowman, G. D. Love, M. J. Padgett, and M. Ritsch-Marte, "Speeding up liquid crystal SLMs using overdrive with phase change reduction," *Opt. Express* **21**, 1779–1797 (2013).
169. M. E. Kandel, S. Sridharan, J. Liang, Z. Luo, K. Han, V. Macias, A. Shah, R. Patel, K. Tangella, A. Kajdacsy-Balla, G. Guzman, and G. Popescu, "Label-free tissue scanner for colorectal cancer screening," *J. Biomed. Opt.* **22**, 66016 (2017).
170. B. Bhaduri, D. Wickland, R. Wang, V. Chan, R. Bashir, and G. Popescu, "Cardiomyocyte imaging using real-time spatial light interference microscopy (SLIM)," *PLoS ONE* **8**, e56930 (2013).
171. M. Fanous, M. P. Caputo, Y. J. Lee, L. A. Rund, C. Best-Popescu, M. E. Kandel, R. W. Johnson, T. Das, M. J. Kuchan, and G. Popescu, "Quantifying Myelin in brain tissue using color spatial light interference microscopy (cSLIM)," arXiv:2003.01053 (2020).
172. Z. Yan, M. Han, Y. Shi, A. Badea, Y. Yang, A. Kulkarni, E. Hanson, M. E. Kandel, X. Wen, F. Zhang, Y. Luo, Q. Lin, H. Zhang, X. Guo, Y. Huang, K. Nan, S. Jia, A. W. Oraham, M. B. Mevis, J. Lim, X. Guo, M. Gao, W. Ryu, K. J. Yu, B. G. Nicolau, A. Petronico, S. S. Rubakhin, J. Lou, P. M. Ajayan, K. Thornton, G. Popescu, D. Fang, J. V. Sweedler, P. V. Braun, H. Zhang, R. G. Nuzzo, Y. Huang, Y. Zhang, and J. A. Rogers, "Three-dimensional mesostructures as high-temperature growth templates, electronic cellular scaffolds, and self-propelled microrobots," *Proc. Natl. Acad. Sci. USA* **114**, E9455–E9464 (2017).
173. E. G. Reynaud, J. Peychl, J. Huisken, and P. Tomancak, "Guide to light-sheet microscopy for adventurous biologists," *Nat. Methods* **12**, 30–34 (2015).
174. N. Stuurman and R. D. Vale, "Impact of new camera technologies on discoveries in cell biology," *Biol. Bull.* **231**, 5–13 (2016).
175. M. E. Kandel, *High Throughput Platform for Multiscale Quantitative Phase Imaging* (2016).
176. Fujitsu, "Fujitsu server PRIMERGY Windows Server 2012 R2 storage spaces performance," 2014, <https://sp.ts.fujitsu.com/dmsp/Publications/public/wp-windows-storage-spaces-r2-performance-ww-en.pdf>.
177. M. E. Kandel, D. Fernandes, A. M. Taylor, H. Shakir, C. Best-Popescu, and G. Popescu, "Three-dimensional intracellular transport in neuron bodies and neurites investigated by label-free dispersion-relation phase spectroscopy," *Cytometry Part A* **91**, 519–526 (2017).
178. D. M. M. Sinclair, Measuring Solid-State Drive Behavior, https://pages.cs.wisc.edu/~sinclair/cs736/cs736_finalReport_myers_sinclair.pdf.
179. D. Shearer, *Samba Architecture: Part II. Samba Basics*, in *SAMBA Developers Guide*, J. R. T. S. T. Vernooij, ed. (1997).
180. X. Ou, R. Horstmeyer, C. Yang, and G. Zheng, "Quantitative phase imaging via Fourier ptychographic microscopy," *Opt. Lett.* **38**, 4845–4848 (2013).

181. E. De Castro and C. Morandi, "Registration of translated and rotated images using finite Fourier transforms," *IEEE Trans. Pattern Anal. Mach. Intell.* **9**, 700–703 (1987).
182. S. Preibisch, S. Saalfeld, and P. Tomancak, "Globally optimal stitching of tiled 3D microscopic image acquisitions," *Bioinformatics* **25**, 1463–1465 (2009).
183. H. Majeed, A. Keikhosravi, M. E. Kandel, T. H. Nguyen, Y. Liu, A. Kajdacsy-Balla, K. Tangella, K. W. Eliceiri, and G. Popescu, "Quantitative histopathology of stained tissues using color spatial light interference microscopy (cSLIM)," *Sci. Rep.* **9**, 14679 (2019).
184. X. Li, B. Gunturk, and L. Zhang, "Image demosaicing: a systematic survey," *Proc. SPIE* **6822**, 68221J (2008).
185. H. S. Malvar, L.-W. He, and R. Cutler, "High-quality linear interpolation for demosaicing of Bayer-patterned color images," in *IEEE International Conference on Acoustics, Speech, and Signal Processing* (IEEE, 2004).
186. L. Ma, M. E. Kandel, H. Majeed, V. Nastasa, and G. Popescu, "White light diffraction phase microscopy with slightly off-axis blind two-step phase-shifting," *Opt. Commun.* **455**, 124563 (2020).
187. S. K. Debnath and Y. Park, "Real-time quantitative phase imaging with a spatial phase-shifting algorithm," *Opt. Lett.* **36**, 4677–4679 (2011).
188. V. Singh, R. Joshi, S. Tayal, and D. S. Mehta, "Speckle-free common-path quantitative phase imaging with high temporal phase stability using a partially spatially coherent multi-spectral light source," *Laser Phys. Lett.* **16**, 025601 (2019).
189. Y. Baek, K. Lee, J. Yoon, K. Kim, and Y. Park, "White-light quantitative phase imaging unit," *Opt. Express* **24**, 9308–9315 (2016).
190. A. Fan, A. Tofangchi, M. Kandel, G. Popescu, and T. Saif, "Coupled circumferential and axial tension driven by actin and myosin influences *in vivo* axon diameter," *Sci. Rep.* **7**, 14188 (2017).
191. A. Tzur, R. Kafri, V. S. LeBleu, G. Lahav, and M. W. Kirschner, "Cell growth and size homeostasis in proliferating animal cells," *Science* **325**, 167–171 (2009).
192. M. Mir, Z. Wang, Z. Shen, M. Bednarz, R. Bashir, I. Golding, S. G. Prasanth, and G. Popescu, "Optical measurement of cycle-dependent cell growth," *Proc. Natl. Acad. Sci. USA* **108**, 13124–13129 (2011).
193. R. Barer, "Interference microscopy and mass determination," *Nature* **169**, 366–367 (1952).
194. R. Barer, "Determination of dry mass, thickness, solid and water concentration in living cells," *Nature* **172**, 1097–1098 (1953).
195. G. Popescu, Y. Park, N. Lue, C. Best-Popescu, L. Deflores, R. R. Dasari, M. S. Feld, and K. Badizadegan, "Optical imaging of cell mass and growth dynamics," *Am. J. Physiol.* **295**, C538–C544 (2008).
196. M. L. Steinhauser, "Multi-isotope imaging mass spectrometry quantifies stem cell division and metabolism," *Nature* **481**, 516–519 (2012).
197. M. E. Kandel, W. Lu, J. Liang, O. Aydin, T. A. Saif, and G. Popescu, "Cell-to-cell influence on growth in large populations," *Biomed. Opt. Express* **10**, 4664–4675 (2019).
198. S. Sridharan, M. Mir, and G. Popescu, "Simultaneous optical measurements of cell motility and growth," *Biomed. Opt. Express* **2**, 2815–2820 (2011).
199. R. Wang, W. Zhuo, M. Larry, M. U. Gillette, A. J. Levine, and G. Popescu, "Dispersion-relation phase spectroscopy of intracellular transport," *Opt. Express* **19**, 20571–20579 (2011).
200. M. E. Kandel, K. W. Teng, P. R. Selvin, and G. Popescu, "Label-free imaging of single microtubule dynamics using spatial light interference microscopy," *ACS Nano* **11**, 647–655 (2017).

201. M. Mir, T. Kim, A. Majumder, M. Xiang, R. Wang, S. C. Liu, M. U. Gillette, S. Stice, and G. Popescu, "Label-free characterization of emerging human neuronal networks," *Sci. Rep.* **4**, 4434 (2014).
202. Y. J. Lee, P. Cintora, J. Arikath, O. Akinsola, M. Kandel, G. Popescu, and C. Best-Popescu, "Quantitative assessment of neural outgrowth using spatial light interference microscopy," *J. Biomed. Opt.* **22**, 66015 (2017).
203. P. Cintora, J. Arikath, M. Kandel, G. Popescu, and C. Best-Popescu, "Cell density modulates intracellular mass transport in neural networks," *Cytometry Part A* **91**, 503–509 (2017).
204. C. Yin, X. Xiao, V. Balaban, M. E. Kandel, Y. J. Lee, G. Popescu, and P. Bogdan, "Network science characteristics of brain-derived neuronal cultures deciphered from quantitative phase imaging data," *Sci. Rep.* **10**, 15078 (2020).
205. S. Robbin, *Pathological Basis of Disease* (Saunders, 1999).
206. Z. Wang, K. Tangella, A. Balla, and G. Popescu, "Tissue refractive index as marker of disease," *J. Biomed. Opt.* **16**, 116017 (2011).
207. H. Ding, Z. Wang, X. Liang, S. A. Boppart, K. Tangella, and G. Popescu, "Measuring the scattering parameters of tissues from quantitative phase imaging of thin slices," *Opt. Lett.* **36**, 2281–2283 (2011).
208. H. Ding, F. Nguyen, S. A. Boppart, and G. Popescu, "Optical properties of tissues quantified by Fourier-transform light scattering," *Opt. Lett.* **34**, 1372–1374 (2009).
209. M. Takabayashi, H. Majeed, A. Kajdacsy-Balla, and G. Popescu, "Tissue spatial correlation as cancer marker," *J. Biomed. Opt.* **24**, 016502 (2019).
210. H. Majeed, M. E. Kandel, K. Han, Z. Luo, V. Macias, K. Tangella, A. Balla, and G. Popescu, "Breast cancer diagnosis using spatial light interference microscopy," *J. Biomed. Opt.* **20**, 111210 (2015).
211. S. Sridharan, V. Macias, K. Tangella, J. Melamed, E. Dube, M. X. Kong, A. Kajdacsy-Balla, and G. Popescu, "Prediction of prostate cancer recurrence using quantitative phase imaging: validation on a general population," *Sci. Rep.* **6**, 33818 (2016).
212. S. Sridharan, V. Macias, K. Tangella, J. Melamed, E. Dube, M. X. Kong, A. Kajdacsy-Balla, and G. Popescu, "Prediction of prostate cancer recurrence using quantitative phase imaging," *Sci. Rep.* **5**, 9976 (2015).
213. M. Fanous, A. Keikhosravi, A. Kajdacsy-Balla, K. W. Eliceiri, and G. Popescu, "Quantitative phase imaging of stromal prognostic markers in pancreatic ductal adenocarcinoma," *Biomed. Opt. Express* **11**, 1354–1364 (2020).
214. M. E. Kandel, M. Rubessa, Y. R. He, S. Schreiber, S. Meyers, L. M. Naves, M. K. Sermersheim, G. S. Sell, M. J. Szewczyk, N. Sobh, M. B. Wheeler, and G. Popescu, "Reproductive outcomes predicted by phase imaging with computational specificity of spermatozoon ultrastructure," *Proc. Natl. Acad. Sci. USA* **117**, 18302–18309 (2020).
215. A. A. Evans, C. A. Best, K. Badizadegan, R. R. Dasari, M. S. Feld, T. Kuriabova, M. L. Henle, A. J. Levine, and G. Popescu, "Geometric localization of thermal fluctuations in red blood cells," *Proc. Natl. Acad. Sci. USA* **114**, 2865–2870 (2017).
216. Y. Park, C. A. Best, K. Badizadegan, R. R. Dasari, M. S. Feld, T. Kuriabova, M. L. Henle, A. J. Levine, and G. Popescu, "Measurement of red blood cell mechanics during morphological changes," *Proc. Natl. Acad. Sci. USA* **107**, 6731–6736 (2010).
217. Y. Park, M. Diez-Silva, G. Popescu, G. Lykotrafitis, W. Choi, M. S. Feld, and S. Suresh, "Refractive index maps and membrane dynamics of human red blood cells parasitized by *Plasmodium falciparum*," *Proc. Natl. Acad. Sci. USA* **105**, 13730–13735 (2008).

218. B. Bhaduri, M. Kandel, C. Brugnara, K. Tangella, and G. Popescu, "Optical assay of erythrocyte function in banked blood," *Sci. Rep.* **4**, 6211 (2014).
219. M. E. Kandel, Y. R. He, Y. J. Lee, T. H.-Y. Chen, K. M. Sullivan, O. Aydin, M. T. A. Saif, H. Kong, N. Sobh, and G. Popescu, "Phase imaging with computational specificity (PICS) for measuring dry mass changes in sub-cellular compartments," *Nat. Commun.* **11**, 6256 (2020).
220. O. Ronneberger, P. Fischer, and T. Brox, "U-net: convolutional networks for biomedical image segmentation," in *International Conference on Medical Image Computing and Computer-Assisted Intervention* (Springer, 2015).
221. A. Krizhevsky, I. Sutskever, and G. E. Hinton, "Imagenet classification with deep convolutional neural networks," in *Advances in Neural Information Processing Systems* (MIT Press, 2012).
222. P. Isola, J.-Y. Zhu, T. Zhou, and A. A. Efros, "Image-to-image translation with conditional adversarial networks," in *Proceedings of the IEEE Conference on Computer Vision and Pattern Recognition* (IEEE, 2017).
223. S. K. Kumar, "On weight initialization in deep neural networks," arXiv:1704.08863 (2017).
224. V. Nair and G. E. Hinton, "Rectified linear units improve restricted Boltzmann machines," in *Proceedings of the 27th International Conference on Machine Learning (ICML)* (Omnipress, 2010).
225. P. Ramachandran, B. Zoph, and Q. V. Le, "Swish: a self-gated activation function," arXiv:1710.05941 (2017).
226. J. W. Lichtman and J. A. Conchello, "Fluorescence microscopy," *Nat. Methods* **2**, 910–919 (2005).
227. J. G. Moffat, J. Rudolph, and D. Bailey, "Phenotypic screening in cancer drug discovery—past, present and future," *Nat. Rev. Drug Discovery* **13**, 588–602 (2014).
228. W. Rawat and Z. Wang, "Deep convolutional neural networks for image classification: a comprehensive review," *Neural Comput.* **29**, 2352–2449 (2017).
229. E. M. Christiansen, S. Yang, M. Ando, and A. Javaherian, "In silico labeling: predicting fluorescent labels in unlabeled images," *Cell* **173**, 792–803 (2018).
230. Y. Rivenson, H. Wang, Z. Wei, K. de Haan, Y. Zhang, Y. Wu, H. Günaydın, J. E. Zuckerman, T. Chong, A. E. Sisk, L. M. Westbrook, W. D. Wallace, and A. Ozcan, "Virtual histological staining of unlabelled tissue-autofluorescence images via deep learning," *Nat. Biomed. Eng.* **3**, 466–477 (2019).
231. W. W. Sung, Y.-M. Lin, P.-R. Wu, H.-H. Yen, H.-W. Lai, T.-C. Su, R.-H. Huang, C.-K. Wen, C.-Y. Chen, C.-J. Chen, and K.-T. Yeh, "High nuclear/cytoplasmic ratio of Cdk1 expression predicts poor prognosis in colorectal cancer patients," *BMC Cancer* **14**, 951 (2014).
232. S. M. Guo, L.-H. Yeh, J. Folkesson, I. E. Ivanov, A. P. Krishnan, M. G. Keefe, E. Hashemi, D. Shin, B. B. Chhun, N. H. Cho, M. D. Leonetti, M. H. Han, T. J. Nowakowski, and S. B. Mehta, "Revealing architectural order with quantitative label-free imaging and deep learning," *elife* **9**, e55502 (2020).
233. M. Rubessa, M. E. Kandel, S. Schreiber, S. Meyers, D. H. Beck, G. Popescu, and M. B. Wheeler, "Morphometric analysis of sperm used for IVP by three different separation methods with spatial light interference microscopy," *Syst. Biol. Reprod. Med.* **66**, 26–36 (2020).
234. L. Dehmelt and S. Halpain, "The MAP2/Tau family of microtubule-associated proteins," *Genome Biol.* **6**, 204 (2005).
235. C. Hu, S. He, Y. J. Lee, Y. He, E. M. Kong, H. Li, M. A. Anastasio, and G. Popescu, "Label-free cell viability assay using phase imaging with computational specificity," *Nature Commun.*, submitted for publication.
236. M. Tan and Q. V. Le, "Efficientnet: rethinking model scaling for convolutional neural networks," arXiv:1905.11946 (2019).

237. S. Paxton, M. Peckham, and A. Knibbs, *The Leeds Histology Guide* (2003).
238. R. Berwick, “An Idiot’s Guide to Support Vector Machines,” in *Vision* (University of Central Florida, 2003).
239. K. Simonyan and A. Zisserman, “Very deep convolutional networks for large-scale image recognition,” arXiv:1409.1556 (2014).
240. J. K. Zhang, Y. R. He, N. Sobh, and G. Popescu, “Label-free colorectal cancer screening using deep learning and spatial light interference microscopy (SLIM),” *APL Photon.* **5**, 040805 (2020).
241. T. H. Nguyen, S. Sridharan, V. MacIas, A. Kajdacsy-Balla, J. Melamed, M. N. Do, and G. Popescua, “Automatic Gleason grading of prostate cancer using quantitative phase imaging and machine learning,” *J. Biomed. Opt.* **22**, 36015 (2017).
242. A. C. Van Steirteghem, Z. Nagy, H. Joris, J. Liu, C. Staessen, J. Smits, A. Wisanto, and P. Devroey, “High fertilization and implantation rates after intracytoplasmic sperm injection,” *Hum. Reprod.* **8**, 1061–1066 (1993).
243. J. R. Kovac and L. I. Lipshultz, “Sperm morphology and reproductive success,” *Asian J. Androl.* **18**, 402 (2016).
244. X. Yi, E. Walia, and P. Babyn, “Generative adversarial network in medical imaging: a review,” *Med. Image Anal.* **58**, 101552 (2019).



Dr. Xi Chen is a postdoctoral research associate at the Beckman Institute, University of Illinois at Urbana-Champaign (UIUC). She obtained her Ph.D. in Physics from the University of Miami in 2019 and her B.S. in Applied Physics from Chongqing University in China in 2014. Her Ph.D. focused on studying phase modulation of stationary light fields with applications in biophotonics. Her postdoctoral research lies in confocal quantitative phase imaging, inverse problem algorithms, and statistical and coherence theory. Her research goal is to develop imaging modalities for turbid samples to study personalized medicine and treatment.



Dr. Mikhail E. Kandel works on medical image analysis, high-throughput instrumentation, and artificial intelligence for microscopy. He received his Ph.D. in Electrical and Computer Engineering from UIUC in 2020. He believes that AI is revolutionizing optical imaging by adding computational specificity to label-free imaging. Now he is at Groq Inc., contributing to the future of computing with stream processors.



Dr. Gabriel Popescu is the William L. Everitt Distinguished Professor of Electrical and Computer Engineering at the University of Illinois at Urbana-Champaign. He directs the Quantitative Light Imaging Laboratory at the Beckman Institute for Advanced Science and Technology. He received B.S. and M.S. degrees in Physics from University of Bucharest, in 1995 and 1996, respectively. He obtained his M.S. in Optics in 1999 and a Ph.D. in Optics in 2002 from the School of Optics/CREOL (now the College of Optics and Photonics), followed by postdoctoral work at MIT, under the late Michael Feld. He is an OSA, SPIE, and AIMBE Fellow, and IEEE Senior Member.